# STUDYING MULTICELLULAR DYNAMICS WITH SINGLE-CELL MICROPATTERN CLUSTERS

**LIN LAIYI**

*B.SC. (HONS.), NUS*

**A THESIS SUBMITTED FOR THE DEGREE OF**

**DOCTOR OF PHILOSOPHY**

**NUS GRADUATE SCHOOL FOR**

**INTEGRATIVE SCIENCES AND ENGINEERING**

**NATIONAL UNIVERSITY OF SINGAPORE**

**2014**

# Declaration

**I hereby declare that this thesis is my original work and it has been written by me in its entirety. I have duly acknowledged all the sources of information which have been used in the thesis.**

**This thesis has also not been submitted for any degree in any university previously**

**Lin Laiyi**

**1st December 2014**

# Acknowledgements

First and foremost, I would like to acknowledge A*STAR graduate academy (AGA) for their generous scholarship funding which granted me the opportunity to pursue a PhD course in the National University of Singapore. My heartfelt gratitude goes out to my supervisors Prof Chwee Teck Lim and Prof Jean Paul Thiery for their support and insightful discussion without which the completion of this thesis would not be possible. My heartfelt thanks also go out to Dr Isabel Rodriguez for her guidance in the development of the cell-positioning platform and I have definitely benefited much from her vast experience in microfabrication. I would also like to thank my TAC chairman Prof Zhang Yong for spending time to attend the TAC meetings and carefully pointing out areas in my work that could be improved on.

In addition, I would also like to thank Dr Yeh-Shiu Chu for his constructive suggestions and mentoring at the early stages of my PhD study. Special thanks also goes out to Vincent Lim from SnFPC, IMRE for his help in laser writing the multiple quartz masks that are essential to my work and Dr Lai Lai Yap from Biochemistry, NUS for her assistance in cell transfection. Kind assistance from the microscopy core, MBI and lab mates in Nano Biomechanics lab, NUS especially Man Chun Leong and Surabhi Sonam is also very much appreciated.

Finally, I would like to dedicate this thesis to my family and close friends whom I may have neglected due to the many hours spent in the lab. Their unconditional support has been very important in helping me pull through this grueling PhD journey.

# Table of Contents

2.2.2 Effect of cell geometry and connectivity on single cell functions

2.3 Micropattern studies on multi-cellular systems

## Chapter 3 Microfluidic Cell-positioning Platform

3.1 Introduction

3.2 Materials and methods

3.3 Results and discussion

## Chapter 4 Motility of Geometrically Constrained Cellular Clusters

4.2 Materials and methods

4.3 Results and discussion

**Chapter 5 Actomyosin-mediated Contraction in Cellular Rings**

5.2 Materials and methods

5.3 Results and discussion

**Chapter 6 Conclusions**

# Summary

Physical cues have been known to exert a considerable influence on cell behavior such as multi-cellular dynamics in morphogenesis and epithelial void closure. The developing embryo is characterized by several well-defined geometries where physical cues had been proposed to play a critical role. Openings or voids in the epithelium can prevent it from performing its barrier-forming function effectively and a prompt and efficient mechanism to close these voids is crucial. Actomyosin-mediated cell contraction is one of two established mechanism in closing epithelial voids and its efficiency is also thought to be closely influenced by physical cues.

In this thesis, it is hypothesized that the size, shape and arrangement of individual cells in close proximity would regulate cell rearrangement and epithelial void closure and are force-mediated. By focusing down to the physical cues exerted on the single cell level, physical principles governing the dynamical behavior of these multi-cellular systems may be revealed. To achieve this, simple clusters of micropatterns that can accommodate a small but fixed number of cells with possible control of the geometry, adhesion and arrangement of individual cells were designed.

To seed a fixed number of cells at precise position on each micropattern cluster is not trivial. Random seeding of cells is uncontrolled and relies on chance that cells will be seeded in the right positions in the micropattern clusters. Hence, the positioning efficiency is low and further decreases as the number of cells required in the clusters increases. To improve positioning efficiency, a novel microfluidic platform containing an array of sieve-like cell traps was developed to control the positioning of single cells on these micropattern clusters. The platform showed a 4-fold improvement in the efficiency

of positioning cells on paired micropatterns and a highly significant 40-fold improvement for a 6-pattern ring compared to random seeding.

For a deeper understanding of cell movements during morphogenesis, further work needs to be done to understand the physical principles that govern cell motility. Using bowtie-shaped micropatterns, the rotation potential of 2-cell systems under different geometrical conditions was characterized. Together with selective inhibition of cell contractility and based on previous studies by others, a proposed force-mediated mechanism governing the rearrangement of geometrically constrained cell clusters was described. The principles revealed in the cell-pair experiments were further verified in a 3-cell model system that is closer to *in vivo* conditions.

To enable actomyosin-mediated epithelial void closure to be examined without conflicting signals from cell proliferation and rearrangement, an *in vitro* experimental system using cellular rings comprising only a single row of 4- to 6- cells was introduced. Using these cellular rings, the effect of geometrical cues from single cells (e.g. cell number and initial cell area) as well as other global geometries (e.g. shape and size of void at the center of the ring) on the actomyosin-mediated contraction dynamics of the cellular ring was investigated.

# List of Tables

# List of Figures

# Abbreviations

| | |
|---|---|
| 2D | 2-dimensional |
| 3D | 3-dimensional |
| BSA | Bovine serum albumin |
| CCD | Charge-coupled device |
| DI | Deionised |
| DIC | Differential interference contrast |
| DNA | Deoxyribonucleic acid |
| ECM | Extracellular matrix |
| EDTA | Ethylenediaminetetraacetic acid |
| EMT | Epithelial-mesenchymal transition |
| ESC | Embryonic stem cells |
| FAK | Focal adhesion kinase |
| Fig. | Figure |
| FRAP | Fluorescence recovery after photobleaching |
| HUVEC | Human umbilical vein endothelial cells |
| LCST | Lower critical solution temperature |
| MAP | Mitogen-activated protein |
| MDCK | Madin-Darby canine kidney |
| MLCK | Myosin light chain kinase |
| mRNA | Messenger ribonucleic acid |
| MRTF-A | Myocardin-related transcription factor A |
| MSC | Mesenchymal stem cells |
| PBS | Phosphate buffered saline |
| PDMS | Poly (dimethyl siloxane) |
| PEG | Poly (ethylene glycol) |
| PLL-g-PEG | Poly-L-lysine-grafted PEG |

| | |
|---|---|
| RIE-lag | Reactive ion etching lag |
| ROCK | Rho-associated protein kinase |
| S.E | Standard error |
| SEM | Scanning electron microscope |
| TEM | Transmission electron microscope |
| TGF-β | Transforming growth factor β |
| UV | Ultraviolet |

# Chapter 1

# Introduction

## 1.1 Background

### 1.1.1 Introduction to physical cues in cell biology

Mammalian cells *in vivo* are continuously exposed to numerous external stimuli and must respond in an appropriate and timely manner for maintaining homeostasis. Cellular response to external stimuli is mediated by a complex network of intracellular signaling pathways through molecular switches such as GTPases, kinases and phosphatases, which in turns governs and coordinates global cell function. An erroneous or delayed response from cells to these external signals can lead to the emergence and progression of human diseases [1]. In addition, understanding cellular response to external stimuli is also vital in the development of artificial tissues and organs, with its importance spanning across biomedical fields such as tissue engineering, design of medical devices and regenerative medicine.

Classical molecular biologists are interested in understanding how soluble biochemical factors such as hormones, cytokines or growth factors stimulate downstream signaling cascades in cells through ligand-receptor binding. However, physical cues are fast emerging as an important complementary candidate in determining how cells would react to its external environment. Unlike soluble factors where transduction of these biochemical stimuli are usually limited to ligand-receptor binding, physical cues are known to be sensed and transmitted throughout the whole cell machinery in a process known as mechanotransduction. Cell sensing of physical cues can be either force-based (e.g. in the stretching of a cell) or surface-based (e.g. in cells resting on nanotopographical surfaces) and a variety of physical mechanisms have been proposed to describe how these mechanical cues are transduced to biochemical signals in the cells [1,2]. Force sensing by cells can be accomplished through force-induced physical changes in intracellular structures such as localized conformational changes of force-sensing proteins such as α-catenin, p130Cas and talin, opening and closing of mechanosensitive ion channels or stabilization/destabilization of cell-cell and cell-matrix adhesion bonds. Geometry sensing has been explained by curvature sensing on topographical surfaces and the clustering and distribution of cell-substrate adhesion proteins such as integrins. For example, clustering of cell-adhesive proteins could promote focal adhesion assembly which then encourages cytoskeleton remodeling in a feedback mechanism. This will further activate biochemical cascades in downstream signaling pathways (e.g. RhoA and FAK pathways) which can have significant effect on global cell behavior such as proliferation and differentiation.

For the past two decades, the advent of soft lithography technology and subsequent explosive advancements in the development of soft, flexible substrates, microfluidic platforms and microfabrication technologies to engineer well-defined surface topography or geometrical confinement have enabled the study of specific physical cues to be performed conveniently. For example, microfluidic platforms have been routinely used in flow-based assays to investigate the influence of shear stress on a monolayer of adherent cells while controlled tensile or cyclic strain can be applied to cells adhered on soft substrates. Small changes in the fabrication recipe of soft substrates can also reproducibly generate substrates of varying stiffness which are ideal for comparison against the classical petri dishes in determining the effect of substrate stiffness on cell behavior. Physical cues are seldom applied to physiological cells in isolation and a combined application of a few different cues will better mimic *in vivo* conditions. For example, shear stress and cyclic strain were applied simultaneously to endothelial and epithelial cells in biomimetic microfluidic platforms such as the lung-on-a-chip device [3].

### 1.1.2 Types of physical cues and their effect on cellular behavior *in vitro*

Physical cues can be broadly categorized as either active or passive cues as shown in Fig. 1.1. Active physical cues mainly comprise externally applied forces such as cell stretching or flow-based shear stress while passive cues are generally material and/or surface-based. For example, substrate stiffness, surface topography and spatial constraints of cell adhesion are some of the more prominent passive cues reported. In this section, a brief overview of several types of physical cues is presented with key examples of their effects on cellular form and fate, ranging from cell morphology, survival, cell motility to cell differentiation.

Cells and tissues are continuously subjected to external forces *in vivo* and respond in various ways to these applied mechanical perturbations or 'loads' over time and space. A prominent example is the remodeling of bone micro-architecture in response to mechanical loading first described in 1892 [4]. Flow shear stresses are important hemodynamic forces experienced physiologically by endothelial cells and hence has generated considerable interests in elucidating how these cells sense and respond to blood flow. Endothelial cells had been found to elongate with their long axis aligning parallel to the direction of the fluid flow [5, 6] with reduced growth [7] and death [8] as well as altered levels of gene expression [9] when exposed to a laminar shear stress. Cell-type specific response to fluid shear stress had also been reported where fluid shear stress had been reported to enhance differentiation of mouse ESCs and progenitor cells into endothelial and cardiovascular lineages [10] while non-laminar shear stress had been reported to increase colon cancer cell adhesion to a collagen matrix [11]. Cells can react to stretching and compressive forces *in vitro* in a variety of ways. Morphologically, cells align perpendicularly to a uniaxial cyclic strain only if the strain is highly dynamic [12] (above 1 Hz frequency). Changes in intracellular activity such as increased expression of collagen and TGF-β in fibroblasts [13] and elevated levels of intracellular $Ca^{2+}$ in MDCK cells [14] had been observed under mechanical stretching. Mechanical loading can also induce stem cell differentiation into specific lineages depending on cell types and strain loading modes. For example, human MSCs differentiate into osteogenic lineages under cyclic uniaxial stretching and chondrogenic lineages under cyclic compression [10].

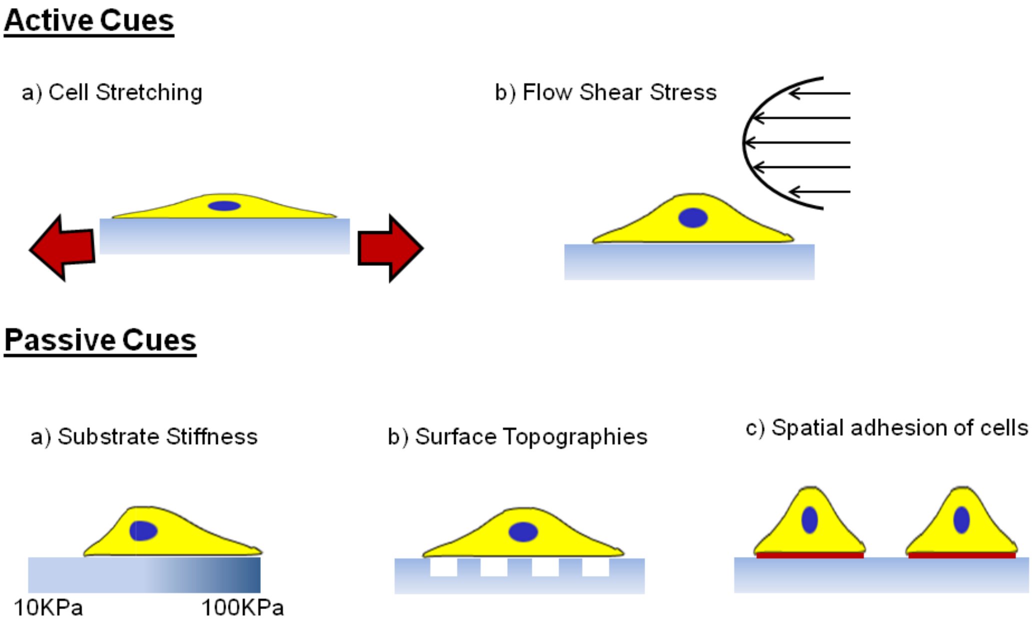

**Fig. 1.1.** Common physical cues in cell biology studied systematically in experiments.

Besides responding to an external force arising from fluid flow or stretching, cells also reacts to many passive physical cues that are material or surface-based. By creating experimental platforms to probe highly specific interactions between cell and bulk materials as well as at cell-material interfaces, systematic study of the cell-material crosstalk has been made possible. This important field of study has found applications in the development of novel biomaterials in guiding cell behavior and fate including highly attractive cell instructive materials [15] for tissue engineering and regenerative medicine.

Substrate stiffness is a widely studied material-based cue that has been known to physically stimulate a variety of adherent cell types, particularly fibroblasts and stem cells. Substrate stiffness has been known to affect cell-substrate adhesion where stiffer substrates encourage larger spreading area, higher traction forces by the cells [16] and well developed focal adhesions [17]. Cell dynamics is also modulated by substrate stiffness where fibroblasts had been shown to move slower [17] on stiff substrates but are more persistent and tend to migrate from a softer region to a stiffer one through durotaxis [18]. In stem cells, a landmark study had been performed where humans MSCs are cultured on collagen-coated polyacrylamide substrates with stiffness mimicking specific body tissues such as brain (~0.5kPa), muscle (~10kPa) and bone (~30kPa). These substrates of varying stiffness had been shown to guide MSCs differentiation into the particular cell type that they represent [19].

Aside from physical cues from bulk material properties such as substrate stiffness, the cell-substrate interface is also important in directing cell form and fate. *In vivo*, cells are exposed to various nanotopographic features such as the ECM fibrillar matrix that are absent in typical smooth substrates used in experiments. Cell adhesion [20] and alignment [21-23] are commonly studied cellular responses believed to be heavily influenced by surface topographies in most cell types. Dynamical behavior of cells is also highly influenced and shaped by surface topographies. Cell migrates faster along grooves [21, 24, 25] but move slower and more persistently on micro-sized pillars [26]. Lattice grid micropattern and disordered nanopits were also observed to direct MSCs towards osteogenic lineages [27, 28] while elongated features such as groove or nanofibers had been shown to direct MSCs and neural progenitor cells to differentiate into neuronal cells [29, 30].

Besides the two passive cues mentioned above, the patterning of cell-adhesive ECM molecules such as fibronectin, collagen and laminin are also known to exert physical stimulus by controlling the spatial adhesion of cells and consequently the cellular geometry and form.  Bow-tie shaped patterns had been designed to allow two triangular single cells to form a single cell-cell contact and are very useful in understanding how cell-cell interactions can affect cell behavior. With an excellent physical control of the geometry, adhesion and arrangement of single cells, systematic investigation of global cellular functions such as proliferation, differentiation, directed migration and neurite outgrowth have been made possible. Even though these single cell studies may provide vital clues in understanding cellular mechanoresponse, cells do not usually act alone in physiological tissues. Multi-cellular behavior on patterned substrates has been shown to be more complex and may even give totally different results from single cell studies. By seeding a large number of cells on a single pattern, cells are also subjected to highly localized cues from their immediate microenvironment. For example, cells at the pattern boundary are surrounded by fewer cells and have a lower number of cell-cell contacts compared to cells at the pattern center. These differences in local cues can in turn result in a highly anisotropic cellular behavior across the whole pattern. Besides looking at the asymmetric behavior of cells at pattern boundaries and at the pattern center, multi-cellular studies have also reveal much about the collective behavior of epithelial cells and how stem cells and muscle cells behave in a multi-cellular environment. As this form of physical cue would be used and explored further in this thesis, a more detailed description of the spatial patterning of adhesion molecules and their effects on single cells as well as multi-cellular form and fate will be given in the next chapter.

### 1.1.3 Physical cues in morphogenesis

The shaping of tissue and cell layers had fascinated developmental biologist over hundreds of years. Developing organisms had been known to formed well-defined shapes at different stages of development which are important in organ formation. However, the precise laws that govern the formation of these specific geometries are still poorly understood. Even in widely popular developmental biology textbooks such as “Developmental Biology” by Scott F. Gilbert [31], information relating to these specific morphogenic geometries is still mainly descriptive in nature. Early scientists attributed the establishment of these well-defined tissue geometries to Darwinistic evolution. However, as early as 1915, physical mechanisms had been proposed as a possible means of shaping tissue geometries by D’Arcy Wentworth Thompson in his highly acclaimed book “On Growth and Form” [32]. Thompson called to attention the remarkable similarities between biological form and behavior of materials under mechanical forces and proposed the use of simple mathematical transformation such as shearing as a means of shaping cell assemblies. Mechanical forces are important in driving cell motility which in turn may contribute to the shaping of defined geometries during morphogenesis. In 1969, John Philips Trinkaus wrote his landmark text “Cells into Organs: The Forces that Shape the Embryo” [33] which underlined the importance of multi-cellular motility in developmental processes *in vivo*.

In the last two decades, there is a shift in focus to understand the biomolecular origins of tissue shaping. Gradients of signaling molecules from the Hedgehog (Hh) family, the Wnt family and the TGF-β family had been identified as key to shaping developing tissues [34]. However, exactly how these families of signaling molecules participate in physically shaping the developing organism is still unknown. More recently, there has been a growing interest to revisit the physical aspects governing morphogenesis. In shaping tissue geometries by cell motility, the stability of cell-cell adhesions and regulation of actomyosin contractility by Rho GTPase are identified as key mechanical players [35, 36]. As the developing tissue is made up of an assembly of a large number of cells, it is not surprising that the modulation of cell-cell adhesion between these cells would be an important first step in enabling the remodeling of the cell layer. However, our knowledge of physical principles governing multi-cellular rearrangement and motility is presently limited to these general rules. Exactly how actomyosin contractility and cell-cell adhesion physically contribute to cell motility and in turn the shaping of the body plan needs to be further examined.

### 1.1.4 Physical cues in epithelial void closure

Besides morphogenesis, physical cues had also been implicated in the closing of epithelial voids. Epithelia are found in most organs to primarily serve as a protective layer for the underlying stroma. Epithelial cells have unique properties to establish well differentiated junctional complex including tight junctions, adherent junctions and desmosomes and a unique set of protein complexes ensuring apico-basal polarity However, some cells in the epithelium may sometimes be destroyed or extruded *in vivo* due to constant exposure to physical trauma, toxins, oncogenic events or even during naturally occurring events such as the remodeling of the epithelium. This creates openings or voids in the epithelium that prevents it from performing its barrier-forming function. To maintain the epithelium barrier integrity, wounded areas in the epithelium must be repaired promptly and efficiently and a comprehensive understanding of how this repair is achieved could be of great value in biomedical and pharmacological applications.

Two distinct physical mechanisms have been proposed so far to describe how cells behave to close these openings in the epithelium. Early studies about half a century ago investigating the behavior of fibroblasts in wound healing assays [37] had already proposed that epithelial cells promptly respond to any opening in the cell sheet by extending lamellipodia in the wounded area which is then followed by cell crawling to seal the opening. This mechanism is characterized by cell migration and appears to be modulated by Rac activation [38]. About 20 years ago, localized concentrations of actin, myosin II, villin and tropomyosin molecules were observed within 5 mins of void formation as a ring around the wounded area [39]. This actomyosin ring had since been termed as an actomyosin 'purse string' as the generation of circumferential tension by this ring pulls the cells bordering the void together in a coordinated motion that is analogous to the drawing of a purse string. As opposed to the first mechanism, this mechanism is characterized by a contractile leading cell edge free of lamellipodia activity and appears to be modulated by Rho activation [40]. A general consensus states that at large void sizes of at least tens of cell diameters, cells tend to close the void by cell crawling and a transition to actomyosin-based contraction occurs at smaller void sizes of a few cell diameters which eventually seal the epithelium. An interesting study performed using bovine corneal endothelial cells suggested a key contribution of ECM in governing the behavior of cells bordering the wounded area [41]. In this study, the presence of ECM appeared to encourage void closure by cell migration while the actomyosin contraction-based mechanism dominated in regions devoid of ECM.

Despite substantial studies on the global mechanism of void closure by physical players, little work had been done to probe the contribution of individual cells. Even for studies done on global void geometry, the results obtained might be confounded by the rearrangement and proliferation of cells that were not directly involved in the formation of the actomyosin ring. For example, cells up to 10 cell rows back from the void could respond to the presence of a void in the cell layer through cell rearrangement and proliferation.

## 1.2 Hypothesis & Aims

In this thesis, it is hypothesized that the size, shape and arrangement of individual cells in close proximity would regulate cell rearrangement and epithelial void closure and are force-mediated. Micropatterns of ECM proteins are able to spatially constraint cell adhesion, allowing the geometrical effects of cells to be systematically examined. However, micropatterns studies whereby cell geometries and environment are precisely controlled rarely go beyond two cells, with only one study found so far using a 3-4 cell clusters with controlled area and shape [42]. In studies on multi-cellular systems such as collective cell migration, tens to hundreds of cells are seeded on a single large cell-adhesive region of more than 10,000 $\mu m^2$. Geometrical constraint is designed to be applied on the whole multi-cellular collective with little or no control of the spatial properties of individual cells. Although, it has been shown that the overall geometry of these multi-cellular systems can influence their behavior and properties, it remains to be seen whether the geometrical and environmental cues from individual constituent cells can also affect this behavior in a meaningful way. Size and shape of single cells have already been shown to modulate the generation of cellular forces while the arrangement of cells in a multi-cellular system would likely affect the force distribution. By controlling these parameters and hence the forces present in multicellular systems, the global dynamics of these systems could be regulated.

To facilitate this study, simple clusters of micropatterns that can accommodate a small but fixed number of cells with possible control of the geometry and arrangement of individual cells were designed. This novel way of designing micropattern clusters could enable us to engineer simple cell model systems to study how the physical parameters of individual cells can affect global multi-cellular dynamics. One of the constraints identified in the use of these micropattern clusters lies in the difficulty in ensuring that the correct number of cells is seeded on these micropatterns at the right positions. To facilitate the efficient use of micropattern clusters in experiments, a microfluidic-based cell-positioning platform had also been developed.

**Specific Aim 1**:  Development of a microfluidic-based cell positioning platform for controlled positioning of single cells on ECM micropatterns.

**Specific Aim 2**: Using bowtie-shaped micropatterns, the rotation potential of 2-cell systems under different size and shape will be characterized. Together with selective inhibition of cell contractility and based on previous studies by others, a proposed force-mediated mechanism governing the rearrangement of geometrically constrained cell clusters is described. The principles revealed in the cell-pair experiments will be verified in a 3-cell system that is closer to *in vivo* conditions.

**Specific Aim 3**: Introduce an *in vitro* experimental system using cellular rings comprising only a single row of 4- to 6- cells to investigate actomyosin-mediated contraction dynamics without conflicting signals which are unrelated to forces generated by constituent cells. The effect of geometrical cues from single cells (e.g. cell number and initial cell area) as well as cell arrangement in the ring (global geometries e.g. shape and size of void at the center of the ring) will be investigated.

# Chapter 2

# Patterning ECM Proteins: A Literature Review

## 2.1 Methods of spatially patterning cell adhesive proteins

### 2.1.1 Overview

Very rudimentary efforts to spatially control the geometry of cells by manipulating cell-substrate adhesion had been reported as early as 25 years ago [43]. In these early studies, control of cell morphology (rounded or fully spread) was achieved by varying the concentration of ECM coating on the substrate. However, such crude methods of cell patterning did not allow precise control of the cell geometry and the differences in integrin clustering on ECM of different density would likely contribute to the different cellular response on these substrates. A more elegant method have since been developed which required the fabrication of cell-adhesive regions in a non-adhesive background. This method, first envisioned in a landmark experiment in 1994 [44], have since encouraged others to develop other more accessible and easy to use methods for patterning.

To date, the more common methods for selectively patterning of proteins can be broadly classified as elastomeric or surface modification methods and they have been the subject of several excellent review papers [45-47]. Elastomeric methods include micro-contact printing, microfluidic patterning and stencil patterning of proteins while surface modification methods can range from UV-based photolithography, laser ablation to plasma lithography. On the other hand, the background that resists cell adhesion usually also prevents protein adsorption and can be made up of very different classes of molecules such as poly(ethylene glycol)-terminated molecules, Pluronics, BSA or hydrogels where surface hydrophobicity appears to be a common property. The ability of these materials to remain inert under days of cell culture conditions is also of interest in studies requiring long term cultures [48,49].

### 2.1.2 Elastomeric methods

Making full use of the highly attractive soft lithography methods, mechanically soft elastomeric ‘stamps’, stencils or microfludic channels with micro-sized features corresponding to the regions to be patterned can be transferred with high fidelity from a re-usable mold as shown in Fig. 2.1. The material of choice is PDMS due to its superior biocompatibility, optical properties and ease of fabrication. To first create these micro-sized features on the master mold, standard microfabrication processes using photoresist and UV photolithography are needed. Microfabrication facilities are inevitably required but they are now available commercially or simplified versions of these facilities can be easily set up in classical biology laboratories.

Micro-contact printing is a method whereby PDMS stamps are used to directly transfer patterns from PDMS stamps with the desired features to the surfaces of culture substrates. In the first attempts to create micropatterned islands on culture substrates, elastomeric stamps had been used to transfer alkanethiols onto specific regions on gold substrates and the remaining bare regions were further passivated with a PEG-terminated alkanethiol that prevented protein adsorption. When exposed to a solution of the laminin ECM proteins, only the non-PEG regions allowed protein adsorption and cell adhesion and spreading were confined to these regions [44]. In this way, surface hydrophobicity can be easily be tuned on alkanethiols to either absorb proteins (e.g. hexadecanethiol) or repel them (e.g. oligo (ethylene glycol)-terminated alkanethiol) by controlling the terminal group on the alkane chain, making them an ideal class of molecules used by several groups [50-55]. Even though alkanethiols are commonly used as an intermediary for patterning proteins, stamping proteins directly onto culture substrates without the need for gold surfaces may be more advantageous [56]. Generally, for a good transfer of proteins from stamp to substrate, the protein should have higher affinity for the substrate than the stamp. Factors such as surface chemistry of the stamp and substrate, drying and stamping time and temperature need to be well controlled for highly efficient protein transfer. For example, plasma treatment of the stamp is commonly carried out to reduce protein affinity to the stamp. Recently, a study comparing protein transfer from PDMS stamp to polyacrylamide gels at room temperature and 37 °C showed that microcontact printing was more efficient at a higher temperature [57].

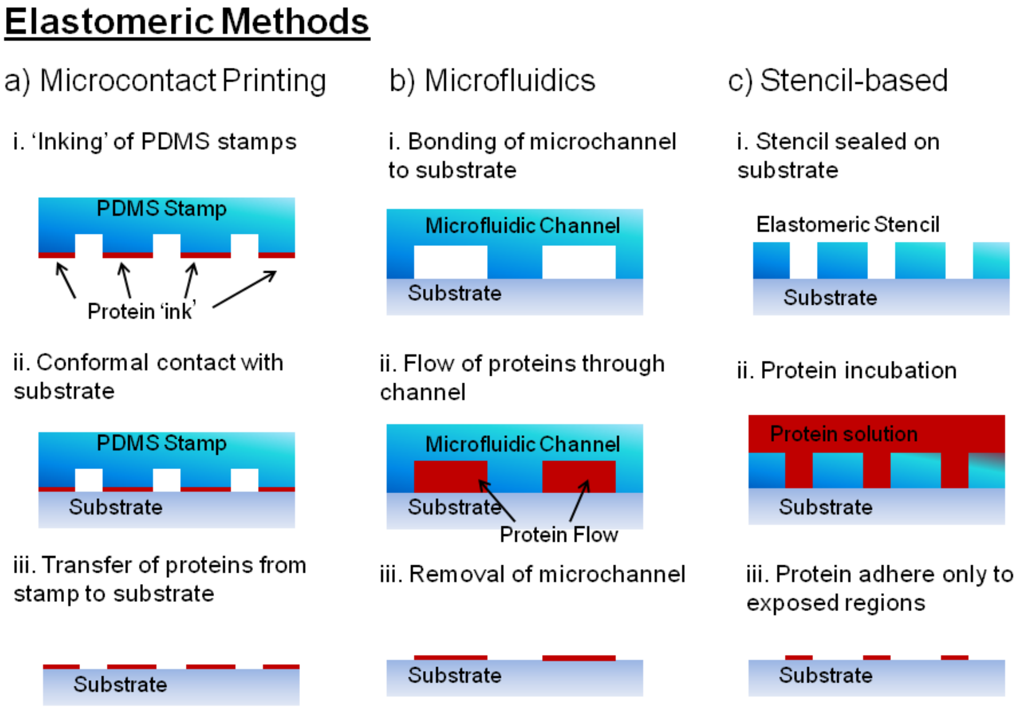

**Fig. 2.1.** Common techniques of protein patterning: Elastomeric methods.

In contrast to microcontact printing where inking materials are deposited in regions in contact with the stamp, PDMS microfluidic channels can be used to deliver solutions to regions where the PDMS do not contact the substrate. These solutions are usually drawn through the channels by capillary forces and can contain proteins for direct patterning or curable materials such as agarose for creating small microwells after the microchannels are removed. For example, bow-tie shaped microwells which have been used predominantly in cell-cell interaction studies can be fabricated in this way. These microwells can be further functionalized for cell adhesion and at the same time act as physical barriers to spatially constraint cells [58]. The microfluidic method of patterning proteins is not frequently used but may offer many advantages such as a greater control of the density of proteins deposited as compared to microcontact printing and is also an easier method to pattern multiple types of proteins in parallel.

Stencil patterning is another straightforward method to pattern substrates. The stencils used are usually fabricated by spin-coating a thin membrane of elastomeric materials such as PDMS on a mold with micro-pillars or by physical etching of parylene. Similar to the principles of conventional ‘lift off’ process used in the selective vapor deposition of metals, these elastomeric membranes with designed arrays of micro-sized holes are placed on the substrate to physically restrict protein adsorption to only the exposed areas. After the patterning step, this membrane can be manually removed, leaving behind the desired patterns on the exposed areas [59]. Cells can also be directly confined in the holes of the stencils. For example, cells had been successfully confined by using PDMS stencils sealed on both dry culture substrates and wet collagen gels [60]. More advanced patterning of cells and a protein have also been demonstrated using stencil patterning. For example by using a 3-layer parylene stencil system, murine ESCs had been co-cultured with up to four distinct types of cells [61].

### 2.1.3 Surface modification methods

Surface modification methods encompass UV-based photolithography, laser ablation and plasma treatment of surfaces as shown in Fig. 2.2. UV-based photolithography has been used for decades in the microfabrication industry where photo-activatable resists is exposed to UV light through an opaque chrome mask with selective transparent regions. The solubility of the resist in a developer solution is modified upon UV exposure and is either removed or retained after a development step depending on whether a positive or negative resist is used. Taking advantage of this established method and also other standard microfabrication techniques such as oxide etching and lift off process, contrasting protein-adhesive and non-adhesive regions can be created. For example in a method known as selective molecular assembly patterning, a photoresist layer is first spin-coated over a film of $SiO_2$ overlaying a $TiO_2$ layer and desired regions in the photoresist were removed by a standard photolithography process. This photoresist layer then acts as a mask for selective etching of the $SiO_2$ film which can be made protein resistant while the exposed $TiO_2$ layer is made favorable for protein adsorption [62]. For simpler methods of patterning proteins without the use of resists and organic solvents, surface chemistries can be directly modified by deep UV irradiation on biocompatible materials such as PEG [63], polystyrene or chemically-synthesized molecules with photo-activatable groups. Examples of photo-activatable groups can include protein-repelling groups that can be cleaved by photoactivation [64] or even caged groups where protein-adsorbing groups are exposed upon irradiation [65]. A very simple method of patterning protein on PLL-g-PEG coated substrates had been developed where the protein repelling carbon groups on PEG are modified into protein adsorbing carboxyl groups by irradiation with 185nm UV light [63]. This attractive and handy technology has spin-off a commercial company Cytoo which offers fabrication services for user-customized micropatterned coverslip.

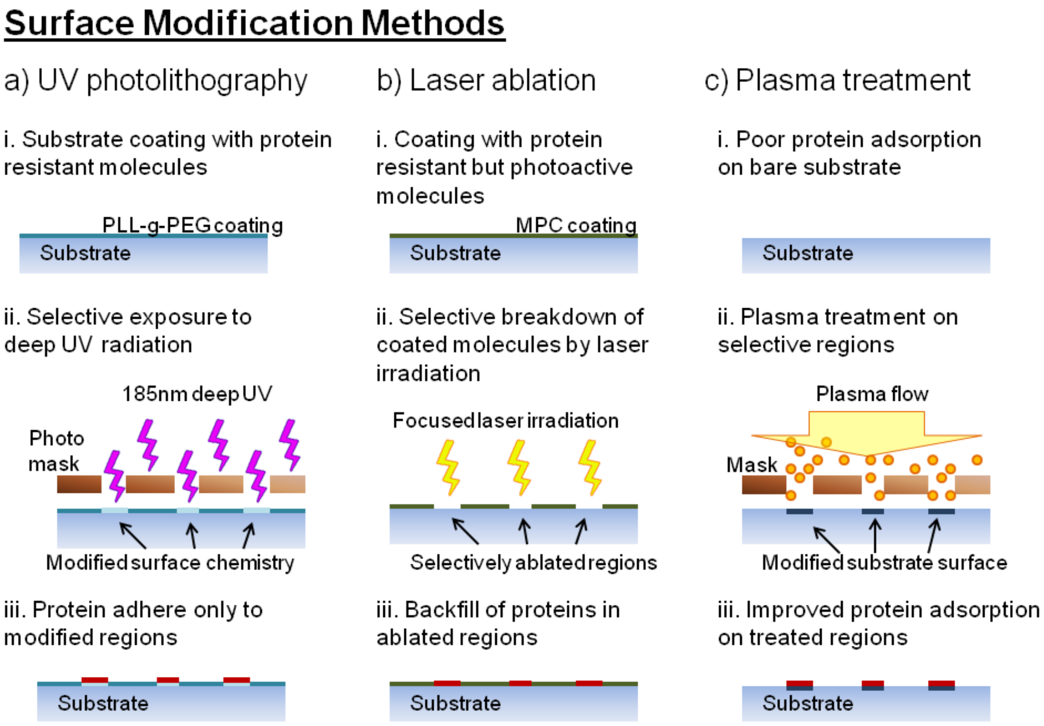

**Fig. 2.2.** Common techniques of protein patterning: Surface modification methods.

Besides using UV illuminations to modify surface chemistries, direct ablation of non-adhesive surfaces with concentrated laser beams have also been shown. Protein resistant but photoactive polymers such as poly (ethylene terephthalate) or 2-mcethacryloylocyethylphosphorylcholine (MPC) absorb the irradiated laser and undergo either a direct breakdown (photochemical) or gets heated up to temperatures that decompose the material (photothermal). Removal of these protein-resistant polymers at specific positions allows a backfill of cell-adhesive proteins in the ablated sites [66]. In addition, since this ablation process can be carried out in aqueous culture conditions, interesting on-demand patterning are possible. In reported experiments, cells were first confined in micropatterned islands and further ablation was carried out to either create migration lanes or to allow the co-culture of a 2nd cell type in close proximity [67]. Optical interference property had been used to generate a large area of parallel linear patterns by using 2 coherent laser beams to selectively ablate regions under constructive interference [68]. Instead of creating patterns on protein-resistant layers, laser irradiations had also been reportedly used conversely to inactivate selective areas of functional cell-adhesive proteins to restrict cell adhesion to unablated sites [69].

Another established method to modify substrate surface chemistry for protein patterning applications is the use of plasma lithography. Plasma are high energy charged particles produced from ionization of gases (e.g. oxygen) that are able to change or substitute surface atoms and functional groups and also to a certain degree, perform etching on some materials for the generation of surface topographies. Selective treatment of the surface by plasma is guided by a mask in tight conformal contact to the substrate which typically improves protein adsorption in exposed areas [70,71], although it has also been used alternatively to destroy unprotected regions of cell-adhesive polylysine [72]. A wide variety of masks have been reported, ranging from TEM copper grids in early experiments, colloidal particles for creating sub-micron features, to even simple PDMS channels or stencils. These masks are usually static but a motorized platform that enabled the mask to be mobile in the X-Y direction had recently been reported which allowed for on-demand plasma treatment and patterning of surfaces [73].

### 2.1.4 Advanced micropatterning

The methods described so far are designed to allow only one type of protein to be patterned across the entire substrate. However, multi-component protein arrays can be achievable through innovative modifications of these methods to allow high throughput cell-protein interaction studies to be carried out in parallel or to probe cell response to different proteins that are spatially separated. A method based on micro-contact printing used a multi-level PDMS stamp to perform stamping of different proteins over several steps without alignment [74]. Using microfluidic patterning, a multilayered microfluidic system was designed where different proteins or cells are flowed in each layer of the channel which contacted the substrate at different regions and patterned these regions differently [75]. Laser ablation techniques are well suited for this purpose due to its ability to modify desired regions on demand. Recently, laser irradiation of selective regions of photocleavable oligohisitidine peptides had allowed subsequent conjugation of His-tagged proteins only at the pre-irradiated sites and multiplex protein patterning is achieved over several irradiation and conjugation cycles [76].

Cell-adhesive proteins patterned using the methods described above are typically static and cannot reproduce the rapidly changing microenvironment that a cell experiences *in vivo*. To facilitate the temporal study of cellular events, patterning methods where cell adhesion to substrates can be reprogrammed on demand will be very attractive. Besides studying cellular activities such as cell migration, these reprogrammable substrates also allow the creation of new patterns without the detachment of adhered cells and are ideal for co-culture applications. Synthesizing switchable molecules for use in reprogrammable substrates is attracting great interest and a growing catalog of these materials has been reported. Switching of these molecules between cell-adhesive and non-adhesive chemistries can be mediated by a variety of external stimuli such as via electrical, thermal or photochemical means. Electrochemically switchable surfaces are commonly made from alkanethiol SAMs on gold surfaces. For example in a pioneering study to control cell adhesion with electrical means, hydroquinone-terminated alkanethiols were oxidized electrochemically, making them highly reactive to cyclopentadiene-tagged proteins [77]. In another key study, PEG-terminated alkanethiols were detached electrochemically from the substrate to improve cell adhesiveness on previous inert areas [78]. Materials that undergo LCST phase transition are excellent for use in creating thermally switchable environments as material and surface property change conveniently with temperature. For example, Poly (N-isopropylacrylamide) (PIPAAm) is a popular material which switches from a hydrophilic to hydrophobic at its LCST temperature of 32°C and had been use for co-culturing purposes [79]. Light responsive substrates are typically made from molecules with photo-activatable groups such as azobenzene derivatives, nitrospirobenzopyran and 2-nitrobenzene. One example of such substrates involved the absorption of protein resistant BSA to a layer of silane molecules functionalized with 2-nitrobenzene groups. By selective photocleaving of the 2-nitrobenzene groups using 365 nm UV beams, cell migration lane could be created on demand [64]. Again, laser-based techniques, with its superior spatial and temporal control, are found to be suitable for creating reprogrammable substrates. In a recent example, Q-switched laser system was used to induce localized oxidation of PEG layers to switch it from protein resistant to protein adhesive state for use in modifying cell shape on demand [80].

## 2.2 Micropattern studies on single cells

### 2.2.1 Overview

#### 2.2.1.1 Pioneering work

With the advent of revolutionary microcontact printing method for stamping alkanethiol on gold surfaces [44], pioneering work on how the size of micropatterned islands affect the growth and death of capillary endothelial cells were carried out [81]. Single cells confined in these micropatterned islands have well-defined shape and size that can be reproduced reliably. This allows highly controlled experimental platforms to be set up for a systematic investigation of the effect of cell geometry on cellular function. Using this attractive experimental method, cells were found to grow better when allowed to spread to large areas but switched to apoptosis when spreading is restricted [81].

#### 2.2.1.2 Assembly of focal adhesions and cytoskeletal network

In addition to showing an immense effect on cell survival, cell geometry and size can also tightly regulate localized intracellular cell behavior such as the assembly of focal adhesions and the alignment of the cytoskeletal network. After initial success in understanding cell survival using micropatterned surfaces, attention was turned to how focal adhesion formation could be correlated to the cell geometry [52]. By comparing focal adhesion assembly of capillary endothelial cells which spread over a single pattern with those that spread to the same area over several smaller patterns, the authors were able to decouple the effects of spreading area and cell-matrix adhesion. They showed for the first time that focal adhesion formation scaled with spreading area instead of the amount of ECM. Follow up studies had been done to test the strength of focal adhesions of micropatterned cells using a spinning disk device. An increase in cell-substrate adhesion and focal adhesion formations with an increase area was reported. Besides being influenced by spreading area, the authors also observed a strengthening of focal adhesion over time [52, 82]. Cell shape can frequently direct how the cytoskeleton is orientated in a cell. In a comprehensive study on how local features and overall aspect ratio of cells affected the structure of its cytoskeleton [83], it was observed that concave features promoted the localized assembly of stress fibers (mainly at the cell cortex) while convex features encourage lamellipodia activity. Anisotropic distribution of lamellipodia activity and actin localization first observed at the corners of square-shaped cells in 2002 [84] was also revisited in this study. As the aspect ratio increases with the cell elongating from a square to rectangular shape, this anisotropic distribution became more pronounced. More recently, by constraining cells to triangular geometry of the same size, microtubule growth towards focal adhesions at the triangle vertices were shown to follow a guidance mechanism where the orientation of the microtubules evolved from being highly random at the nucleation sites to an ordered one nearer the vertices [85].

#### 2.2.1.3 Decoupling effects of cell shape and cell-matrix adhesion

In most studies involving micropatterns, the whole cell fully resides on top of an ECM protein layer. However, this may not be the case *in vivo* due to the heterogeneity and fibrillar nature of the ECM matrix in the body tissues. A fully adhered cell also suffers from conflicting signals between cell shape and amount of cell-matrix adhesion. To overcome these limitations, a unique approach to micropattern studies used various protein pattern shapes (e.g. T, V or Y shapes) that allowed a single cell to spread across gaps in the ECM pattern as shown in Fig. 2.3.a. From Fig. 2.3.a, it is clear that even though the distributions of ECM in the patterns are very different, the shape of the fully spread cell remains similar. This method had proved to be highly informative, significantly improving our understanding of the impact of cell-adhesive matrix on how a spreading cell determined its final shape, how cell polarity was established and more importantly, how the cell division axis was orientated. In studies on cell shape determination, cell borders linking two cell apices tend to orientate in a distance-minimizing manner [86]. Focal adhesion accumulated on the pattern boundary and stress fibers originating from these focal adhesions reinforces the region devoid of cell-matrix adhesion and resists membrane tension. Following this result, anisotropic adhesive patterns were observed to able to guide cell polarity towards region of cell adhesion independent of cell shape [87]. It was proposed that an anisotropic cell-matrix adhesion encouraged cytoskeletal and cortical asymmetries that could affect the positioning of organelles such as nucleus and the golgi complex although the positioning of centrosomes appeared to be fixed, at least in the case of human retinal pigment epithelial cells. Interestingly, it was also reported that an ECM pattern shapes could guide the orientation of the cell division axis of HeLa cells [88]. Anisotropy in ECM distribution resulted in an asymmetrical network of retraction fibers which are formed between regions of ECM and the rounding cell as the cell entered mitosis. These retraction fibers were thought to play a significant role in orientating the cell division axis as they pulled on the astral microtubules causing a reorientation of the mitotic spindle until these pulling forces balanced out [89].

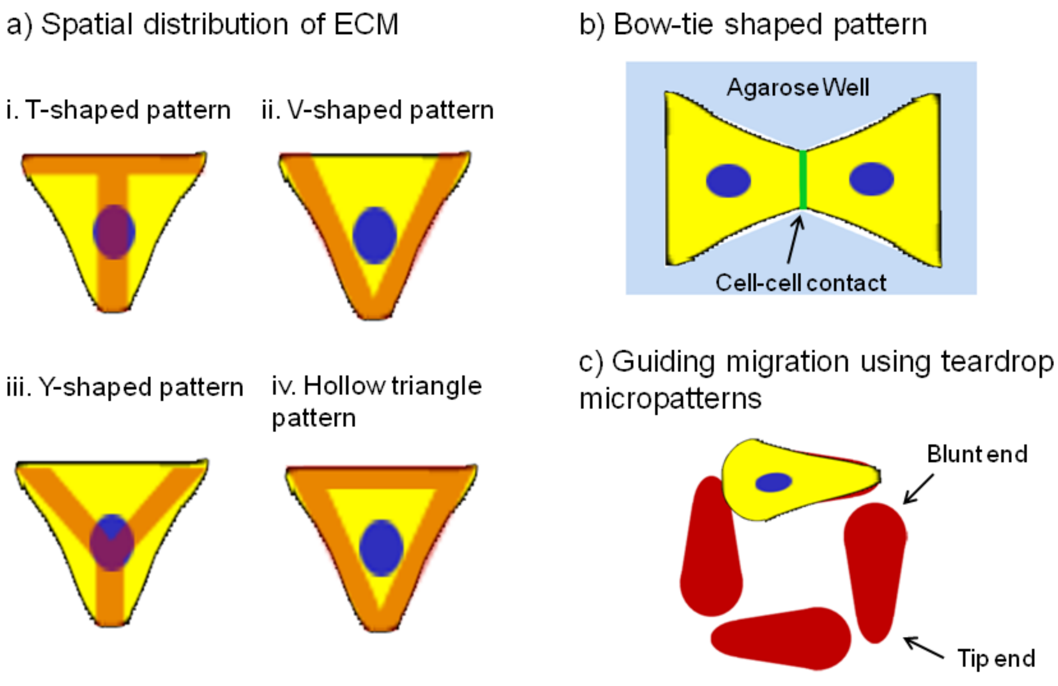

**Fig. 2.3.** Landmark use of protein patterning in single cell studies.

### 2.2.1.4 Cell-cell interactions

Besides varying the cell geometry and size, there is also great interest in understanding how cell-cell interactions could affect intracellular structures and global cell functions. In the simplest fashion, when two micropatterns each accommodating a single cell are placed in close proximity (~2-10 µm apart), a lone cell-cell contact can be engineered. ‘Bow-tie’ shaped micropattern had been used to allow a single cell-cell contact to be formed between two triangular-shaped cells as shown in Fig.2.3.b. By comparing a single cell of similar shape and size to a cell pair in the bow-tie, cell response due to geometrical signals could be effectively decoupled from those originating from cell-cell interactions.

For example, in a modified bow-tie shaped pattern (using square-shaped instead of triangular-shaped cells), single cells in contact were polarized with their nucleus closer to the contact and centrosomes orientated further away [90]. When the cells were released from confinement by electrochemically removing the passivated layer, the cells migrate away from each other. Several experimental works have adapted this successful micropattern shape for cell-cell interaction studies including this thesis research where the stability of a pair of single cells in a bow-tie shaped micropattern was examined as described in the next chapter. In other examples, similar patterns were used to probe the effect of cell-cell contact and cell size on the keratinocytes differentiation [50]. The authors found increase in differentiation markers observed in contacting cells as opposed to cells with no contact after both 48hrs and 120 hrs in culture although different cell size did not appear to regulate keratinocyte differentiation.

Instead of putting two cells together to observe the interaction of intercellular adhesion molecules in live cells, these molecules such as those from the cadherin family of proteins could be patterned directly on the surface.  A major advantage of such experiments is a far superior imaging of the interactions between the intercellular adhesion molecules as they are now in the conventional microscopic plane of view. This imaging advantage was employed in a study where transfected C2 cells expressing N-cadherin were seeded on N-cadherin substrates [91]. Cell-cell adhesion dynamics probed using FRAP analysis and time-lapse imaging of the initial stages of cell-cell contact formation and maturation allowed the authors to propose a model for how N-cadherin nucleates, grows and shrinks. The crosstalk between cell-cell and cell-substrate adhesion was also investigated by patterning alternating strips of E-cadherins and collagen and monitoring the lamellipodia activity, migration and traction force distribution of MDCK cells cultured on these strips [92].

With the successful demonstration of how spatial control of cell adhesion in single cells could have significant biological relevance, there were interest from various groups to look at global cell function in the same manner, particularly in the areas of cell proliferation, stem cell differentiation, directed cell migration and neurite outgrowth. These exciting areas of research constitute the major core of biological studies on single cells using micropatterned substrates and will be reviewed in greater details in the next few sections.

### 2.2.2 Effect of cell geometry and connectivity on single cell functions

#### 2.2.2.1 Cell Proliferation

Ever since the first landmark study on how cell size could affect cell growth and survival [81], the understanding of cell proliferation with the use of protein patterning has been a popular topic of research. A subsequent study used similar square-shaped micropatterned islands to demonstrate that the cell cycle transition from G1 phase to S phase was prohibited in cells where spreading was restricted [93]. Biochemical proliferative cues from growth factors and integrin binding are already well established to promote G1/S transition but these results clearly showed that geometrical cues also play an important role in cell growth. Geometrical cues appear to be transduced by FAK which plays a dual role in regulating cell proliferation [94]. In highly spread cells, FAK signaling is activated which induces a proliferative effect through RhoA and modulates cytoskeletal tension and focal adhesion through a feedback mechanism. In addition to cell spreading, cell proliferation has been shown to be dependent on cell-cell interactions. Conventional understanding of cell proliferation dictates that in high density cell cultures, cell proliferation is suppressed by a contact inhibition effect. However, in these confluent cultures, the number of cell-cell contacts is uncontrolled and the spreading area of cell also tends to be smaller than those in sparse cultures. To isolate the proliferative contributions of cell-cell interactions, bow-tie shaped agarose microwells had been used to precisely engineer a single cell-cell contact and control cell size and shape. A series of studies on cell growth using this experimental platform had collectively showed that a decrease in cell spreading area independently suppresses proliferation while cell-cell contact engagements were surprisingly able to stimulate proliferation through cell-specific signaling pathways [95-97]. In bovine pulmonary artery endothelial cells, VE cadherin engagement decreased cell spreading but also appeared to increase cell proliferation through a spreading independent mechanism [96]. This mechanism could be mediated by the Rho-ROCK pathway where cellular tension and the integrity of the cytoskeletal structure are crucial. In NRK-52E and MCF10A epithelial cells, an optimal cell culture density existed where proliferation was maximal [97]. In high culture density, cell proliferation was suppressed by low cell spreading independent of cell-cell interaction effects. In lower densities, engagement of E-cadherin increases cell proliferation through Rac1 signaling pathways which were mediated by cadherin binding of p120 catenin. To explore the effect of cell-cell interaction beyond a single contact, modified bow-tie shaped patterns were designed to engineer two or more contacts (e.g. three contacts for cells in the center of a ‘propeller’ shape pattern) and used dielectrophoresis to effectively position required cells on the patterns. The authors found that beyond a single contact, stimulation of cell proliferation by cell-cell contact engagement occured at a lesser degree [42]. Besides cell size and connectivity, cell shape has also been shown to affect cell proliferation. For example, using circular and elliptical micropatterns, proliferation of smooth muscle cells was found to be significantly lower in highly elongated cells compared to circular ones, probably due to a corresponding difference in nucleus morphology of these cells [98].

#### 2.2.2.2 Stem cell differentiation

Besides cell proliferation, stem cell differentiation is also tightly regulated by cell shape and spreading. Cell spreading has a huge impact on the cytoskeletal dynamics and tension generation in cells which could lead to highly cell-specific mechanisms affecting cell differentiation. Larger micropatterned islands promoted osteogenic differentiation in favor of adipogenesis in human MSCs and this dependence of lineage commitment on cell size appears to originate from RhoA activity and cytoskeletal tension [99]. Keratinocyte differentiation had also been observed to be regulated by cell size through the activity of the serum response factor (SRF). Larger cells contained higher levels of G-actin and SRF activity was inhibited. This in turn suppresses terminal differentiation in epidermal stem cells through downregulation of the JunB transcription factor [100]. When human MSCs were stimulated with TGF-β, differentiation specification into either chondrogenic or myogenic lineages was found to be dependent on the extent of cell spreading. If these stimulated cells were well spread, RhoA activity remained surprisingly unchanged but Rac1 activity and N-cadherin expression were upregulated which induces differentiation into smooth muscle cells [101]. Cell shape also affects stem cells differentiation by influencing localized tension sensing of cells where high localized tension was found to favor osteogenesis in mesenchymal stem cells [102, 103] and increased the expression of differentiation markers in epidermal stem cells [100]. Osteogenesis mediated by high localized tension appears to be transduced via RhoA pathway as in the same way as highly spread cells. Gene expression analysis on highly tensed cells cultured on star-shaped patterns also implicated MAP kinase pathways and noncanonical Wnt signaling in this sensing mechanism [103]. Aspect ratio is another important factor in guiding cell differentiation. In MSCs, an optimal aspect ratio of 1 and 2 had been reported for adipogenic and osteogenic differentiation respectively [102] while higher aspect ratios appeared to encourage myogenic differentiation [104].

#### 2.2.2.3 Cell migration

Dynamical cellular behavior such as cell migration can also be guided by pattern shape and configurations. On typical cell culture dishes, cell move in randomized directions but they can be directed to move in a bias way by asymmetrical shaped patterns. For migration to occur, cells have to be polarized with membrane extensions towards the leading edge and retraction of the cell body at the rear end. For this “front-back” polarization to develop, specific intracellular polarization in terms of distribution of actin filaments, focal adhesions and lamellipodia activity must first occur. Early studies investigated the dependence of lamellipodia extension on cell shape using different geometric forms and results had shown that cells preferentially extended their lamellipodia through sharp corners of these shapes [53], possibly due to a concentration of traction forces on these regions [84]. In symmetrical patterns such as circles, these molecular polarizations appeared to be transient. However in asymmetrical patterns, asymmetry of actin filament distribution was similarly short-termed but anisotropic distributions in focal adhesions and membrane activity tends to be more persistent [105]. In tear-drop shaped patterns, this symmetry breaking was observed to be orientated along the blunt-to-tip axis. Organelles such as centrosomes were also displaced from the cell center with the displacements directions similar to that observed in migrating cells. When the passivated layer was removed using electrochemical means, the cells tend to migrate towards the blunt end but not laterally, consistent with the direction of “front-back” polarization [54].

Guided migration is typically observed in the presence of gradient cues on unpatterned substrates. For example, in durotaxis, cells preferentially migrated from a softer substrate to a stiffer substrate. Other cues such as chemoattractants or cell adhesion strength can also direct where cells prefer to migrate. To guide cell migration using cell geometry-based cues, 4 tear-drop shaped patterns were arranged in a square with each pattern at right angles to each other [106] as depicted in Fig.2.3.c. It was found that this series of patterns was able to direct migration of fibroblasts and endothelial cells from one pattern to another at both the blunt end and the tip end. Migration speed appeared to be modulated by the gap distance between each pattern and migration bias was destroyed on a rectangular migration track where cells did not adopt a polarized shape. When a large number of tear-drop shaped patterns were arranged to form a circle, cells migrated continuously around the circular track in a persistent direction [107]. Inhibiting important regulators of polarity and motility such as Rac1, RhoA and Cdc42 affected migration speed but not the directional bias. In another similar study using MCF-10A epithelial cells, cell migrated most effectively by jumping sideways from the tip end of one pattern to the blunt end of the next pattern compared to other modes of jumping [108]. More recently, another study showed that the directional cues provided by asymmetrical patterns can be highly cell-specific, opening up the possibility of using them in cell sorting [109].

#### 2.2.2.4 Neurite outgrowth

Instead of modulating cell morphology to direct cellular dynamical behavior, neurite extensions can be guided using patterned grids in an attempt to mimic neuronal network circuits. For example, dorsal root ganglia cultured on laminin and poly-L-lysine grid patterns adhered mainly to the patterned regions with active neurite extensions following closely to the layout of the grid lines. Their cell bodies and neurites were GAP-43 positive which is similar to developing and regenerating neurons *in vivo* [110]. Patterned substrates could also provide valuable insights into how neurites could explore a large area scattered with high and low affinity ECM molecules. When an array of cell-adhesive spots was patterned instead of a continuous track, an inter-spot distance of 30 μm was found to prohibit neurite growth between the spots. Neurite growth and branching have been shown to have high affinity for laminin spots while fibronectin spots appeared to be less conducive for cell body adhesion, neurite branching and neurite growth. However, by mixing fibronectin and laminin spots in a multi-component substrate, fibronectin spots were observed to act as intermediaries to bridge two laminin spots > 30 μm apart, with no change in neurite extension velocity and length from pure laminin spots [111]. Recently, carbon nanotubes, which can form nanotopographical mesh structures while also having a strong affinity to poly-lysine, are emerging as an ideal candidate for patterning neural networks *in vitro*. Both topographical and geometrical cues can be conveniently applied which to guide neurite attachment and elongation in long term cultures [112]. Using well designed patterns, internal neuritic tension was found to be crucial in axonal polarization where one of the growing neurite exhibits increased growth rates at the expense of other neurites and acquire axonal characteristics [113]. Presence of this internal tension is confirmed using patterned curved lines which cause the detachment of growing neurites. In a Y-shaped pattern where the cell body resides in the pattern center with three growing neurites, there was no preference for axonal polarization when the angles between the growing neurites were made equal. Instead, if the angles between two of the neurites were 90°, the remaining neurite was under higher internal tension and tend to become the axon.

## 2.3 Micropattern studies on multi-cellular systems

### 2.3.1 Overview

Single cell studies on micropatterns, with its simplicity and precise control of cell morphology and connectivity make it a very attractive and reproducible experimental platform. Deservingly, micropatterns have been regarded as essential tools in the quest to understand how biological cells respond to their geometrical environment. However, cells do not exist in isolation in the body tissues. Even though single cell studies may have much value as a starting point for providing vital clues in understanding cellular response, the response of a collection of cells are much more complicated and may not be necessary similar to that of a single cell. For example, proliferation rates had been shown to first increase with the engagement of a single cell-cell contact but began to decrease as the number of contacting cells increased [42]. To recreate cellular behavior *in vivo*, adhesive patterns designed for tens to hundreds of cells are fast emerging as candidates for studying collective cell behavior in a multi-cellular environment. These patterns are much larger (>10,000 $\mu m^2$) and cells appears to experience highly localized environmental cues that may be very different at pattern boundaries and at the center of the pattern. For example, cells at the pattern boundary are surrounded by fewer cells and have a lower number of cell-cell contacts compared to cells at the pattern center. This could lead to very different behaviors exhibited by cells on the same pattern, which mirrors the heterogeneity observed in the body tissues.

By using computational modeling and experimental studies, a key study concluded that an ensemble of cells cultured on a geometrical pattern experienced a highly anisotropic distribution of mechanical stress depending on the pattern shape [114]. For example, in a square pattern, cells at the corners experienced higher mechanical stress compared to those at the sides while cells at the pattern center are under minimal stress. This appeared to be analogous to what was observed on single cells residing on square patterns where traction forces were concentrated at the sharp corners. Many global cellular behaviors such as proliferation and differentiation are dependent on cell tension as observed in single cell studies. Similarly, asymmetry in stress distribution in multi-cellular patterns had been shown to mediate a distribution of proliferation rates across the pattern with highly stressed cells growing faster. This is true for a wide variety of shapes ranging from squares, rectangles to an asymmetric annulus. A series of follow up studies had since been reported which suggest that this stress distribution also plays a crucial role in generating an anisotropic distribution of how stem cells differentiate, how epithelial cells undergo EMT and how fibroblasts migrate. For instance, when human MSCs were seeded on square patterns, highly stressed cells at the edge of the pattern committed preferentially to osteogenic lineages while cells experiencing lower mechanical stress at the pattern center underwent adipogenesis [115]. When mouse mammary epithelial cells cultured on square patterns were treated with TGF-β to induce EMT, expression of epithelial markers is higher for cells at the center of the pattern while mesenchymal markers were elevated in cells at the edge of the pattern [116]. Expression of mesenchymal markers by TGF-β stimulation and cellular tension appeared to be mediated by MRTF-A which is also observed to be localized in nucleus of cells only at the edge of the pattern. By using dynamic patterning methods, fibroblasts cultured in geometrical patterns were released from their confinement and cells were observed to preferentially migrate outwards from region where higher stress was expected [117].

Multi-cellular patterns can also exhibit anisotropic cellular behavior independent of mechanical stress distribution. First observed in single cell studies, engagement of the cadherin intercellular adhesion molecule was found to induce an off-centering of the nucleus and the centrosomes [90]. When extended to a multi-cellular study using astrocytes, epithelial and endothelial cells on large circular patterns, a polarized phenotype was also observed where the centrosomes of cells at the edge of the circle were preferentially positioned towards the free edge while those of cells at the circle center were randomly oriented similar to what was observed in isolated cells [118]. These polarizing patterns had been attributed to cadherin engagements which induce positioning of the nucleus and centrosomes away from the cell center by an interplay of forces associated with actin and microtubule networks. Besides looking at asymmetric behaviors of cells at pattern boundaries and at the pattern center, studying the behavior of multiple cells on patterned substrates have also reveal much about the collective behavior of epithelial cells and how muscle cells and stem cells behave in a multi-cellular environment. These prominent areas of research will be further reviewed in detail in the next section.

### 2.3.2 Collective behavior of epithelial cells

Epithelial cells rarely act autonomously as they are known to form highly cohesive units through closely-knitted cell-cell junctions. These cell-cell junctions are not only responsible for the integration of individual epithelial cells into the epithelium and the maintenance of the epithelium's structural integrity and barrier-forming functions, but also play a crucial role in the dynamic remodeling of the epithelium. For example, in typical wound-healing assays, a sheet of cells are known to move in concert with one another with the emergence of a few highly mesenchymal-like leader cells locally guiding a unit of follower cells. This process is known as collective cell migration and may be important in driving several physiological processes such as embryogenesis, wound-healing, cancer metastasis and even lateral cell migration in zebrafish. Even though single cell migrations have been extensively studied on micropatterns, the effect of geometrical cues on how a cohort of cells migrates collectively still needs to be established further.

Recently, collective cell migration directed along adhesive tracks of different width had been studied [119]. MDCK cells on narrow tracks were shown to move faster in a contraction-elongation manner while cells on wide tracks are slower and move in a vortex-like fashion. Loss of cell-cell contact and cell contractility abolished the dependency of migration speed and migration modes on track geometry. Using a similar experimental setup with parallel strips of fibronectin tracks separated by a narrow passivated region, migrating keratinocytes were observed to form highly tensed cell bridges spanning across adhesive tracks and suspended over the non-adhesive region [120]. These multi-cellular bridges could be described by an elastic model and might provide valuable insights on how cell sheets maintains its integrity and distributes tension during physiological processes with low cell-matrix adhesion. Patterning ECM strips have also been very useful in understanding contact inhibition of locomotion (CIL) where colliding cells tend to move away from one another. On patterned narrow strips, cells were only confined to migrations up and down the strips with frequent collision where head-to-head collisions of single cells were found to be most effective for CIL [121]. Collective cell behavior can emerge where single cells line up in a row and adhered to one another to form a “train of cells” that migrated and polarized in a coordinated manner. Besides using adhesive strips to study how cells behaved collectively, a persistent rotational motion of MDCK cells had also been studied in large circular patterns [122]. The emergence of this coordinated cell behavior was found to be dependent on cell density, pattern size and cell type. When mutant MDCK cells exhibiting mesenchymal characteristics were used instead, collective behavior becomes much less persistent while invasive breast cancer cells exhibit highly uncoordinated, randomized behavior. Interestingly, cells exhibit biased cell alignment and directional rotation that was strikingly cell-type specific on the inner and outer boundaries of ring-shaped micropatterns [123]. This directional bias appears to be strongly dependent on the integrity of the actin cytoskeleton where a complete reversal of the bias direction had been shown by experiments using actin–depolymerising drugs.

### 2.3.3 Stem cell niche

Apart from the collective cell behavior, many experiments on ECM patterns had been designed to probe how stem cells behave in a multi-cellular environment. The *in vivo* microenvironment or stem cell niche is crucial for the maintenance of the differentiation potential of stem cells or "stemness" and ECM micropatterned substrates are well placed to reproduce this microenvironment *in vitro*. In a very recent study, human MSCs had been shown to express higher levels of MSC markers on patterned circular islands than on typical unpatterned culture substrates. This effect on the cells persisted once it is established and remains even after release from pattern confinement for up to 16 days [124]. Patterned circular islands also restricted cell spreading and suppressed proliferation, both of which could be relevant in preserving cell stemness. High expression of MSC markers were typically observed in early passages and inhibition of cell tension by drug treatment have been shown to reproduce elevated MSC markers expression on unpatterned substrates. When human ESCs were cultured on circular pattern, cells at the pattern boundary were more proliferative but remain undifferentiated [125]. This results were confirmed by an up-regulation of β-catenin at pattern boundaries which mediates ESC expansion and self-renewal and also appears to be linked to an increased in Oct-4 expression in those cells. The size of circular patterns also generates important guidance cues in stem cell differentiation where smaller cell colonies had been reported to encourage ESCs differentiation through Smad1 signaling [126]. Human ESCs have also been cultured to confluency on these circular patterns before detaching them to generate embryoid bodies (EB) of defined sizes [127].

### 2.3.4 *In vitro* muscles

A large body of work has also been done on muscle cells for the creation of artificial muscle tissues *in vitro* which will be very useful in physiological studies, tissue engineering, therapeutics and pharmacological applications. To this end, micropatterned substrates are able to facilitate the formation of myotubes from myoblasts by effectively organizing and aligning myoblasts adhered to these substrates. For example, C2C12 cells cultured on vitronectin strips under serum-free conditions experienced heighten sensitivity to surface cues and were found to form single myotubes at an optimal strip width of 30 μm [128]. Multiple myotubes were formed on wider strips while myotubes formation was inhibited in narrow strips of less than 10 μm. By patterning C2C12 myoblasts on parallel rectangular islands that were highly elongated, myotubes formation tends to be more favorable compared to circular islands of the same size or unpatterned substrates [129]. The effect of pattern geometry in myotubes formation is further examined in a study which compares myoblasts differentiation in line, ring and hybrid patterns combining geometrical feature of both rings and lines [130]. The results showed that myoblasts on hybrid patterns were shown to exhibit the strongest differentiation parameters independent of cell density variations among the different pattern geometries.

# Chapter 3

# Microfluidic Cell-positioning Platform

## 3.1 Introduction

### 3.1.1 Motivation

In typical experiments involving micropatterned substrates, cells were seeded on these micropatterns by random seeding where single cells in suspension were added directly to the micropatterned substrates. The cells were allowed to sink down onto the substrate and might or might not adhere depending on where they land. If a cell encountered an adhesive region, cell-ECM interaction allowed the cells to be anchored to these regions but they remained in suspension otherwise. These events occur in a highly random fashion. For quantitative analysis to be carried out in cell studies, a large sample size is essential as this would average out any heterogeneity in the cell population. This would give a more accurate representation of cell behaviour in general.

In the next two chapters, each bow-tie region and trapezium pattern was designed to house exactly one cell. Although random seeding was convenient, the efficiency of obtaining micropatterns with the appropriate number of cells at the right locality was limited. Usable micropatterns for analysis were rare, especially for the ring arrangement of micropatterns used in Chapter 5. In these rings, at least 4 to 6 cells had to be seeded on the micropattern consistently in a well-distributed manner. Concentration of seeded cells in one section of the ring could still allow cellular rings to be formed via cell migration. However, this process may take a long time which could allow some of the cells to divide. Although cell division had been successfully harnessed to create cell doublets on micropatterns [131], it would not be useful in experiments that require a larger number of cells. Taken together, it appears that obtaining micropatterns with the same number of cells consistently is challenging, especially if the number of cells required is large. This may explain why published work in the literature is generally limited to at most two cells in the pattern. Hence for efficient use of micropattern clusters with more patterns, a method to deposit single cells at specific localities in a non-random manner would be first presented in this chapter.

### 3.1.2 Single cell manipulation methods

To handle single cell in a controlled manner, various techniques are available and more are constantly being developed due to an increasing demand for simple and efficient tools for single cell manipulation at high-throughput. Micropipettes and optical tweezers are established methods for handling single cells but suffer from low efficiency, being only able to manipulate one cell at a time. Very recently, two separate research groups have independently designed robotic automation platforms to greatly enhance the throughput of handling cell with micropipettes [132,133]. Microwells-based platforms with well sizes of about 20 µm are also commonly used for the isolation of single cells at high efficiency [134]. Instead of singe cell isolation, larger wells had also been used for multiple cell confinement although a much reduced efficiency was reported [135,136].

High throughput microfluidic arrays based on dielectrophoresis [137-140] or hydrodynamic fluid flow [141-144] are commonly used for trapping single cells in a fluidic flow at designated locations. Dielectrophoretic trapping uses a non-uniform AC field to electrically polarize suspended particles and the fluid medium. A net force is induced on the particles either towards (pDEP) or away (nDEP) from the electrodes depending on the dielectric constant of the particle and the medium. For cells in typical culture medium, the nDEP or negative dielectrophoretic forces present pushes the cells away from high field regions. Taking advantage of these induced forces, cell traps could be engineered by surrounding designated locations with electrodes. Notably, microelectrode arrays had been integrated with protein patterning to actively trap single cells on protein micropatterns. In this platform, pDEP or positive dielectrophoretic forces was utilized instead to trap cells in a sucrose medium [140] which enabled efficient coupling of electrodes and micropatterns.

Fluidic flow in a microfluidic channel is typically laminar and its flow path could be easily modified by the presence of microstructures such as sieve-like traps [141,142] or small side conduits [143,144] via a change in fluid resistance. Hydrodynamic trapping makes use of well-designed placement of these microstructures to control the passage of suspended cells flowing through the microchannel. Sieve-like traps literally ‘sieve’ out single cells when a cell suspension was flowed through them. Many of these traps were designed with gaps in them or between the traps and the substrate such that fluidic resistance in the trap vicinity could be changed depending on trap occupancy. These changes in fluidic resistance divert the fluid flow away from occupied traps and promote single cell trapping [141]. Sieve-like trap arrays reported in the literature are usually designed in closely packed configurations which are attractive for high-throughput trapping and analysis at the single cell level. Alternatively, side conduits incorporated at designated location in straight or serpentine-shaped channels diverts cell and fluid flow from the main channel. If these conduits were designed to be much smaller than the size of the cell, cells could be trapped at these locations. For efficient trapping of single cells, the overall fluidic resistances in these channels have to be carefully calculated so that fluid flow would bypass occupied conduits.

### 3.1.3 Design approach

In this chapter, a cell positioning platform which allowed the controlled positioning of single cells on micropatterns is presented (Fig. 3.1). An array of hydrodynamic sieves

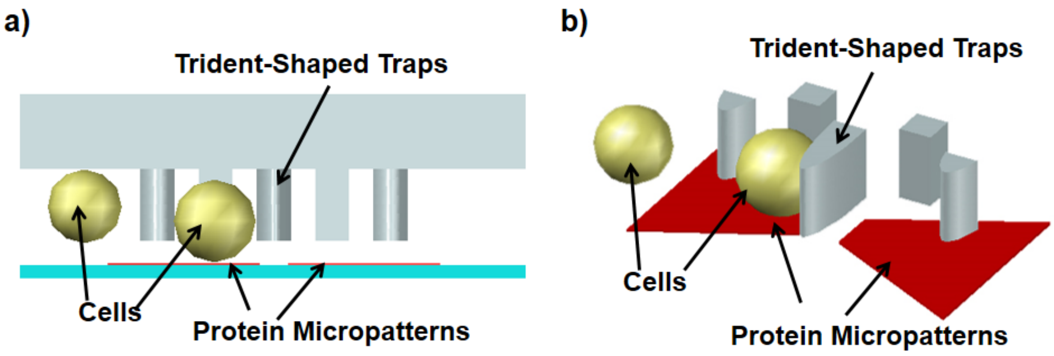

**Fig. 3.1.** Schematic diagrams showing how single cells could be controllably positioned on micropatterns using sieve-like traps in a microfluidic channel. a) Side view. b) Tilted view without the top of the microchannel.

enabled high throughput trapping of single cells at specific locations which could be coupled to micropatterns for efficient positioning of cells on these patterns. Sieve-like traps in a microfluidic channel were aligned onto the fibronectin micropatterns on a coverslip with high precision using a self-made alignment fixture attached to a fluorescent microscope. Cells suspended in culture medium were loaded into the device where single cells were captured by the sieve-like traps on top of the protein micropatterns. A gap was designed between the trap and the coverslip to provide space for trapped cells to attach and spread on the micropatterns but was designed to be too small to allow captured cells from escaping. Once the cell had spread sufficiently, the microfluidic channel was removed from the coverslip. This was done to prevent adhered cells from being pulled off by any shear forces that might be generated from the removal of the microchannel. Some platforms using dielectrophoresis [140,145,146] to position cells on adhesive substrates had also been reported in the literature. When compared to the platform proposed in this chapter, dielectrophoretic trapping involved considerable trapping forces and require cells to adhere in non-conventional media such as a sucrose medium. Also the set up for dielectrophoresis had to be permanently attached to the substrate which could limit accessibility for high-resolution imaging and subsequent manipulation. The cell positioning platform proposed in this chapter also have the advantage of being (1) easy to fabricate and set up, (2) compatible to a wide variety of micropattern configurations, (3) able to provide significant improvements over the current random seeding method, (4) able to preserve cell viability and (5) to facilitate further manipulation of the adhered cells and high-resolution imaging.

## 3.2 Materials and Methods

### 3.2.1 Fluid Modeling

3D computational fluid dynamics (CFD) analysis was carried out to find the optimal trap design that could best fulfil the needs of the platform. Sieve-like traps of different designs were created and meshed using GAMBIT 2.4.6 (Ansys Inc., 2006) and a value of 5 µm was used as the gap size between the trap and the bottom of the simulation space. 118,888 to 344,235 tetrahedral elements with skewness less than 0.8 were used in the mesh and mesh independence was ensured by increasing the mesh number until the average flow velocity around the trap differed by less than 0.7% when compared to a finer mesh. Flow characteristics around the trap were solved using FLUENT 6.3.26 (Ansys Inc., 2006) with a value of 2 mm/s for flow velocity at the inlet and iterated until convergence of the residuals to a precision of $1^{-05}$. A model which allows a two-way coupling between the continuous phase and the discrete phase was used in the calculations. The continuous phase was given the density/viscosity of water while the discrete phase was set to be 15 µm particles with the same density/viscosity injected at an initial velocity of 2 mm/s.

### 3.2.2 Device Fabrication

Silicon molds for the microfluidic chip were fabricated using typical microfabrication processes. 4” silicon wafers were spin-coated with AZ7220 photoresist and a laser-written glass mask was used to transfer the chip design to the resist via a 16s UV illumination and a 1 min development in AZ Developer. The developed photoresist acted as a mask to facilitate deep silicon etching of the wafer in selective regions using a Deep Reactive Ion Etching-Inductively Coupled Plasma (DRIE/ICP) system (PlasmaLab System 100, Oxford Instruments). Wafers were etched to a depth of 25 µm characterized by surface profiler (KLA-Tencor) measurements at regions corresponding to the microchannel walls. The wafer was then cleaned before silanization with heptadecafluoro-1,1,2,2-tetrahydrodecyl trichlorosilane under vacuum for 30 min at 80°C in a AVC-150M SAM coater system (SORONA). Microfluidic chips were replicated from this mold using PDMS-based soft lithography. The curing agent were mixed 1:10 with PDMS monomers (Sylgard 184, Dow Corning) and degassed in a vacuum dessicator before heat curing in an oven. Curing time and temperature were adjusted to ensure minimal deviations of the microfluidic chip from desired dimensions. After curing, the microfluidic chip was demolded for use and 1 mm access holes for fluidic tubes were punched at the inlet and outlet using a flat cutting tip (Harris Uni-Core™).

### 3.2.3 Fabrication of micropatterned substrates

Protein patterning was achieved using a direct photolithographic method modified protocols reported in the literature [63]. 25 mm glass coverslips were first cleaned and made hydrophilic by immersing them for 15 mins in a piranha solution made by mixing concentrated sulphuric acid (Sigma) and hydrogen peroxide (Merck) at a ratio of 3:1. The cleaned coverslips were washed thoroughly using DI water and stored in methanol. When required for use, the coverslip were rinsed with DI water and dried before being further activated by oxygen plasma for 5 min. Subsequently, 0.1 mg/ml PLL-g-PEG (Surface Solutions) was incubated on the activated coverslips for 1 h before it was rinsed off. Next, designed micropatterns were transferred to the prepared coverslips by UV exposure through a 3” quartz photomask (SnFPC, IMRE). The photomask was first placed under UV light for 3 min before use to make it hydrophilic. A 2.5 µl drop of DI water was then placed between the mask and the functionalized coverslip, ensuring that no air bubbles were trapped. This was done to ensure close contact between the mask and the coverslip in the absence of a vacuum system. Photo-activation was carried out for 8 min with a 185 nm deep UV bulb (Heraeus GUH022-10T5VH). After photo-activation, the patterned coverslip was separated from the mask by immersing the mask in DI water. Patterned coverslips could be dried and stored on the lab bench for up to 3 days. When required for experiments, the patterned coverslip was immersed in water for 30 mins to rehydrate the PEG molecules. After rehydration, the coverslip was dried before incubating with 6 µg/ml of rhodamine-labelled fibronectin (Cytoskeleton, Inc.) in $NaHCO_3$ buffer for 1 hr, followed by incubation with 6µg/ml of native fibronectin (Sigma) for another 1 hr. Excess unbounded fibronectin was washed off in each step.

### 3.2.4 Cell culture and preparations

HeLa cells were cultured using high glucose Dulbecco’s modified Eagle’s medium (DMEM) (Gibco), supplemented with 10% (v/v) fetal bovine serum (Gibco) and 1% (v/v) penicillin/streptomycin (PAN). Cells were grown for three days to 90% confluence before passaging. Confluent cells were detached from the tissue culture flasks by incubation with 1X trypsin-EDTA (PAA) for 15 mins after which the trypsin was inactivated by adding an equal amount of medium. The suspension was then centrifuged at 1000 rpm for 5 min and the pellet was then re-suspended and re-seeded at 1:10 dilution. To obtain single cell suspension during experiments, the HeLa cells were detached from the culture flask and pipetted up and down a few times using a fine tip in complete DMEM medium. For better results, a 40 µm cell strainer (Becton Dickinson) could be used to remove undissociated cells. Cell density was adjusted to 80,000 cells/ml for random seeding experiments and 300,000 cells/ml for experiments involving the cell-positioning platform. When cell nuclei staining is required, , HeLa cells were rinsed twice with PBS to wash off the medium before incubation with 2 µM Hoescht33342 dye (Invitrogen) diluted in PBS for 20 min. After staining, the unbounded dye was removed by rinsing with complete medium. Live/dead staining of cells for assessment of cell viability was done using the LIVE/DEAD viability/cytotoxicity kit for mammalian cells (Invitrogen) using recommended protocol from the product.

### 3.2.5 Platform packaging and operation

To align sieve-like traps in the microfluidic chip to micropatterns at micro-meter precision, a self-made alignment fixture attached to a fluorescent upright microscope (BX61, Olympus) was used (see Fig. 3.2). The fixture basically consisted of a coverslip holder and a microfluidic chip holder that were made from glass slides. The fixture was simultaneously illuminated by both fluorescence and bright field to visualize both the rhodamine label on the micropattern and the features on the microfluidic chip. In practice, the micropatterns were in focus while the iris of the bright field microscope was occluded to increase the depth of focus in bright field. For alignment, the patterned coverslip was kept fixed by a drop of water while the chip holder was either rotated or translated. Rotational alignment was achieved by matching the alignment marks at opposite corners of the microfluidic chip with corresponding alignment marks on the micropatterns via a manual rotation the chip holder. Translation alignment was achieved by matching the traps to the micropatterns via the microscope stage. Once the traps and the micropatterns were aligned, the chip and the coverslip could be bonded by lowering the microscope stage. When the microscope stage was lowered, the whole alignment fixture was lowered as well. Eventually the chip holder, with its protruding ends, would get caught on the side blocks while the patterned coverslip and its holder continued to be lowered. This would result in contact between the coverslip and the chip for reversible bonding between them. After alignment, 0.02” fluidic tubes were connected to the access holes in the microfluidic chip through metal connects made from gauge 20 syringe needles to complete the packaging of the microfluidic platform.

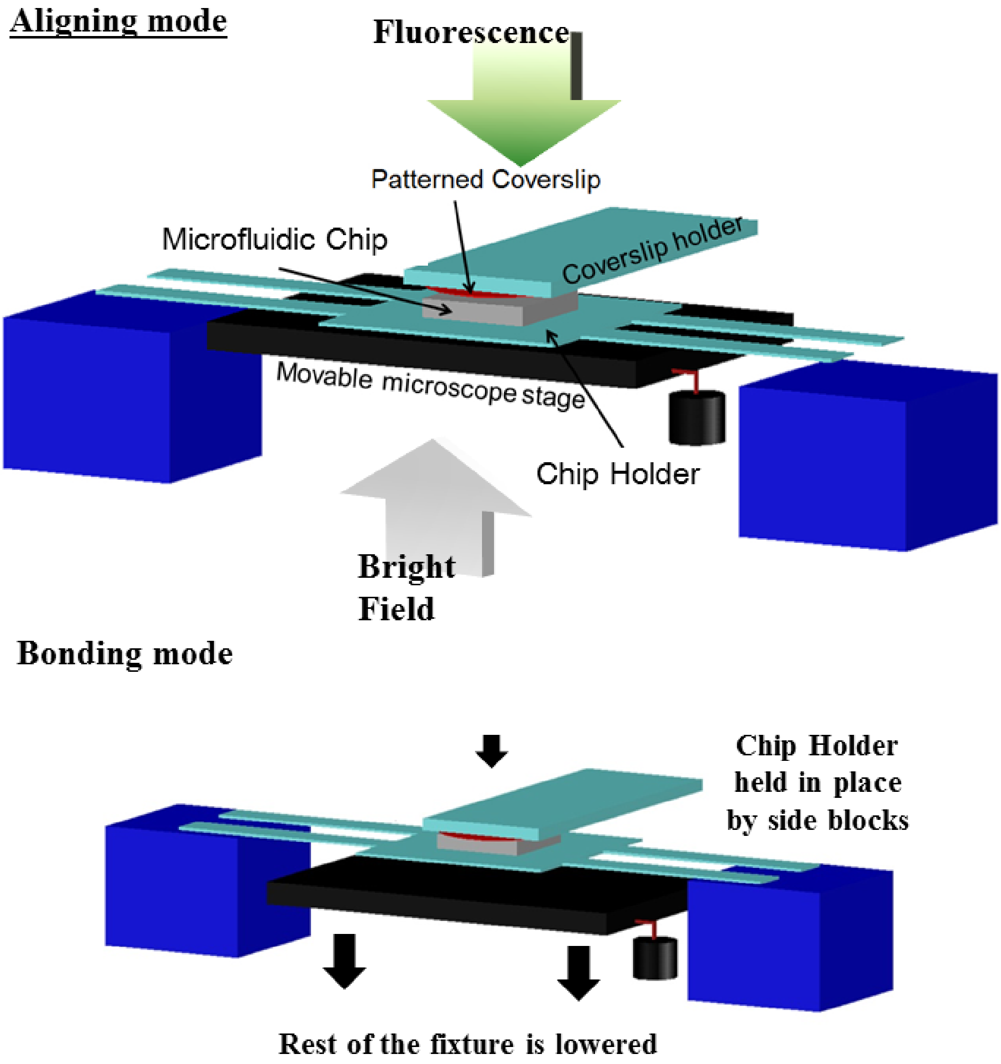

**Fig. 3.2.** Schematic diagrams showing alignment fixture in both aligning mode and bonding mode.

Experiments using the microfluidic platform were performed on a temperature control stage (Leica MATS) with temperature initially set at 23 °C and fluid flow through the microfluidic platform was powered by a syringe pump (Fusion 200, Chemyx Inc.). 0.2% (w/w) Pluronics F-127 (Sigma) in PBS was first flowed into the platform at a flow rate of 5 µl/min for 30 min to ensure that no air bubbles remained trapped in the microchannel. The flow was then stopped for 30 min to incubate the microchannel with pluronics for blocking against cell attachment. A flushing step was then carried out by flowing PBS at 5 µl/min for 1 hr to completely remove any pluronics residues from the platform. 60 µl of the prepared single cell suspension was then loaded into the device at a flow rate of 8 µl/min for cell trapping. A 30 min flushing step was then performed with $CO_2$-independent medium (Gibco) at 10 µl/min to remove untrapped cells and to replace the fluid in the platform with culture medium. After flushing, the flow rate was reduced to 0.5 µl/min and the temperature of the stage was adjusted to 37° C. Trapped cells were allowed to attach and spread on the micropattern for 90 min. After that, the coverslip was decoupled from the microfluidic channel and rinsed with PBS before further experiments or imaging. Cell trapping and attachment in the platform was imaged under an inverted microscope (Leica DM IRB) in DIC mode while rhodamine-labeled micropatterns and Hoechst-stained cell nuclei were imaged in epifluorescence mode. Images were captured using a colour CCD camera (DC500, Leica) at either 4X or 10X magnifications to cover a wide field of view.

## 3.3 Results and discussion

### 3.3.1 Random seeding

Using random seeding to populate micropatterns with cells is very straightforward but it is far from reliable, especially if a fixed number of cells are required to be consistently placed on a cluster of micropatterns in close proximity. For an isolated micropattern, the efficiency of finding a single cell on the pattern was reported to be about 40% [147]. When a few micropatterns are arranged in a cluster, it would clearly be much more difficult for all the micropatterns in the cluster to simultaneously satisfy this condition. To quantify this assertion in experiments, clusters of 800 μm$^2$ trapezium patterns micropatterns with two to six micropatterns in each cluster (see Fig.3.3.a) were populated with HeLa cells by random seeding and the efficiency of obtaining one cell per pattern was characterized. This efficiency was termed positioning efficiency after the efficiency

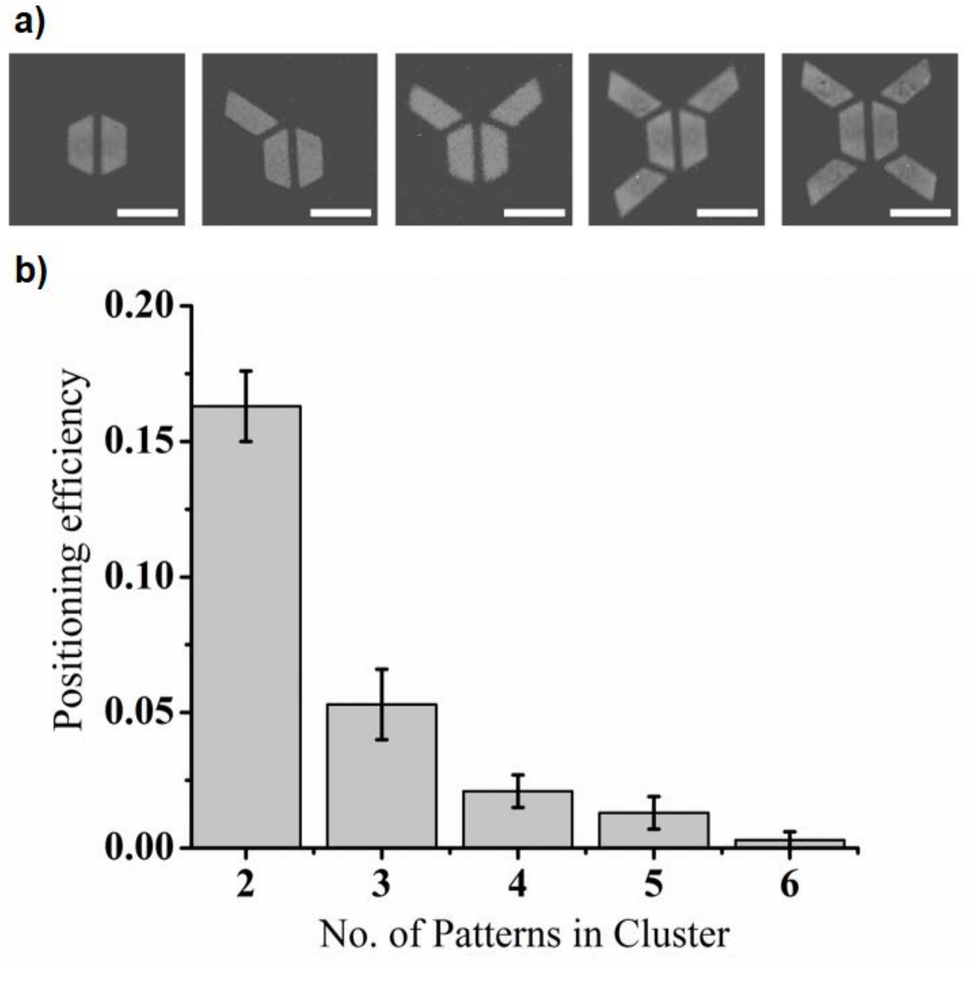

**Fig. 3.3.** Positioning efficiency in different types of micropattern clusters. a) Micropattern clusters with 2 to 6 micropatterns. b) Positioning efficiency for micropattern clusters with 2 to 6 micropatterns (n = 8). Scale bar depicts 50 μm. Error bars depict S.E. statistics.

of positioning cells at the right locality (i.e a single cell on top of each micropattern) and would be used throughout this chapter. To obtain the positioning efficiency of different types of micropattern cluster, the number of clusters with a single cell in each pattern was visually counted and this number was expressed as a fraction of the total number of clusters analyzed. This process was repeated over 8 independent random seeding experiments. The results showed that the positioning efficiency of random seeding decreases with increasing number of pattern in the cluster as shown in Fig.3.3.b. Positioning efficiency dropped significantly from 16.3% (S.E±1.3) in paired patterns to 0.3% (S.E±0.3) in 6 pattern clusters. Even though this result is only strictly true for trapezium micropatterns in this particular cluster configuration, it is highly probable that such a trend also exists for other micropattern designs and cluster configurations.

### 3.3.2 Flow modeling for optimal trap design

The presence of a hydrodynamic sieve-like trap in a laminar flow tends to create a region of high fluidic resistance around it as seen clearly in Fig. 3.4. Hence, cells flowing towards such traps are likely to be diverted away from them, resulting in a large proportion of empty traps [141]. To circumvent this problem, cell suspensions with a higher cell density could be used but this would instead cause an increase in the number of traps with 2 or more cells. For efficient single cell trapping, it would be ideal to identify trap design which would facilitate fluid flow through the trap. This was achieved through the use of 3D computational fluid dynamics (CFD) analysis. Cup-shaped traps reported in the literature were used as a reference and different designs of similar shaped traps were created (see Fig. 3.4). In the flow modeling, simulated particles of density 6.67 particles/$\mu m^2$ were allowed to flow near the trap and the paths of these particles were tracked (see black lines in Fig. 3.4). Fluid flow through the traps or flow efficiency was characterized by counting the number of particle tracks that pass through the trap. A trap design that allows more simulated particle tracks to pass through it would possibly indicate higher flow efficiency in experiments. The results from the flow modelling showed that the 3 block design shown in Fig. 3.4.e was the optimal design, allowing a

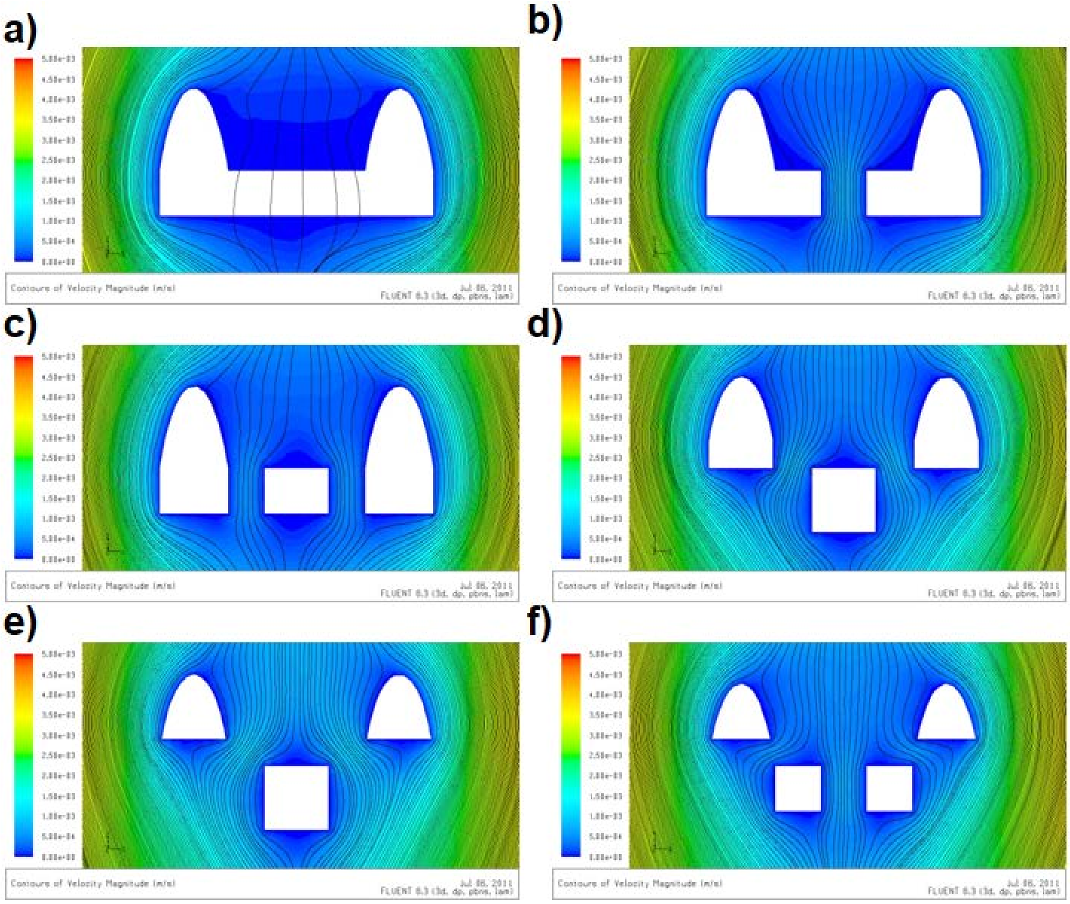

**Fig. 3.4.** CFD flow modeling for different trap designs. Particle tracks (black lines) of simulated particles of density 6.67 particles/μm overlaid with velocity magnitude contours (red: highest, blue: lowest) for different cup-shaped traps. Velocity magnitude contours gave an indication of the fluidic resistance in the trap vicinity. a) Reference design with no openings, 6 particle tracks through trap. b) 1 opening, 14 particle tracks. c) 2 openings, 12 particle tracks. d) No corners, 20 particle tracks. e) No corners with side openings, 30 particle tracks. f) 4-piece configuration, 20 particle tracks.

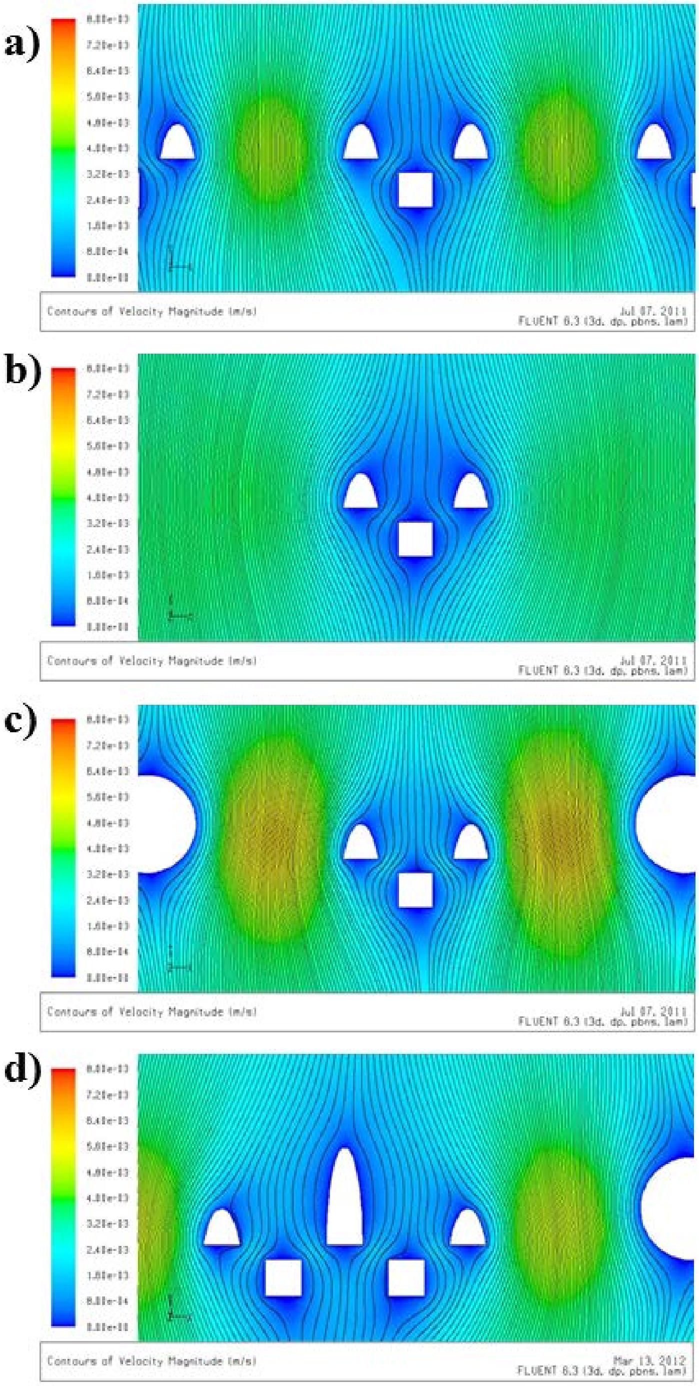

**Fig. 3.5.** Side pillars in cup-shaped traps and trident-shaped traps for trapping cells for effective trapping of single cells far apart and close together. Evaluation on cell trapping efficiency using flow modeling. Particle tracks (black lines) of simulated particles of density 1.33 particles/μm overlaid with velocity magnitude contours (red: highest, blue: lowest) for different cup-shaped traps. (a) Typical compact configuration of sieve-like traps: 8 particle tracks (b) Isolated trap: 5 particle tracks. (c) Isolated trap with side pillars: 9 particle tracks. (d) Trident-shaped traps: 9 particle tracks.

maximum number of 30 simulated particle tracks to pass through the trap. The reference cup-shaped trap design with no openings shown in Fig. 3.4.a only allowed 6 simulated particle tracks to pass through it. Velocity magnitude contours were overlaid with the particle tracks to give an indication of the fluidic resistance in the trap vicinity. As similar scale bars for the heat maps were used across the different designs, meaningful comparisons could be made by comparing the contour colours. For the optimized design, fluidic resistance around the trap was observed to be the lowest (See darker blue colour map in Fig. 5.4,) compared to the rest of the trap designs. This could account for the observed high flow efficiency as simulated particles were less likely to be diverted away.

Arrays of hydrodynamic sieve-like traps reported in the literature appear to be always arranged in a compact configuration [141,142]. To determine the impact of array configuration, the flow efficiency of an isolated trap was compared to a trap sandwiched by 2 adjacent neighbours as shown in Fig. 3.5.a and Fig 3.5b. In the flow modeling, simulated particles of density 1.33 particles/$\mu m^2$ were allowed to flow near the trap and the paths of these particles were tracked. Flow efficiency through an isolated trap was clearly lower with only 5 simulated particle tracks passing through it as compared to 8 for the trap with close neighbours. Hence, arranging sieve-like traps in a compact configuration might be crucial for high flow efficiency. However, when micropattern clusters are designed for biological studies, a reasonable amount of space between each cluster is required to avoid unwanted interactions between cells on different clusters. For example, the bow-tie patterns and micropattern ring clusters used in this thesis were spaced at least 200 µm away from their next nearest neighbours. Hence, closely packed sieve-like traps would not be compatible with these micropattern designs. To allow higher flexibility in array configurations, pillars could be designed at both sides of isolated traps to mimic closely packed neighbours (see Fig. 3.5c). These pillars would not trap cells but could possibly allowed traps to be designed far apart from each other without compromising flow efficiency. From the flow modelling results, the presence of these additional pillars indeed recovered the number of simulated particle tracks passing through the trap to 9 (see Fig. 3.5c).

On the other hand, cup-shaped traps had to be placed at least 30 µm apart to prevent clogging of cells between the traps. However, micropattern clusters are made up of patterns in close proximity where cells are needed to be positioned close to one another. For example, for the sieve-like traps to be compatible with bow-tie shaped patterns, cells are needed to be trapped side by side. To trap cells in close proximity, trident-shaped traps were designed. This trap design is a simple merger of two optimized cup-shaped design side by side. The centre portion of the trap was replaced with a half-elliptical structure which protrudes out from the rest of the trap. The design of this protruding structure aims to prevent multiple-cell trapping by allowing cells flowing towards an occupied trap to slide off to the sides. The flow modeling results (see Fig. 3.5d) showed that the flow efficiency of a trident-shaped trap was comparable to cup-shaped traps, similarly allowing 9 particle tracks to flow through each pocket of the trap. With the availability of the side pillars design and the trident-shaped trap design, cells could now be positioned either closed together or far apart from one another using sieve-like traps. This would facilitate the design of trap arrays that are compatible with a wide variety of cluster designs with micropatterns arranged in almost any configuration.

### 3.3.3 Gap between microfluidic traps and the substrate

The presence of a gap between the sieve-like traps and the substrate is one of the salient features of the cell-positioning platform. Firstly, it encourages single cell trapping by varying the fluidic resistance in the trap vicinity according to the occupancy of the traps.

By preventing contact between any parts of the microchannel with the micropattern, this gap also maintains pattern integrity when the microchannel is being peeled off. More importantly, it enables trapped cells to spread partially on the micropattern which facilitates stronger anchorage to the substrate. This prevents cells from being ripped off from the substrate by shear forces that may be generated from the removal of the microchannel.

To achieve such a gap, the height of the microfluidic traps should be different from that of the main channel. Fabricating features of different heights in PDMS replicas would require the corresponding features in the silicon mold to be etched to different depth. This is non-trivial and a 2 step fabrication process is typically required where each step etches selective regions in the wafer to one of the desired depth. Such a multi-step process is tedious and greatly increases the chance of having errors in the fabrication. In this work, a simple one-step method was used.  In deep silicon etching, anisotropic etching is achieved through the Bosch dry etch process. This process consists of repeated cycles of etching and deposition where a protective polymer (e.g. $C_4F_8$) was deposited on the surfaces of etched regions. When silicon is etched to a significant depth using the Bosch process, high aspect ratio features has been shown to be etched slower than features with low aspect ratios in a phenomenon named ‘RIE-lag’. In this work, the size of the sieve-like traps is much smaller compared to the walls of the main channel. Hence, aspect ratios of the corresponding features on the silicon would be higher and these features would be etched slower under the influence of RIE-lag. In this way, the height of the traps would be very different from that of the channel wall.

To visualize this feature size-dependent etch rate, the cross-section of a trident shaped trap was observed under SEM as shown in Fig. 3.6.a. The size of the central structure in the trident shaped trap was slightly larger than the rest of the trap and correspondingly, this central structure appeared to be higher. Even though the difference in sizes in this case was small, it was translated to an observable difference in feature height. With a much sizeable difference between the size of the traps and the channel wall, significant difference in height between them would be expected. This height difference between the sieve-like traps and the channel wall would manifest itself as the gap size between the traps and the substrate. An optimal gap size exists where the trapped cells have maximum amount of space to spread but are unable to squeeze through the trap during flow. Some degree of control on gap sizes would be very helpful as different cell types would likely have different optimal gap sizes. A 3-stage model had been proposed to account for the effects RIE-lag [148]. From this model, a change in the recipe for the Bosch process such as the etch time or deposition time could be used to influence the degree of RIE-lag. This change in RIE-lag would be translated to a corresponding change in gap size. In this work, some control of the gap size had been achieved by varying the etch time/cycle in the Bosch process as shown in Fig. 3.6. Gap sizes were calculated from measurements of the height of the traps and the channel walls in 3 separate PDMS microchips casted from the same wafer. Since, the channel walls were etched to slightly different heights with different recipes, gap sizes were normalized to the expected sizes when channel wall was 20 µm high. From the results, it was observed that gap sizes could be increased with a longer etch time / cycle.

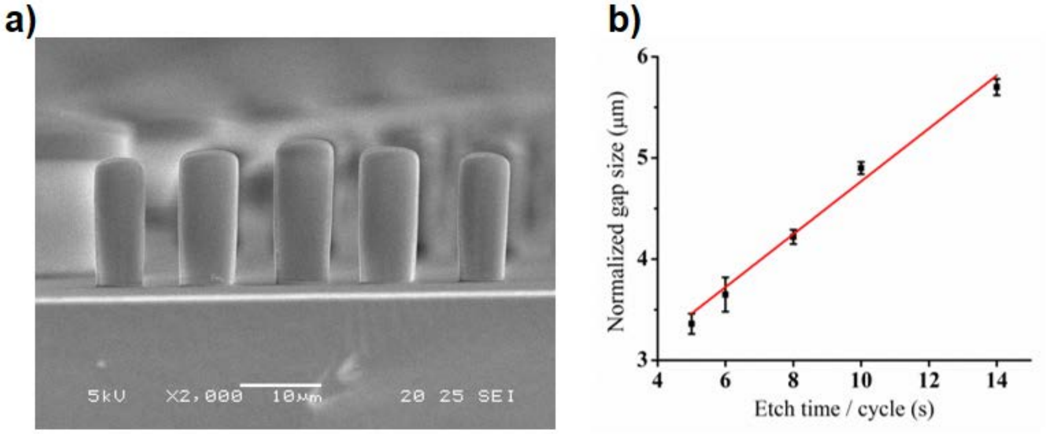

**Fig. 3.6.** RIE-lag from deep silicon etching. a) SEM image of PDMS replica of trident-shaped traps. Larger central structure appeared higher than the rest of the trap. (b) Normalized gap size as a function of etch time/cycle used in the process recipe (n =3). Gap sizes were measured from the 2nd and 4th pillar from left in (a). Gap size normalized to approximately what is expected for channel walls etched to 20 µm. Error bars depict S.E. statistics.

### 3.3.4 Towards high throughput alignment of microfluidic traps to micropatterns

Accurate alignment of the sieve-like traps to the micropattern is crucial for the cell-positioning platform to work. Inaccurate alignment might cause cells to be trapped above passivated regions in the micropatterned substrate which would result in non-adhesion between cells and substrate. The alignment method outlined in the material and methods section paired a single trap to its corresponding micropattern and relied on matching feature spacing in both arrays to propagate the alignment. The photolithographic method of protein patterning faithfully replicates designed feature spacing to micropatterned substrates but feature spacing between sieve-like traps had been observed to become smaller than designed ones. A small mismatch in feature spacing could result in a large misalignment between traps and micropatterns located far away from the point of alignment. Hence, this mismatch of feature spacing is highly undesirable in large arrays designed for high throughput cell positioning.

Heat curing of PDMS had been reported to induce shrinkage depending on the curing conditions [149]. To investigate the effect of curing temperature on the shrinkage of the microfluidic chip, chip samples were cured at different temperatures ranging from room temperature to 80 °C. As the rate of curing is highly dependent on temperature, different curing time was also needed. PDMS shrinkage in this study was measured by first aligning the alignment marks at one corner of the chip and then measuring the mismatch distance between the alignment mark at the opposite corner on the chip and the micropattern as shown in Fig. 3.7.a. This mismatch was expressed as a percentage of the distance between the alignment marks at both corners. 3 different PMDS microchips cured under the same conditions was compared with the same micropatterned coverslip in this manner. The results showed that PDMS shrinkage decreases from 1.18% when cured at 80 °C to 0.79% at 55 °C (See Fig. 3.7.b). When cured at room temperature for 3 days, the PDMS shrinkage was negligible. Though curing the microchips at room temperature might seem attractive, large scale cell bebbling was observed when these microchips were used for cell positioning. Room temperature curing possibly only resulted in partial curing of the PDMS and diffusion of monomers into the microchannel had been reported to be detrimental to cell survival [150]. To drive PDMS polymerization to completion, microchips cured at room temperature were followed by heat curing at 60 °C for 5 hr. Cell bebbling effects were eliminated but a PDMS shrinkage of 0.21% was also observed. This shrinkage was smaller than expected values if the PDMS was cured directly at 60 °C.

Taken together, these results suggested that the observed PDMS shrinkage could involve both effects due to heat-dependent phase changes (e.g. solvent evaporation and different expansion coefficients of silicon/PDMS) and polymerization effects. To eliminate mismatch between the traps and the micropatterns, larger spacing between sieve-like traps were designed to compensate for PDMS shrinkages. A 1% offset was used in practice and the spacing between traps and micropattern were matched by fine-tuning the curing temperature as shown in Fig. 3.7c. Using a 1% design offset and heat curing of the PDMS at 60 °C for 5 hr, trap arrays over a 3 mm by 2 mm region had been consistently aligned to micropattern arrays of the same size.

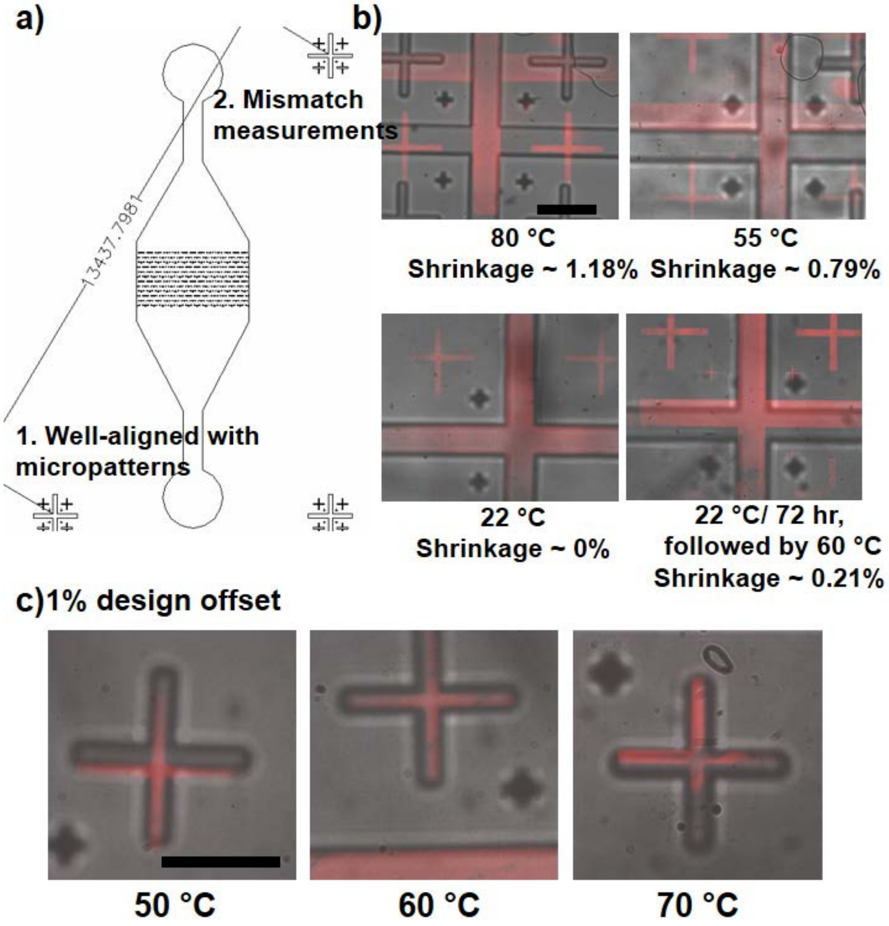

**Fig. 3.7.** Temperature dependent effects of heat curing on PDMS shrinkage. Microchip features in bright field and rhodamine-labeled protein micropattern under fluorescence. a) Characterization of PDMS shrinkage. Alignment marks on microchip well aligned with micropatterns at bottom left corner. Mismatch measured at the top right corner. Shrinkage expressed as a percentage of distance between alignment marks (n = 3). b) PDMS shrinkage cured at different temperatures. c) Fine tuning of curing temperature with a 1% offset in microchip design. Scale bars depict 200 μm. Error bars depict S.E. statistics.

### 3.3.5 Cell trapping statistics

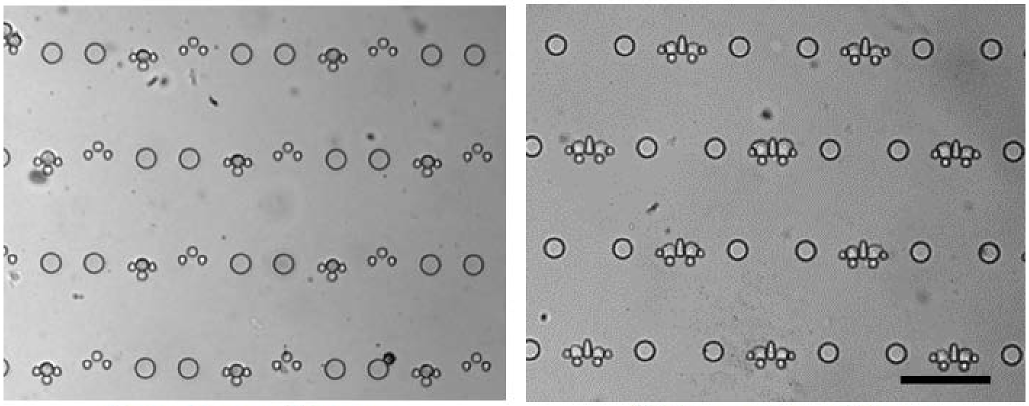
Cup-shaped Traps
for isolated cells

Trident-shaped Traps
for cell pairing

**Fig. 3.8.** Cell trapping in cup-shaped traps and trident-shaped traps. Scale bars depict 100 μm.

To evaluate the performance of the cell-positioning platform, the efficiency of single cell trapping using the designed traps was first characterized. Efficiency of trapping single HeLa cells was characterized for cup-shaped traps and the efficiency of pairing them side by side was calculated in trident-shaped traps (see Fig. 3.8). HeLa human cervical carcinoma cells attach easily and spread rapidly on fibronectin and were identified as an ideal cell line for testing. Optimized operation conditions were used for the characterizations where a cell suspension of density 300,000 cells/ml was loaded at a flow rate of 8 μl/min. Cell suspensions of lower cell density or loaded at high flow rates were observed to preferentially flow along the sides of the microchannel, resulting in many empty traps at the channel centre. Higher cell density or lower flow rates tend to result in multiple-cell trapping leading to a clogging of traps and eventually the microchannel. Cell trapping efficiency was measured after a flushing step by visually counting the number of single cells in cup-shaped traps or the number of pair cells in trident-shaped traps. Trapping efficiency was then expressed as a percentage of the total number of traps in the array. Collapsed traps or traps blocked by impurities were not used in the calculations. This process was repeated 3 times in different microchips. The results showed a single cell trapping efficiency of 86.2% (S.E.±2.8) in cup-shaped traps and a pairing efficiency of 71.1% (S.E.±4.9) in trident-shaped traps. These trapping efficiencies are comparable to some of the more efficient trapping methods reported in literature as shown in Table 3.1.

**Table 3.1.** Comparisons of single cell trapping and cell pairing efficiency in designed sieve-like traps with reported methods.

| **Trapping Method** | **Trapping Efficiency** | | **References** |
|---|---|---|---|
| | **Isolated Cells** | **Paired Cells** | |
| Micropatterns only | ~40% | ~30%* | Yan C et. al., *Biomaterials*, 2011 |
| Microwells | 84.5% - 92.2%** | — | Rettig JR et. al., *Anal. Chem.*, 2005 |
| Microwells | ~50% | ~35% | Tang J et. al., *Biomaterials*, 2009 |
| Positive Dielectrophoresis | — | 70% | Gray DS et. al., *Biosens. Bioelect.*, 2004 |
| Hydrodynamic Serpentine Channel with Side Conduits | 85.0% | 70.0% | Frimat JP et. al. , *Lab Chip*, 2011 |
| Hydrodynamic sieve-like trap | ~55% | — | Di Carlo D et. al., *Anal. Chem.*, 2006 |
| Hydrodynamic sieve-like trap | — | ~70% | Skelley AM et. al., *Nat. Methods*, 2009 |
| **Hydrodynamic sieve-like trap** | **86.2%** | **71.1%** | **This work** |

* Represents a large pattern to accommodate 2 cells, not to be confused with 2 smaller patterns designed for 1 cell each

* *Efficiency varies depending on cell line used

### 3.3.6 Pair-wise cell positioning

Having established that the designed sieve-like traps could trap cells at good efficiencies, trident-shaped traps were coupled to bow-tie patterns to evaluate the overall performance of the cell positioning platform. These bow-tie shaped patterns were similar to the ones used in Chapter 4 where a single cell is required to be positioned on each bow-tie region.

The use of trident-shaped trap that could trap single cells side by side would be ideal for this purpose. A proof-of-concept demonstration was shown in Fig. 3.9.a. Trapped cells was clearly observed to spread on the micropattern underneath the microfluidic trap. This showed that the presence of a gap between the trap and the substrate indeed allowed cells to spread on micropatterns and could be important for the platform to work. After the microchannel was decoupled from the coverslip, the positioning efficiency of the platform was characterized. Characterization of positioning efficiency was performed on platforms with an optimized gap size of 6 µm between the trap and the substrate. When the gap size was less than 5 µm, the cells remained rounded on the micropattern and most of them were detached during the removal of the microchannel. Similar to what was done for random seeding, the number of bow-tie patterns with a single cell in each bow-tie region was visually counted and this number was expressed as a fraction of the total number of patterns analysed. This process was repeated 3 times. The results showed that a positioning efficiency of 67.0% (S.E±3.0) could be achieved for array of 150 bow tie patterns in staggered configuration. This was a slight decrease from the 71.1% trapping efficiency recorded for trident shaped traps which suggested that not all the trapped cells eventually remained on the micropattern (see Fig. 3.9.b). The trapping of non-viable cells or cell attachment to PDMS traps could be some plausible explanations. Shear forces from the removal for the microchannel could also have pulled off some of the cells that were not well-adhered. However, the numbers showed that more than 95% of the trapped cells could be retained. Random seeding experiments were also performed on bow-tie patterns in an identical array (see Fig. 3.9.c). The results showed that a positioning efficiency of only 17.1% (S.E±2.1) was obtained by 3 independent random seeding experiments. This translates to a 4-fold improvement in positioning efficiency through the use of the cell positioning platform (see Fig. 3.9.d).

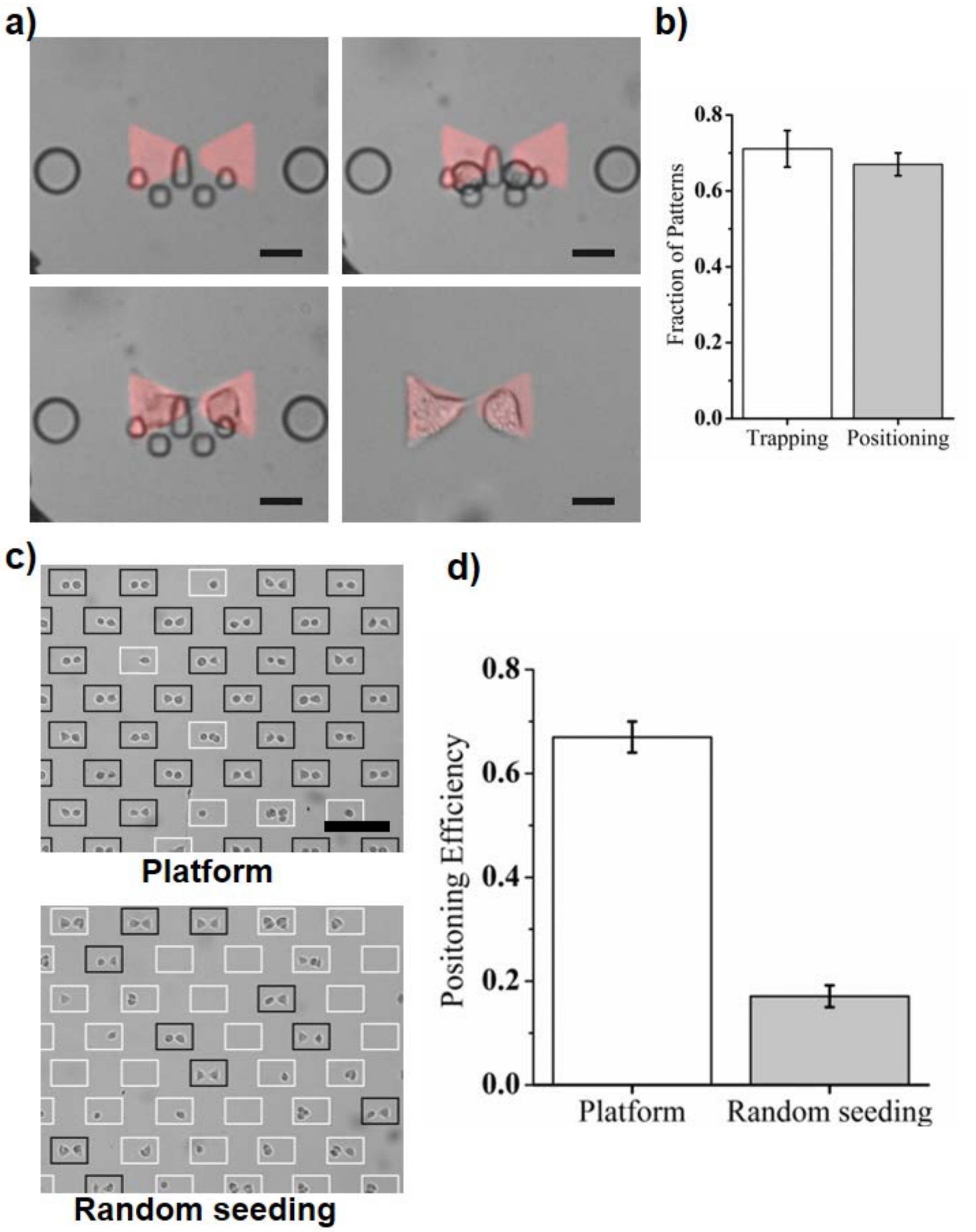

**Fig. 3.9.** Cell positioning on bow-tie shaped micropatterns. a) Proof of concept demonstration of cell positioning. Scale bar depict 20 μm. b) Comparing cell trapping efficiency of trident shaped traps and positioning efficiency of platform (n = 3). Differences indicate not all the trapped cells eventually remained on the micropattern after removal of microchannel. c) Representative regions showing positioning using cell positioning platform (top) and random seeding (bottom). Black box indicates pattern with well positioned cell pair, white box for other patterns. Scale bar depicts 200 μm. d) Comparing positioning efficiency of platform and random seeding. 4-fold improvement achieved using cell positing platform (n = 3). Error bars depict S.E. statistics.

As positioned cells were exposed to a variety of mechanical forces during the operation of the platform, there was a need to confirm the viability of these cells. HeLa cells were either positioned using the platform or randomly seeded on fibronectin-coated coverslips without patterns. Characterization of cell viability was based on both live/dead staining and the morphology and proliferation rate of adhered cells over a 4-day period. For live/dead staining, cell viability kit was used which stained live cells green and dead cells red. In 3 independent experiments, 94.3 % (S.E±0.7) of the cells were found to be viable when positioned using the platform. Using similar methods, the viability of cells directly seeded on the fibronectin-coated coverslips was found to be 97.6% (S.E±0.8). This drop of 3.3% in cell viability could be considered as acceptable. The morphology and proliferation rate of adhered cells were assessed using phase-contrast images of the same representative region taken on the 1st, 2nd and 4th day after cell attachment. The results showed that cell morphology were comparable for both cells positioned by the platform and randomly seeded cells (see Fig. 3.10). The number of cells in the representative region was visually counted immediately after attachment and again after 4 days. A comparable proliferation rate was also obtained where the cells increased by about 7.5-fold in both cases. Taken together, these results suggest that cell positioning using the platform did not affect the viability of the positioned cells.

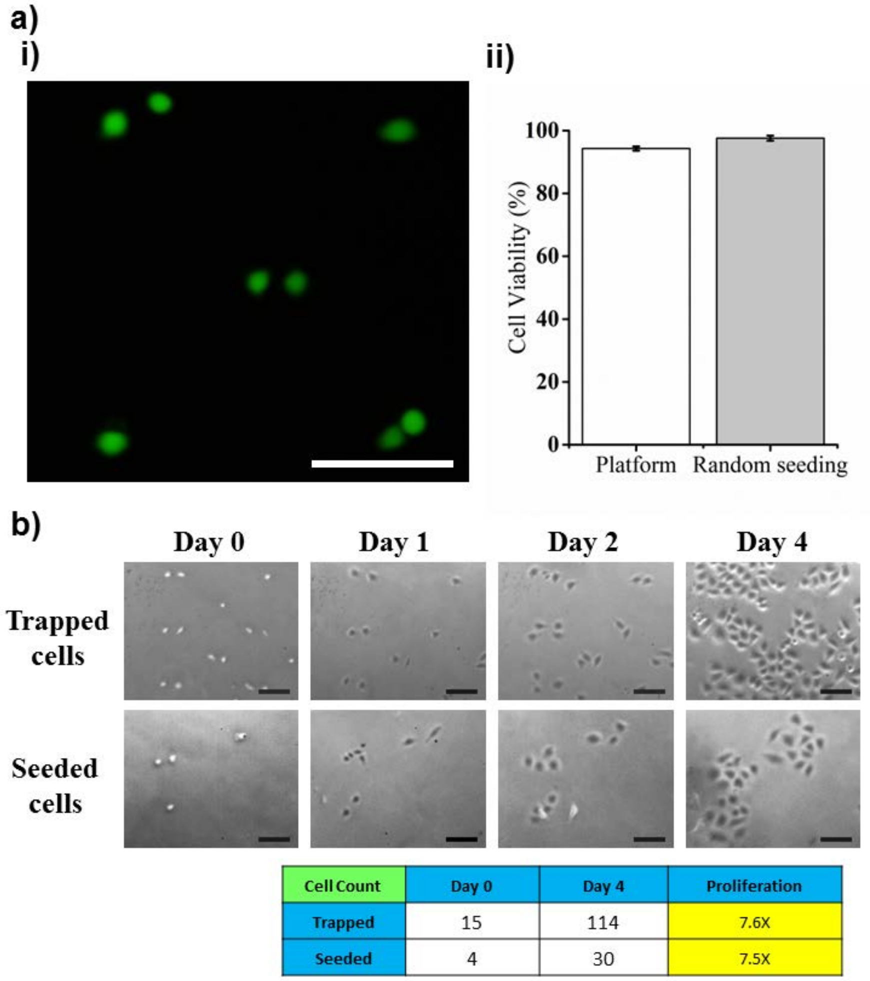

| Cell Count | Day 0 | Day 4 | Proliferation |
|---|---|---|---|
| Trapped | 15 | 114 | 7.6X |
| Seeded | 4 | 30 | 7.5X |

**Fig. 3.10.** Assessment of cell viability. (a) Live/dead staining on cells. (i) Cells positioned using the platform. Green: viable cells, red: dead cells. (ii) Comparison of viability staining between cells randomly seeded (n = 3) on fibronectin coated coverslips and cells positioned using platform (n = 3). (b) Cell morphology and proliferation rates in a representative region. Scale bars depicts 100 μm. Error bars depict S.E. statistics

### 3.3.7 Cell positioning on a 6-pattern ring

To assess the performance of the cell positioning platform in larger micropattern clusters containing more patterns, cell positioning was also demonstrated on micropatterns arranged in a ring configuration. These micropattern rings were similar to the ones described in Chapter 5 but in this case a hexagonal ring comprising six 800μm$^2$ trapezium-shaped patterns was used. As a spacing of 30 μm was required between cell traps to prevent clogging between traps, limited space was available within the micropattern ring for trap placement. In this case, the use of trident-shaped traps for the trapping of cells in pairs would be useful for optimizing the use of available space. Due to the geometry of the ring, cup-shaped traps were needed to trap two of the required cells individually. In Fig. 3.11.a, a combination of trident-shaped and cup-shaped traps was shown to position 6 single cells nicely on top of the micropattern ring.

Positioning efficiency using the platform was also characterized for 6-pattern rings following similar procedures employed for bow-tie patterns. Fig. 3.11.b showed adhered cells in a ring configuration after the microchannel was removed. A good number of rings were shown to contain exactly 6 cells which were well-distributed within the rings. Fig. 3.11.c. confirmed that these adhered cells were indeed properly positioned on the micropatterns with one cell residing on each pattern. Overall, 16.7% (S.E±0.7) of the patterns analysed was found to contain properly positioned cells in 3 independent experiments. When this result was compared to the 0.4% (S.E±0.2) positioning efficiency obtained using random seeding (n = 3), a highly significant 40-fold improvement was achieved through the use of the cell positioning platform (see Fig. 3.11.d). Taken together with the results for bow-tie patterns, it was clear that the advantages of using the cell positioning platform were amplified in micropattern clusters containing a larger number of micropatterns.

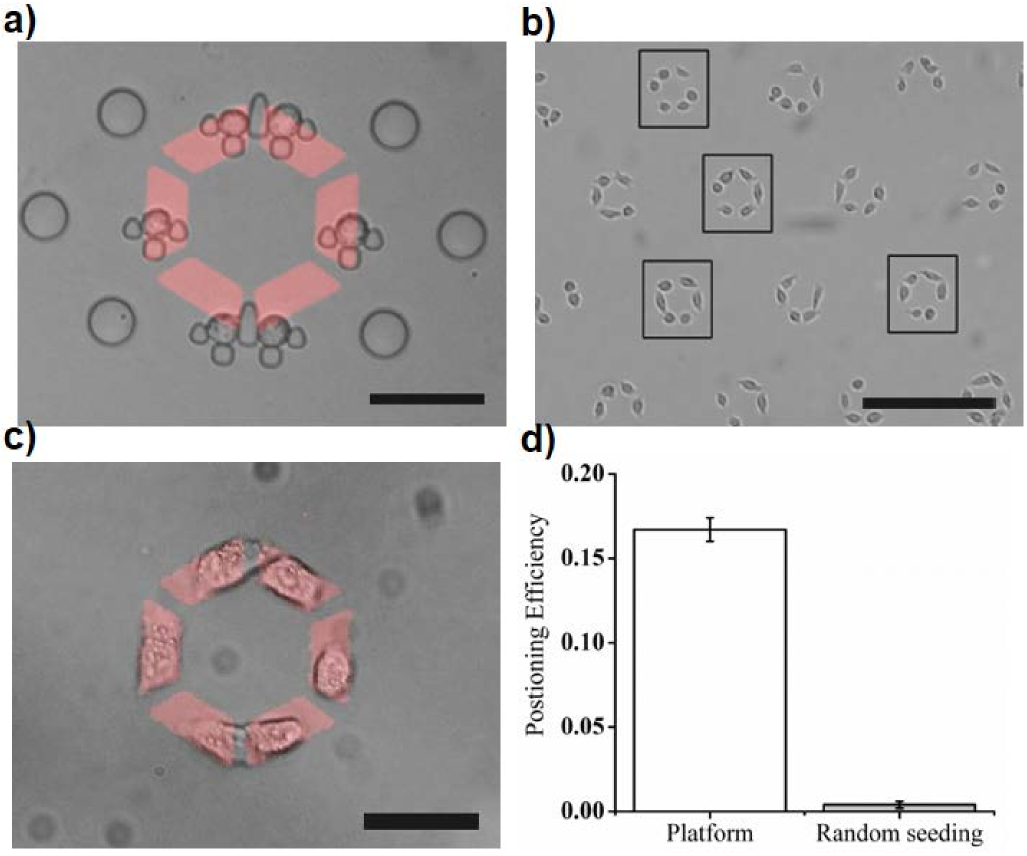

**Fig. 3.11.** Cell positioning on micropattern rings. a) Combination of trident-shaped traps and cup-shaped traps for cell trapping on micropattern ring. Scale bar depict 50 μm. b) Phase image showing adhered cells positioned by platform on micropattern rings. Scale bar depict 300 μm c) Adhered cells were properly positioned on micropatterns. Scale bar depicts 50 μm. d) Comparing positioning efficiency of platform and random seeding (n = 3). 40-fold improvement achieved using cell positing platform. Error bars depict S.E. statistics.

### 3.3.8 Platform variants: Heterotypic cell pairing

The use of sieve-like traps in the cell-positioning platform allowed trap design to be modified easily without significant disruptions to platform operation. In this chapter, cell positioning using similar principles had been demonstrated with traps of two very different designs serving distinct purposes. Also, integration of these traps could be accomplished with ease as demonstrated by the combination both trident-shaped traps and cup-shaped traps for trapping cells on micropattern rings. This flexibility in trap design and the seamless integration of different trap types could be attractive for the design of platform variants performing their own unique functions. Here, a platform variant capable of pairing single cells from two different cell populations is introduced. Some cell types, in particularly hepatocytes and endothelial cells, had been reported to exhibit very different functional and morphological behaviour when co-cultured with other cells such as fibroblasts and carcinoma cell lines *in vitro* [151]. This observed behaviour of co-cultured cells is thought to be closer to the *in vivo* situations. Although random co-culturing of different cell types in confluent monolayers is not new, there is a growing interest to develop methods to engineer controllable heterotypic cultures [152], in particularly at the single cell level [144,153,154]. These methods of single-cell manipulation were designed and developed specifically for heterotypic cell pairing but a simple modification in the layout of cup-shaped traps could also allow the platform variant to perform the same function.

In this platform variant, cup-shaped traps were designed in pairs with one trap rotated 180° compared to its neighbour as shown in Fig. 3.12. Cells flowing through a pair of these traps can only be effectively captured by the trap that is orientated in correct direction. For a proof-of-concept demonstration of the platform variant, the platform was set up as before using microchips with the new design. Pairs of cup-shaped traps were coupled to bow-tie shaped patterns with one trap in each bow-tie region. Unstained HeLa cells (1st cell population) were first flowed into the channel from the inlet and single cells were only captured in one of the paired traps as shown in Fig. 3.12.a. The trapped cells were then allowed to adhere and spread on the micropattern. Next, Hoechst-stained HeLa cells (2nd cell population) were injected into the channel from the outlet (see Fig. 3.12.b). Since the flow was reversed, stained cells could now be captured in the other trap as shown in Fig. 3.12.c. The flow rate used for cell trapping was relatively low and insufficient to detach unstained cells that had already spread on the micropattern. As before, the microchannel was removed after the stained cells had adhered, leaving a heterotypic pair of stained and unstained cells positioned side by side as confirmed by fluorescence microscopy (see Fig. 3.12.d).

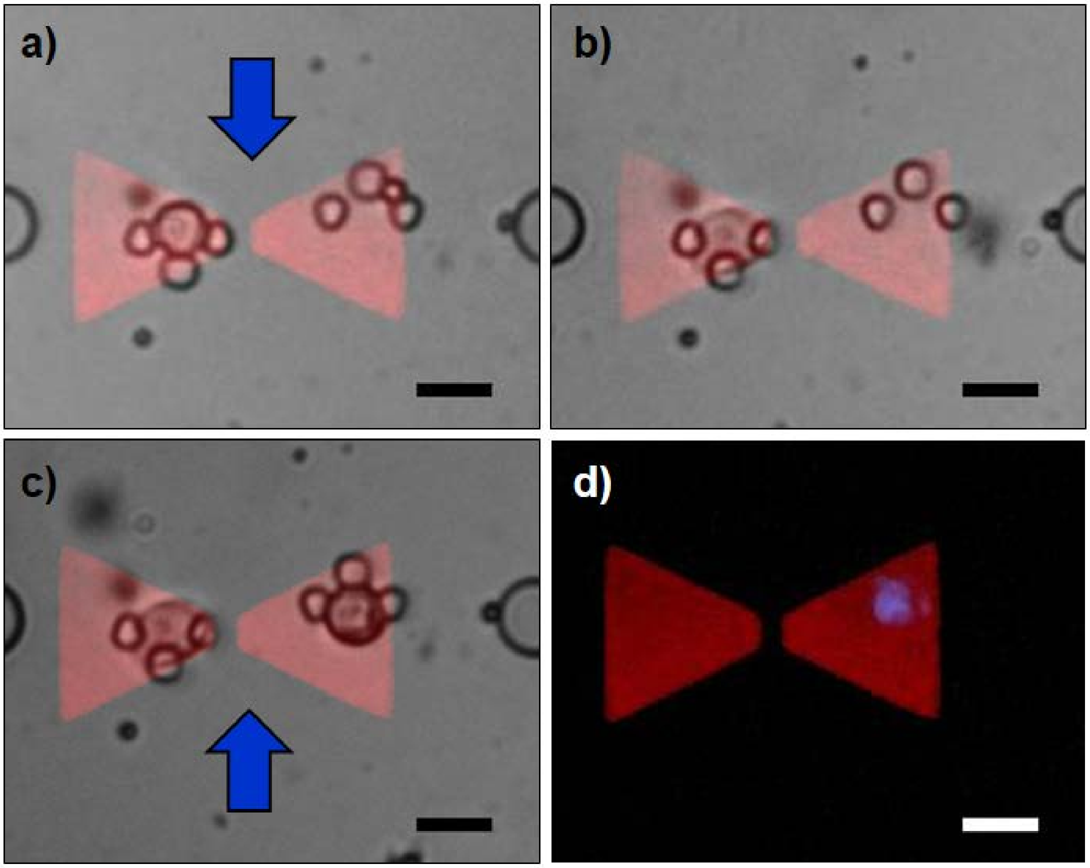

**Fig. 3.12.** Heterotypic cell pairing. Paired cup-shaped traps with one of them rotated 180° compared to its neighbor a) Unstained HeLa cells injected from the inlet. Cells were captured in only traps orientated in the right direction. b) Trapped cells allowed to spread on micropattern. c) Hoechst-stained HeLa cells injected from the outlet. Cells could now be captured in the other trap. d) Pairing of stained and unstained HeLa cells confirmed by fluorescence microscopy. Scale bars depict 20 μm.

## 3.4 Conclusions

In this chapter, a cell positioning platform to position single cells controllably on fibronectin micropatterns had been introduced. The microfluidic chip at the heart of this platform could be easily fabricated by soft lithography from a silicon mold which in turn was produced by a straightforward one-step microfabrication process. The microfluidic chip was aligned to the micropatterned substrate using a homemade alignment device and could also be easily detached after positioning for imaging and subsequent experiments. By designing both trident-shaped traps and pillars at the side of the sieve-like traps, single cells could be trapped close to and far apart as desired, making the traps compatible to a wide range of micropattern configurations. Cell viability was also found to be largely preserved after going through the positioning process in the platform.

A 4 fold improvement in positioning efficiency was observed on paired micropatterns when using the platform as compared to random seeding and a highly significant 40-fold improvement was recorded for 6-pattern rings. Heterotypic cell pairing had also been demonstrated. Hence, this cell-positioning platform could potentially be an attractive technology to allow highly efficient use of micropattern clusters to study multi-cellular dynamics or the design of sophisticated micropattern clusters containing different populations of cells in a well-defined configuration.

# Chapter 4

# Motility of Geometrically Constrained Cell Clusters

## 4.1 Introduction

Cell motility has been observed and studied in various possible modes and cellular scale, each exhibiting unique forms and features that are very different from one another. Cell migration is the most commonly studied form of cell motility for adherent mammalian cells where polarized cells are thought to move by a threadmilling mechanism involving membrane extensions at the leading edge and retraction of the cell body at the rear. Besides actual displacement of the cells, cells which are confined by geometrical constraints have also been observed to move among one another in the epithelial cell sheet without disrupting the tissue integrity. In some cases, the movement of the epithelial cells is observed to resemble persistent rotation in a particular direction. This was more commonly observed *in vitro* on substrates with micropatterned proteins, for example in cell pairs confined on micropatterns [126, 155]. In larger circular patterns containing hundreds to thousands of cells, the rotational persistence appeared to depend on cell density, pattern size and epithelial characteristics of the cells [122]. These rotational movements were also observed in 3D cell clusters embedded in gels where the rotational motion was thought to be important for the assembly of the ECM matrix [156], the establishment of epithelial tissue polarity [157] and the organization of spherical tissue architecture [158]. *In vivo*, persistent rotational motion is less common, but unique cases have been reported particularly during *Drosophila* morphogenesis for example during follicle epithelium elongation in oogenesis [159], at the onset of border cell migration in the ovary [160] and during ommatidal cluster formation in the *Drosophila* eye [161].

Apart from undergoing a persistent rotation, constrained epithelial cell clusters also tend to rearrange themselves to remodel tissue shapes during morphogenesis. In this case, cells are constrained by strong inter-cellular adhesion deep in the tissue layer and cell rearrangement can generally occur without disruption of the integrity of this tissue layer. A typical example of cell rearrangement is observed in convergent-extension where the cells move between one another and exchange neighbors in a process termed cell intercalation. This process is conserved across several morphogenic systems ranging from the antero-posterior elongation of the mesoderm during *Xenopus* gastrulation [162] to the tube extension of the respiratory system during *D. melanogaster* morphogenesis [163]. A second prominent example is invagination where a localized constriction of the apical surface of cells within the epithelium is perpetuated into a resultant buckling in that section of the epithelium such as that observed during the initiation of *Drosophila* tubulogenesis [164]. In comparison, the rotation of a pair of cells confined on micropattern could be seen as a scaled down version of these tissue-level rearrangements where the only possible form of rearrangement is for the cell pair to exchange position with each other.

Cell rearrangement has been found to be dependent on highly polarized tissues generated by the timely expression of process-specific genes at precise locations in the tissue. However, exactly how this molecular patterning over time and space drives the movement of cells is currently still under investigation. In cell intercalation, cell-cell junctions of a selected region of hexagonal cells must first be shortened to form multi-cellular rosettes before the junctions are lengthened again in the transverse direction to reform the hexagonal cell shape. Based on results currently available, this remodeling of the cell junction is thought to be dependent on the interplay between the expression of cell-cell adhesion molecules which extends the cell junction and cortical tension which shortens it [165].

Minimal model experiments involving micropatterned cell pairs which represent cell clusters formed in the simplest way possible have been reported. In an early study investigating how persistent rotation of a cell pair is highly cell-type specific, the authors concluded that both the persistence time of unpatterned cells in random walk and the quality of cell-cell contact are important parameters for persistent rotational motion [155]. Pair-wise rotation of cells also appears to be dependent on glucose concentration in the culture medium [166]. Under low glucose conditions, cell rotation appears to be slower probably due to a lack of ATP to power actin polymerization. More recently, the presence of ECM at the cell-cell junction was found to encourage cell motility [131]. The authors observed that the cell-cell junction of a cell pair preferentially orientated itself to stabilize at regions devoid of ECM. By using traction force microscopy, it was also observed that when the cell-cell junction resides on a region without ECM, less tension was experienced by the cell pair along the direction perpendicular to the cell junction. This reduction in perpendicularly-oriented tension would be correspondingly balanced by a decrease in cell-cell forces that might account for the spatially stabilized cell pair.

In the case of cells migrating freely in isolation or as a collective sheet, the physical parameters governing their migration modes had been substantially studied [105-109, 119-123]. However, for a constrained cell cluster, more work needs to be done to understand the rules that physically govern cell motility. In this chapter, bow-tie micropatterns were designed to unravel how individual cell area, cell-cell contact length as well as the cell shape can govern the motility of these cell pairs. The physical principles obtained using these two cell experiments would then be further verified in 3-cell clusters residing on circular patterns.

EpH4 murine mammary gland epithelial cells were chosen to be used for the studies in both chapter 4 and 5 because they are known to form tight cell-cell contact which could even be highly visible in bright field without fluorescence staining. This cellular property would allow multi-cellular dynamics to be observed conveniently in experiments without too many of the cells breaking their contacts and behaving as isolated cells. There are also some evidences to suggest that epithelial resealing by actomyosin-based contraction appears to be restricted to only cell-types with strong cell-cell contact [38].

## 4.2 Materials and Methods

### 4.2.1 Cell culture and preparation

Micropatterning was performed using the photolithographic method as described in Chapter 3. For the protein incubation step, the pattern coverslip was incubated with 20μg/ml of fibronectin (Sigma) in 0.1M NaHCO instead. EpH4 cells were cultured and prepared in the same way as HeLa cells as described in Chapter 3. 2 ml of EpH4 cell suspension with a cell density of 100,000 cells/ml were added to the patterned coverslip in a 35 mm petri dish and incubated in standard cell culture conditions for 30 min. After the incubation time had elapsed, the excess cells were rinsed off using serum-free DMEM medium supplemented with only 1% (v/v) penicillin/streptomycin (PAN) and allowed to spread in standard culture conditions for 12 hrs. The use of serum-free medium ensures that the cells can spread fully on the micropattern and adopt the desired shape. For better cell spreading, the patterned cells could be treated with 20 μM blebbistatin for 1 hr before allowing to spread. Both serum-free medium and blebbistatin reduces cell contractility, promoting cell spreading [167] and may even prevent protein from being pulled off the substrate. After the cells had fully spread on the micropattern, the serum-free medium must be replaced by complete medium before further experimental steps. This was done by aspirating the serum-free medium in the petri dish on one side while simultaneously adding fresh complete medium on the other side of the dish. This was done to prevent the coverslip from drying due to the hydrophobic PEG surface. To stain the cell nuclei, similar protocol was followed as described in chapter 3. For drug treatment, drug powder was dissolved in DMSO and diluted to the required dosage in complete medium. A dose of 1 µM or 2 µM was used for Y27632 (Sigma) and ML7 (Sigma) treatment while a dose of 1 nM was used for Calyculin A (Sigma).

### 4.2.2 Quantification of focal adhesion density

For immunofluorescence staining, coverslips with fully spread cell pairs on the micropatterns were first washed twice with PBS containing $Ca^{2+}$ and $Mg^{2+}$ to remove any serum residues. The cells were then detergent extracted using 0.01% Triton-X-100 in cytoskeleton buffer (10 mM MES, 138mM KCl, 3 mM MgCl, 2mM EGTA) for 1 min and immediately fixed using 3% paraformaldehyde (Sigma) for 10 min. The coverslips were then washed twice with PBS for 5 min. Following which, cells were permeabilized using 0.3% Triton-X-100 for 10 min and then washed twice again with PBS for 5 min. The cell nuclei and actin filaments were stained with 2 µM Hoescht33342 dye (Invitrogen) and Alexa Fluor 594-tagged phalloidin (Invitrogen) (diluted 1:800) in blocking buffer (PBS with 1% BSA and 0.2% Tween-20) for 60 min. Next, the coverslips were incubated overnight at 4 °C with a primary rabbit antibody for phoshorylated paxillin (Abcam) diluted 1:200 in the blocking buffer. After that, the primary antibody was thoroughly washed off using PBS containing 0.2% Tween-20 before the coverslip was incubated for 60 min with Alexa Fluor 488-tagged anti-rabbit polyclonal antibody (Invitrogen) diluted 1:500 in PBS. The secondary antibody was again thoroughly rinsed off before the coverslips were mounted and dried overnight at room temperature.

For the quantification of focal adhesion density, epifluorescence images of the cell pairs were taken at 60X magnification. The images were then processed using the ImageJ software. Background fluorescence was first removed using the ‘Subtract Background’ function before the image was binarized with the immunofluorescence stains appearing white. The total areas of the immunofluorescence stains in each cell pair were measured using the ‘Analyze Particles’ function with a minimum particle size of 0.25 $\mu m^2$.

### 4.2.3 Time-lapse imaging

Time-lapse imaging of live cells on micropatterns was taken over a 6 hr period at 10 mins time intervals using the BioStation IM-Q system (Nikon). The cells were maintained under standard culture conditions during imaging. Images were taken under both bright field illumination and 340-380 nm (UV range) excitations using the in-built cooled CCD camera at either 10X or 20X magnifications. Exposure time was kept low at 20 s for illuminated light and 8 s for the UV light to minimize photo damage to the cells. A 5mm by 5 mm imaging area can be probed automatically by the system using a motorized stage. Micropattern arrays were designed to be compatible with this imaging window to allow up to 1,000 patterns to be imaged in one experiment. For drug treatment studies, the cells were exposed to the drugs for 30 mins prior to commencement of imaging and also throughout the whole imaging period of 6 hrs without any drug washout.

### 4.2.4 Measuring the orientation of the nucleus-nucleus axis for cell pairs

Following the paper investigating the effect of ECM at the cell-cell junction on cell motility [131], the nucleus-nucleus axis, θ was also used to measure the relative position of the cell pair. A flow chart showing the steps to measure θ from raw images is shown in Fig. 4.1. From raw images obtained from the BioStation IM-Q, patterns that did not fulfill any of the following three criteria at any time point were immediately discarded: (1)

patterns must contain exactly two cells, (2) cells must spread fully on the patterns and (3) cell-cell contact between the two cells must be maintained. The third criterion was judged visually based on the cell-cell contact itself which was highly visible under phase contrast for EpH4 cells and also from the movement of the cell pair which should appear to be collective. For the remaining patterns, the corresponding time lapse images showing the nuclei of the cell pair under UV excitation were also obtained. The nucleus-nucleus axis was denoted as the line connecting the center of the two cell nuclei. The orientation of this axis, $\theta$ was calculated from position coordinates of the cell nuclei using simple trigonometry. In this chapter, $\theta$ was taken to be the anti-clockwise angle (to the nearest 1°) from the horizontal in the range $-90° < \theta < 90°$. For high throughput quantification of $\theta$ over the entire imaging period, the position coordinates of the cell nuclei was located automatically using the CellProfiler software [168]. The coordinates of the nuclei center are then exported to Excel (Microsoft) for the calculation of $\theta$ and other downstream calculations. When calculating $\theta$ from position coordinates of the cell nuclei, the result must be corrected for the overall tilt of the pattern array from the horizontal. This tilt in the pattern array could be measured accurately from wide field images that are obtained by stitching all the images obtained from the whole 5 mm X 5 mm imaging area. This parameter $\theta$ was used to represent the relative orientation of one cell with respect to its neighbor and had been used recently to study the effect of ECM on the spatial stability of cell junctions [131]. For example when $\theta = 0°$, it meant that the two cells are orientated side by side. When a graph of $\theta$ against time was plotted, a jump in the graph could be observed when the cell pair switches position on the bow-tie pattern as seen in Fig. 4.2.b and Fig. 4.2.c. This is due the convention of measuring $\theta$ in the limits of $-90° < \theta < 90°$.

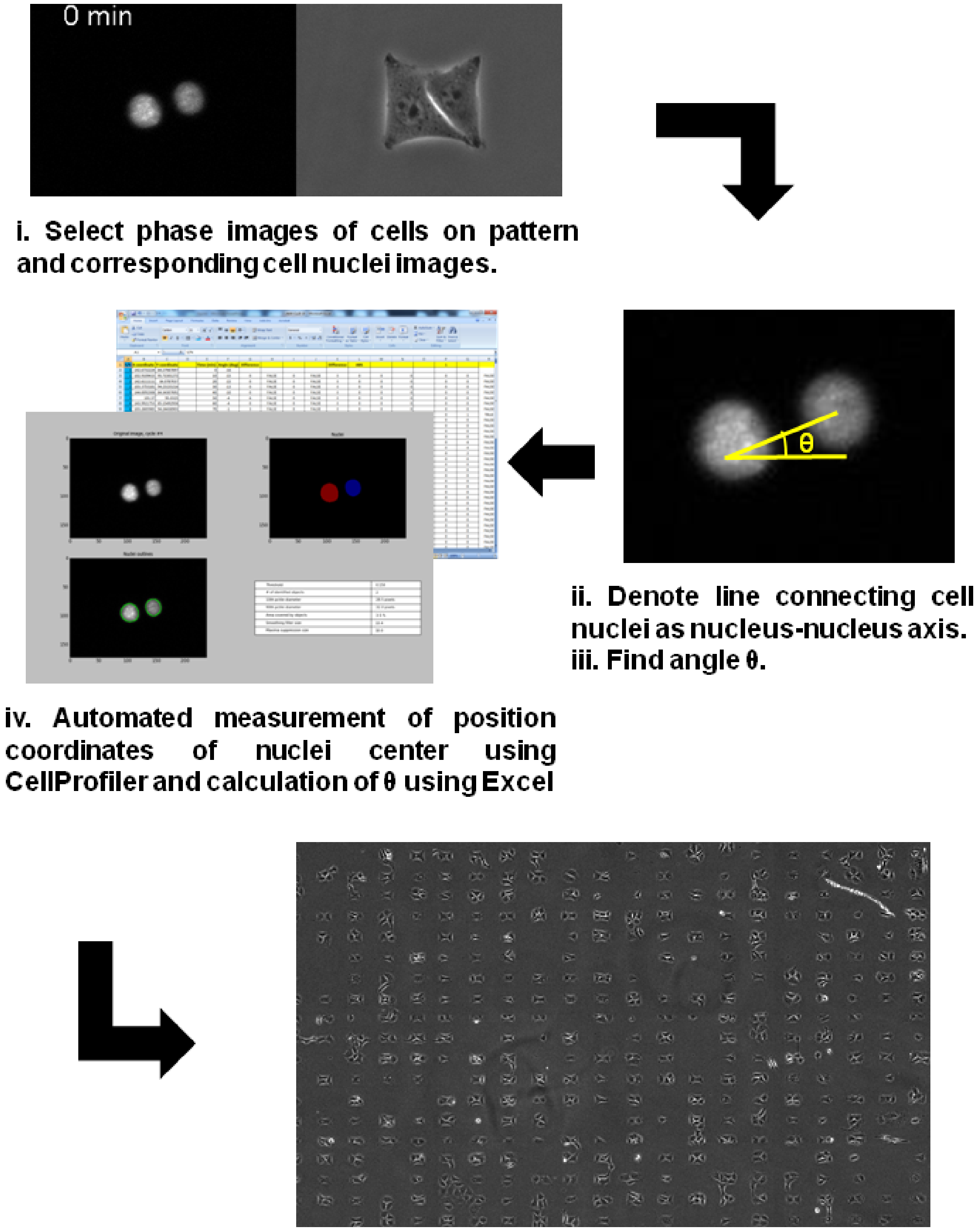

i. Select phase images of cells on pattern and corresponding cell nuclei images.

ii. Denote line connecting cell nuclei as nucleus-nucleus axis.
iii. Find angle θ.

iv. Automated measurement of position coordinates of nuclei center using CellProfiler and calculation of θ using Excel

v. Correction for tilt of pattern array to the horizontal using stitched images

**Fig. 4.1.** Measuring the orientation of the nucleus-nucleus axis, θ for cell pairs.

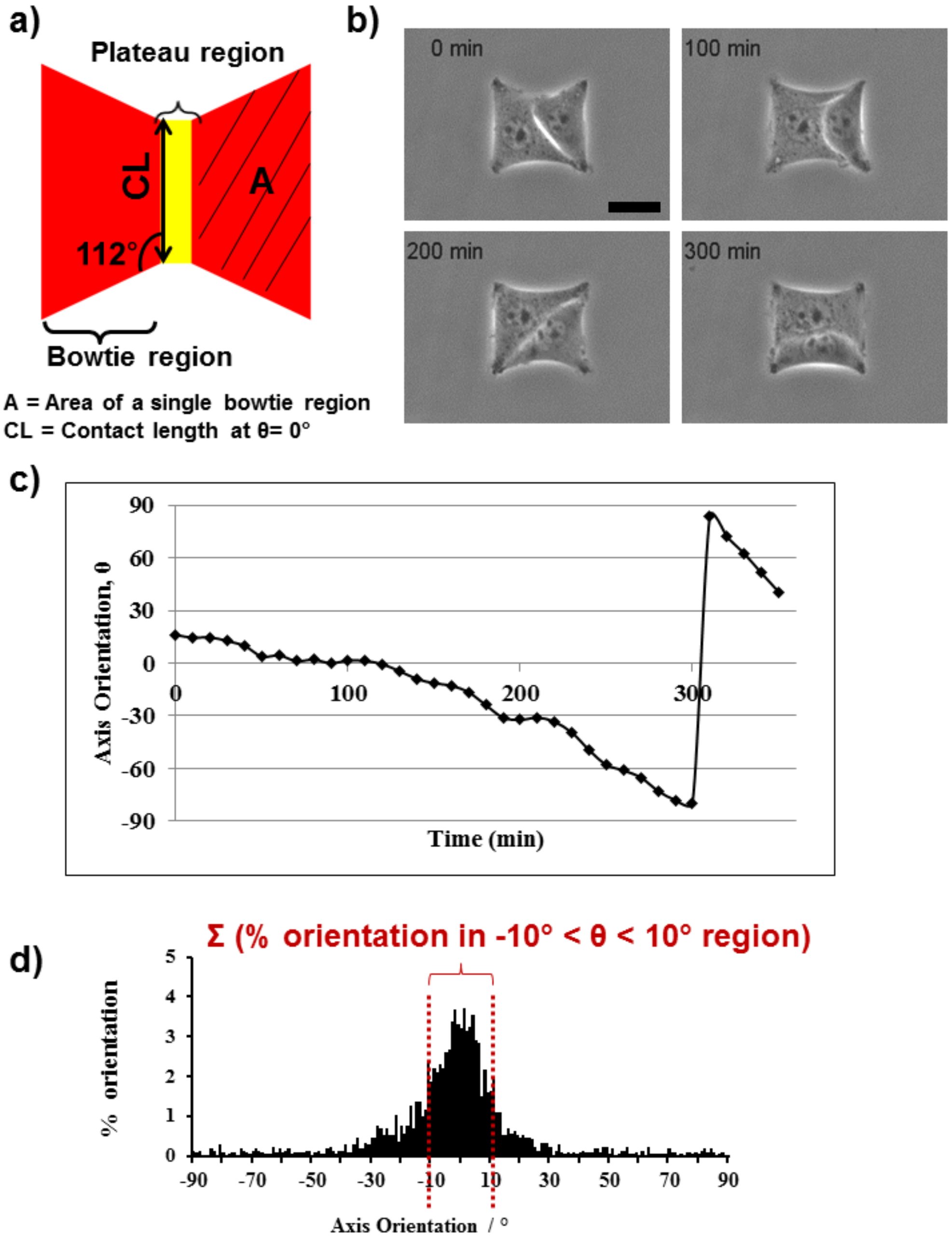

**Fig. 4.2.** Rotating cell pair on bow-tie shaped micropattern. a) Design of bow-tie shaped pattern. b) Time lapse image of a cell pair rotating on A1000 CL 30 bow-tie pattern. c) Plot of θ against time. The jump in the graph represents an exchange in the position of the cells on the pattern as shown in b) at the 300mins time point. d) Summation of θ frequency in the -10° < θ < 10° region to compare cell pairs of the same shape. Scale bar depicts 20 μm.

### 4.2.5 Naming conventions for bow-tie patterns

Bow-tie shaped patterns of different geometries were used to physically constraint a pair of EpH4 cells. When the pair of cells was seeded on these micropatterns, the passivated background of PLL-g-PEG molecules prevented cells adhesion and hence, the cells did not spread beyond the patterned region. This effectively restricted the total area of the cell pair to the area of the bow-tie pattern. The two cells are observed in most cases to share the available area equally. Therefore, the area of a single cell on the bow-tie pattern could be controlled approximately by the area of a single bowtie region as depicted by A in Fig. 4.2.a. Apart from restricting the cell spreading area, the length of the cell-cell contact can also be controlled to some degree by varying the length of the constriction in the bow-tie. At $\theta = 0°$, the contact length is at a minimum. This contact length at $\theta = 0°$ is depicted by CL in Fig. 4.2.a. By fixing the angle at which the bowtie diverges from the constriction at 112° for all bow-tie pattern designs, the geometry of the bow-tie pattern could be fully described by using only the A and CL values. In this chapter, the rotation potential of cell pairs on bow-tie patterns designed with different A and CL was quantified. Bow-tie patterns are named using A and CL according to their corresponding area and contact length. For example, a bow-tie pattern that restricts the single cell area to 1000 $\mu m^2$ and the contact length at $\theta = 0°$ to 30 μm is named A1000 CL30. A plateau region of width 6 μm was incorporated into pattern design as shown in Fig. 4.2.a. This plateau region might be filled with or devoid of ECM to verify the effect of ECM on the motility of constrained cell pairs with what was reported in the literature [131].

### 4.2.6 Characterizing cell pair rotations

Cell pair rotations were characterized in three ways. To average out heterogeneity in the cell population, results from at least 50 cell pairs were used in these characterization methods. In the first method, an average rotation speed was calculated over 6 hour using only rotations where the cell pair moved away from $\theta = 0°$. This could be represented by $\Delta\theta_t/\theta_t > 0$ where $\theta_t$ denoted θ at time t min and $\Delta\theta_t$ denoted the difference between $\theta_t$ and $\theta_{t+10}$. This average value would be a numerical representation of the potential for cell pairs to rotate. The second method characterized the directional bias of the cell rotations. For cell rotations away from $\theta = 0°$, rotations where $\Delta\theta_t > 0$ were considered anti-clockwise rotations while rotations where $\Delta\theta_t < 0$ were considered clockwise rotations. The directional bias of the rotations was calculated by measuring the average frequency of anti-clockwise rotations. In a randomly rotating cell pair, this frequency should be 50%. The first two methods were used for comparing between bow-tie patterns of different shape, size or arrangement. An upper and lower limit of $-10° < \theta < 10°$ was set for the θ used when calculating the average rotation speed to ensure that the shape and contact length of the cell pair do not vary significantly from the bow-tie pattern. The third method of characterization was used to compare the effect of ECM on cell motility where cell pairs are confined to regions of the same shape and size. Hence, data from the full range of $-90° < \theta < 90°$ was used instead. In this method, a summation of the frequency of θ in the $-10° < \theta < 10°$ region was calculated (see Fig. 4.2.d). This summation represents the probability of the finding a cell pair orientated in the $-10° < \theta < 10°$ region. Cell pairs that frequently orientate themselves within this region were regarded as having low spatial motility.

### 4.2.7 Measuring the configuration index of 3-cell clusters

A flow chart showing the steps to measure α from raw images is shown in Fig. 4.3. When three cells are seeded on circular patterns, a configuration index, α could be used to numerically characterize the configuration of the cells with respect to one another. Firstly, the patterns to be analyzed were manually selected according to cell number, cell spreading and cell-cell contact similar to the situation for cell pairs. Also, following what was done for cell pairs, the configuration of the cell nuclei were used to represent the configuration of the cells. In this case, a triangle was fitted to the cell nuclei using the center of each nucleus as one of the triangle vertices. In this way, the dimensions of the triangle could be easily obtained from the position coordinates of the three cells' nuclei. An inscribed circle was then drawn in the fitted triangle and the area of the circle was calculated from the triangle dimensions. When the three cells' nuclei were positioned in a perfectly symmetrical configuration, an equilateral triangle would be fitted which gives the largest inscribed circle. Hence, the idea here was to use the area of the inscribed circle to give a numerical characterization of the configuration of the three cells' nuclei. Since only the relative position of the cell nuclei with respect to one another was important, this area is normalized to the area of the triangle to give $\alpha_0$. $\alpha$ is given by $\alpha = \alpha_0/0.6046$ to set the maximum value of $\alpha$ to 1 for convenience. High throughput characterization of the cell configuration was also done using the CellProfiler software for measuring nuclei coordinates and the Excel software for calculations as in the 2-cell scenario.

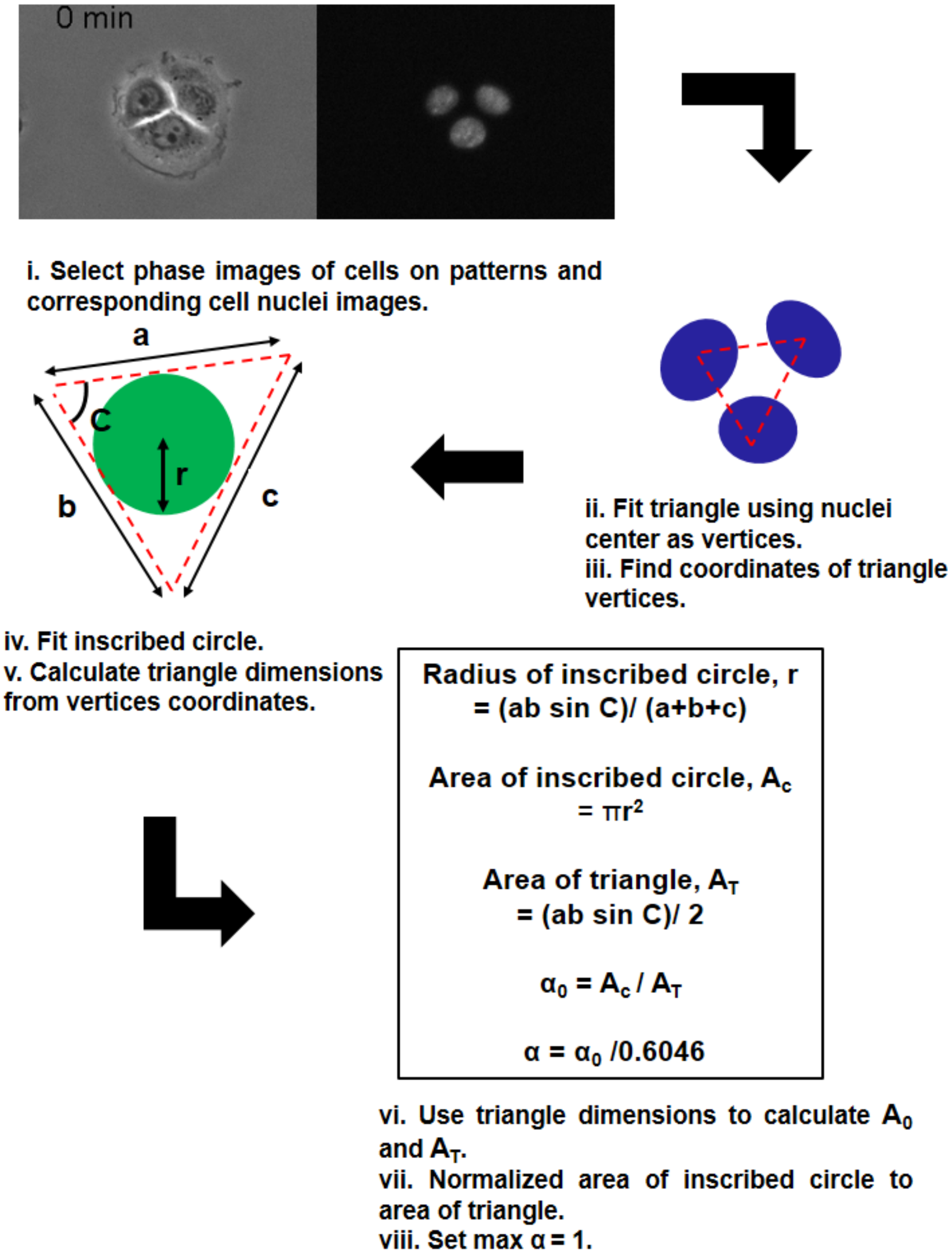

i. Select phase images of cells on patterns and corresponding cell nuclei images.

ii. Fit triangle using nuclei center as vertices.
iii. Find coordinates of triangle vertices.

iv. Fit inscribed circle.
v. Calculate triangle dimensions from vertices coordinates.

Radius of inscribed circle, r $= (ab \sin C)/ (a+b+c)$

Area of inscribed circle, $A_c = \pi r^2$

Area of triangle, $A_T = (ab \sin C)/ 2$

$\alpha_0 = A_c / A_T$

$\alpha = \alpha_0 / 0.6046$

vi. Use triangle dimensions to calculate $A_0$ and $A_T$.
vii. Normalized area of inscribed circle to area of triangle.
viii. Set max $\alpha = 1$.

**Fig. 4.3.** Measuring the configuration index, α of a 3-cell cluster.

## 4.3 Results and discussion

### 4.3.1 Experimental approach

The experimental approach was derived from preliminary observations. Confined cell pairs had been shown in experiments reported by other groups to readily rotate on square patterns [131, 155]. From preliminary results, when a cell pair is seeded on a bow-tie shaped pattern and imaged over a 6-hour period, similar rotational motion was also observed as shown in Fig. 4.2.b. In these rotating cell pairs, the parameter θ had been used to denote the orientation of the nucleus-nucleus axis which represented how the two cells were positioned relative to one another. A closer look at the distribution of θ showed that the cell pair on bow-tie patterns (number of patterns analysed, n = 58) preferentially orientated themselves at low |θ| values while cell pairs seeded on highly symmetrical patterns such as a circle (n = 67) did not show any orientational preference (see Fig. 4.4.a). This difference in the manner at which cell pairs orientated themselves could be attributed to how cell shape and the cell-cell contact length were varied with the rotation of a cell pair. For cell pair rotation on circular patterns, the cells remained close to a semi-circular shape while the cell-cell contact length remained constant with the diameter of the circular pattern. However, for cell pair rotation on bow-tie patterns, very significant changes in cell shape and cell-cell contact length occurred as shown in Fig 4.4.b. Although the orientation of the nucleus-nucleus axis would not be strictly perpendicular to the cell-cell contact, there appears to be a positive correlation between the two. Due to the confinement of the cell pair in the bow-tie pattern, the cell-cell contact length was expected to be longer at larger |θ| values and vice versa. Besides this tendency of cell pairs to orientate at low |θ|, the orientational preference was observed to peak at θ = 0° and this could be regarded as an equilibrium state.

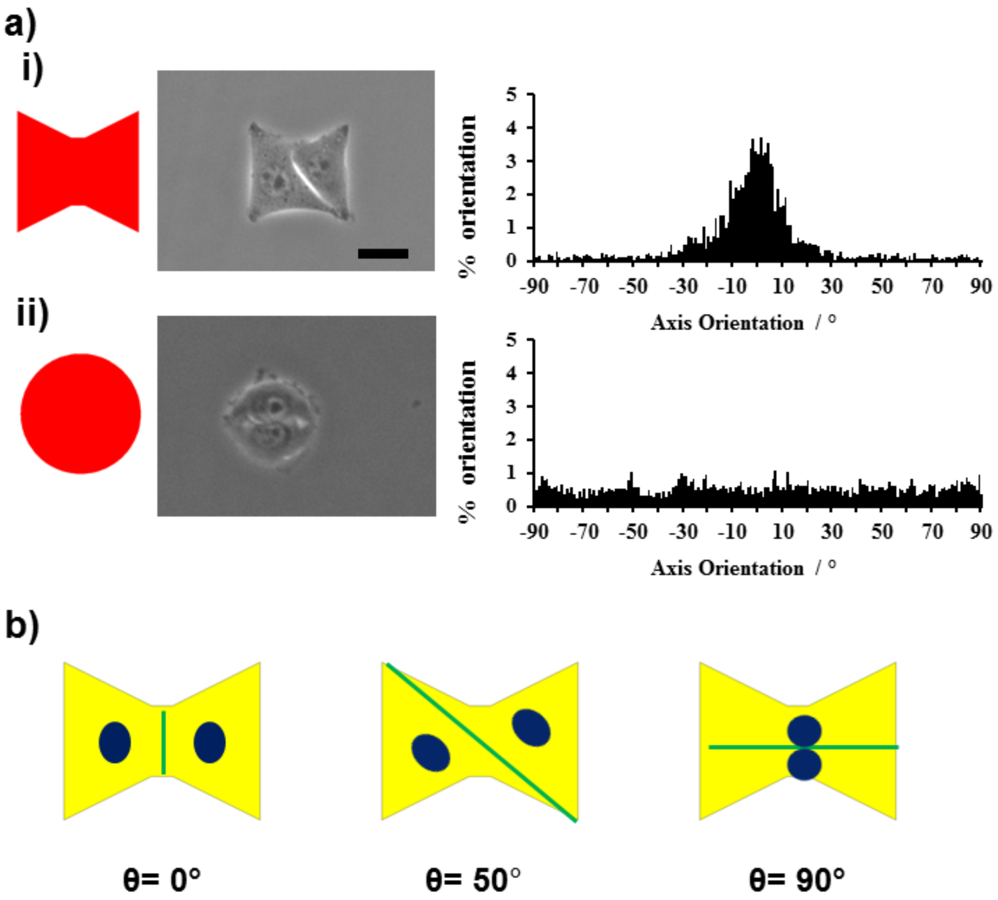

**Fig. 4.4.** Orientational preferences of cell pairs on different shapes. a) Frequency of θ for cell pairs on i) bow-tie pattern (n = 58) and ii) circular pattern (n = 67). Schematics of micropattern used are shown on the left in red. b) Significant changes in cell shape and contact length as cell pair rotates on bow-tie shaped patterns. Nuclei are represented by blue ovals, cell-cell contacts by green lines and cell body is shown in yellow. Scale bar depicts 20 μm.

Many attempts at describing the physical mechanism governing cell rearrangement had been reported using computational models where a shift from a state of mechanical equilibrium was sufficient to induce cell movements [169,170]. Similar approach was used in this chapter to investigate the effect of cell geometry on the rotation of confined cell pairs. Using a cell pair as a minimal model system for confined cell clusters, the potential for cell pairs to rotate on bow-tie patterns of different geometries was quantified. Three rotation modes were observed to exist for cell pairs on bow-tie shaped patterns as shown in Fig. 4.5.a. In the first mode, cell pairs rotated away from the $\theta = 0°$ equilibrium. The second mode was a recovery rotation towards the equilibrium and could be represented by $\Delta\theta_t/\theta_t < 0$. The last rotation mode occurred when cell pair remained stationary as represented by $\Delta\theta_t/\theta_t = 0$. As the potential for cell pairs to rotate is a measure of how easy it would be to physically perturb the cell pair away from their equilibrium position, only the first rotation mode would be considered in the characterization of rotation potential.

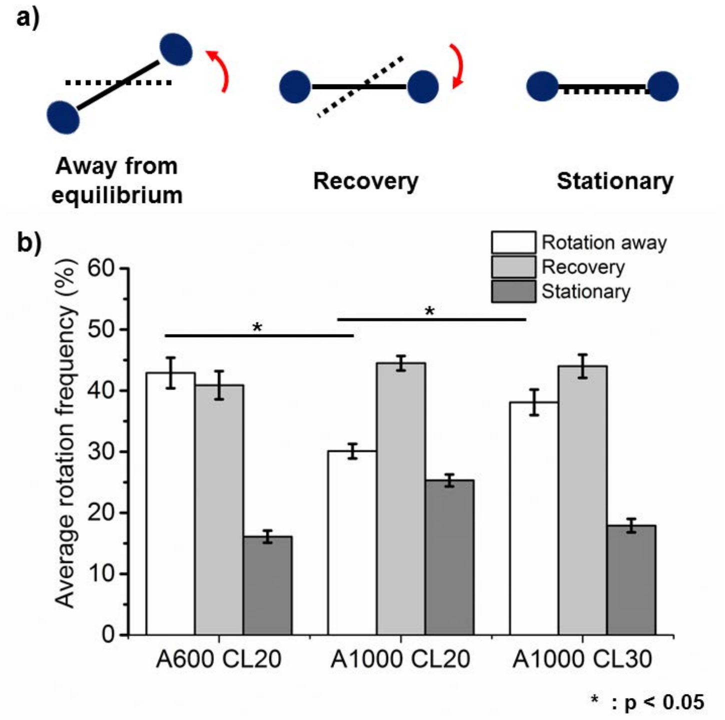

**Fig. 4.5.** Rotation modes of cell pairs. a) Different rotation modes of cell pairs. Nuclei are represented by blue ovals. Nucleus-nucleus axis at time t represented by black solid lines and at time t-10 min by black dotted lines. Only rotation away from equilibrium was considered for quantification of rotation potential. b) Frequencies of cell pairs rotating away from equilibrium, recovery and stationary for three typical bow-tie pattern designs.

### 4.3.2 Effect of contact length and area

To further investigate how the distribution of θ for cell pairs on bow-tie patterns varied with changes in contact length , the distribution of θ was measured for bow-tie patterns with CL = 20 µm (n = 53), CL = 30 µm (n = 60) and CL = 40 µm (n = 70) . The single cell area A was kept constant at 800 µm$^2$. As mentioned previously, the orientation of the nucleus-nucleus axis would not be strictly perpendicular to the cell-cell contact but there appears to be a positive correlation between the two. For a simplified approximation of contact length variations, the cell-cell contact length were assumed to be perpendicular oriented to the nucleus-nucleus axis ie. |θ| + 90°. Also they were assumed to be perfectly confined within the patterns with no significant membrane ‘bridges’ spanning across unpatterned regions. This was found to be generally true for most cases other than highly concave region at the center of the A800 CL40 bowtie pattern. Expected contact length variations at 10° intervals were measured from the different bow-tie patterns. At θ = 0°, expected contact length was estimated by the line bisecting the bow-tie pattern as shown in Fig. 4.6.a. The length of this line is equal to the CL value. The expected contact length at higher θ was estimated by first rotating this bisecting line anticlockwise by θ and then adjusting the length of the line till both ends touches the boundary of the bow-tie pattern as shown in Fig. 4.6.a. These expected contact length are then normalized to their respective CL values for meaningful comparisons between different types of bow-tie pattern. In all patterns, the normalized contact length first increases as θ increases until a maximum at about θ = 40° and then falls gradually (see Fig. 4.6). Comparing the bow-tie patterns A800 CL20 and A800 CL30, it was observed that changes in the normalized contact length was much steeper when CL = 20 µm. Correspondingly, the frequency

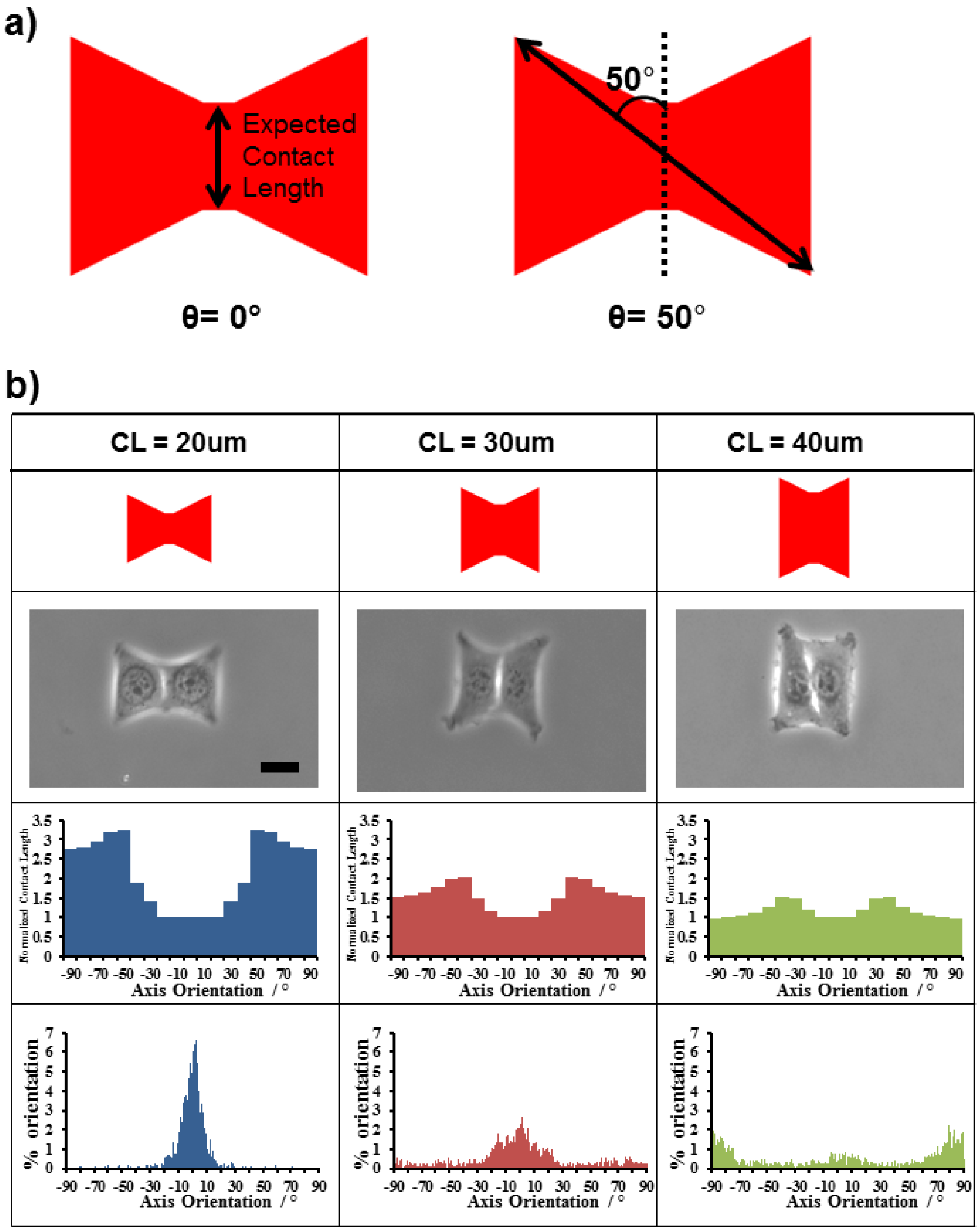

**Fig. 4.6.** Effect of contact length variations on the distribution of θ. a) Measurement of expected contact length. b) Effect of contact length variation on the distribution of θ for cell pairs on A800 CL20 (n = 53), A800 CL30 (n = 60) and A800 CL40 (n = 73) bow-tie patterns. Contact lengths are normalized to CL values. Scale bar depicts 20 µm.

distribution of θ was mainly confined to a sharp peak in the region of $-10° < \theta < 10°$ for the A800 CL20 pattern compared to a more gradual peak in the region of $-30° < \theta < 30°$ for the A800 CL30 pattern. Also, almost negligible amount of cell pairs were found to be orientated at $\theta > 10°$ for the A800 CL20 pattern while a small number of cell pairs could still be found orientated at $\theta > 30°$ for the A800 CL30 pattern. Interestingly, for patterns where CL = 40 µm, the cell pairs tend to orientate themselves perpendicularly to the pattern. Besides having a value of close to 1 for the normalized contact length at $|\theta| = 90°$, this anomaly could also be accounted for by the formation of significant membrane 'bridges' across the concave region at the center of the pattern which increases the contact length at small |θ| values. As shown in Fig. 4.6, the membrane 'bridges' caused the cell pair on the A800 CL40 pattern to deviate from a bowtie shape. This set of results clearly showed that confined cell pairs prefer to position themselves to minimize their contact length. Also, cell pairs rotating on confined patterns might experience a resistance to increase their contact length which becomes more significant if this increased in contact length was larger. Taken together, the motility of confined cell pairs was found to be highly dependent on overall shape of the pattern.

To investigate how absolute values of contact length affect the rotation potential of confined cell pairs, the average rotation speed of cell pairs away from the $\theta = 0°$ position on bow-tie patterns A800 CL20 and A800 CL30 was measured and compared as shown in Fig. 4.7.a. The average rotation speed was calculated to be 14.3 °/hr (n = 53, S.E.±0.6) when CL = 20 µm and 23.3 °/hr (n = 60, S.E.±1.6) when CL = 30 µm. The experiment was repeated using bow-tie patterns A1000 CL20 and A1000 CL30 where the single cell area is kept constant at 1000 $\mu m^2$. An average rotation speed of 10.9 °/hr (n = 59, S.E.±0.3) was calculated for cell pairs on the CL20 pattern and an average rotation speed of 16.4 °/hr (n = 58, S.E.±1.2) for cell pairs on the CL30 pattern as shown in Fig. 4.7.a. In both cases, average rotation speed was found to be higher when the contact length is high. CL40 patterns were not used in these experiments as only a few cell pairs orientated themselves in the -10° < θ < 10° region used for calculations while the cell-cell contact were generally unstable when CL is less than 20 µm. Interestingly, there also appeared to be a significant increase in the frequency of cell pairs rotating away from the equilibrium on A1000 CL30 patterns compared to A1000 CL20 patterns (Fig. 4.5.b). In summary, both experiments involving contact length variations and absolute values of contact length showed that the motility of the cell pairs was highly sensitive to the contact length of the cell-cell junction formed between the cells.

Besides contact length, cell area could also possibly influence the potential for cells to rotate on micropatterns. Average rotation speed of cell pairs on bow-tie patterns of different single cell area A but constant CL of 20 µm was measured and compared as shown in Fig. 4.7.b. The average rotation speed of cell pairs on the A600 CL20 pattern was calculated to be 15.1 °/hr (n = 62, S.E.±1.0). Compared to the values calculated for cell pairs on the A800 CL20 pattern, average rotation speed was slightly higher on A600 CL20 patterns but there is no statistical difference between the rotation speeds. However, when cell pairs on both A600 CL20 and A800 CL20 patterns were compared to cell pairs on A1000 CL20 patterns, it was noted that the average rotation speed was significantly higher for cell pairs on the smaller patterns in both cases. Interestingly, the frequency of cell pairs rotating away from the equilibrium also increased on A600 CL20 patterns compared to A1000 CL30 patterns (Fig. 4.5.b) These results suggested that the potential for cell rotation of confined cell pairs did not change with cell area when the cells are small and only decreased if the spreading area of the cells became very large.

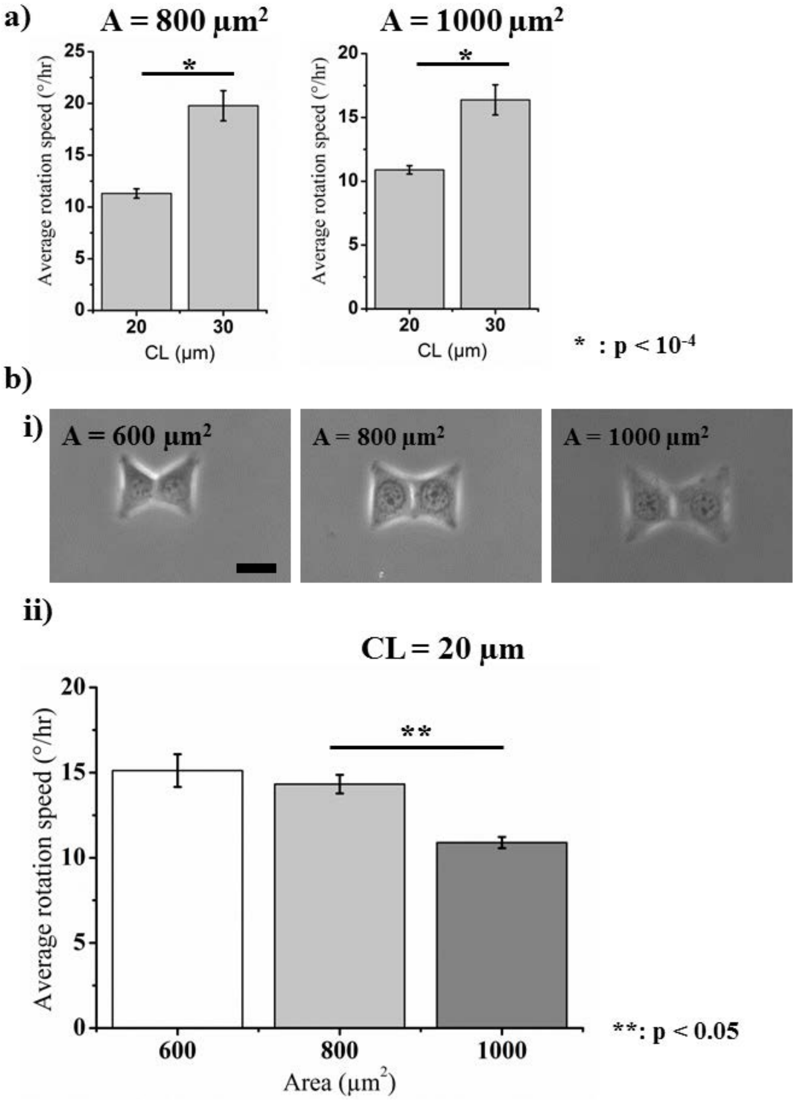

**Fig. 4.7.** Effect of contact length and cell area on rotation potential. a) Effect of contact length on average rotation speed for pattern areas A= 800 µm$^2$ and A= 1000 µm$^2$. Cells had a higher rotation speed on A800 CL30 (n = 60) and A1000 CL30 (n = 58) patterns compared to A800 CL20 (n = 53) and A1000 CL20 (n = 59) patterns. b) (i)Phase contrast images of cell pairs on bow-tie shaped patterns of different areas. Cells on A600 CL20 (n = 62) patterns had a rotation speed of 15.1 °/hr. Scale bar depicts 20 µm. (ii) Effect of single cell area on average rotation speed for contact length CL = 20 µm. Error bars depict S.E. statistics.

### 4.3.3 Quantification of focal adhesion density

It has been reported in earlier studies that increased localization of molecules involved in focal adhesions (e.g. vinculin) was observed at the cell periphery when the area of the cell increases [52]. It is very likely that focal adhesions could play a key role in modulating the rotation speeds of constrained cell pairs since the disassembly of focal adhesions are thought to be an essential step for cells to move in any manner. To investigate how the focal adhesion density at the periphery of the cells could vary with cell area, immunofluorescence staining of cell pairs were performed on cells seeded on A600 CL20, A800 CL20 and A1000 CL20 patterns. Phosphorylated paxillin antibodies were used to reveal paxillin molecules that were specifically localized to focal adhesions and not cytosolic paxillin. As expected, phosphorylated paxillin-containing focal, typically found at the ends of actin filaments, were concentrated at the cell periphery especially at the sharp corners of the bowtie-shaped patterns (see Fig. 4.8.a). The density of these focal adhesions was quantified by measuring the total area of the immunofluorescence stains for each cell pair. Total focal adhesion areas for cell pairs seeded was found to be 50.9 $\mu m^2$ (n = 53, S.E.±4.4) when A = 600 $\mu m^2$, 58.9 $\mu m^2$ (n = 65, S.E.±4.1) when A = 800 $\mu m^2$ and 72.5 $\mu m^2$ (n = 57, S.E.±4.7) when A = 1000 $\mu m^2$. These results showed that the focal adhesion density at the cell periphery increases as the cell area increases. Furthermore, it appears that this increase was amplified when the cell area becomes larger which is highly reminiscent of previous results reported based on single cells seeded on square-shaped micropatterns [52].

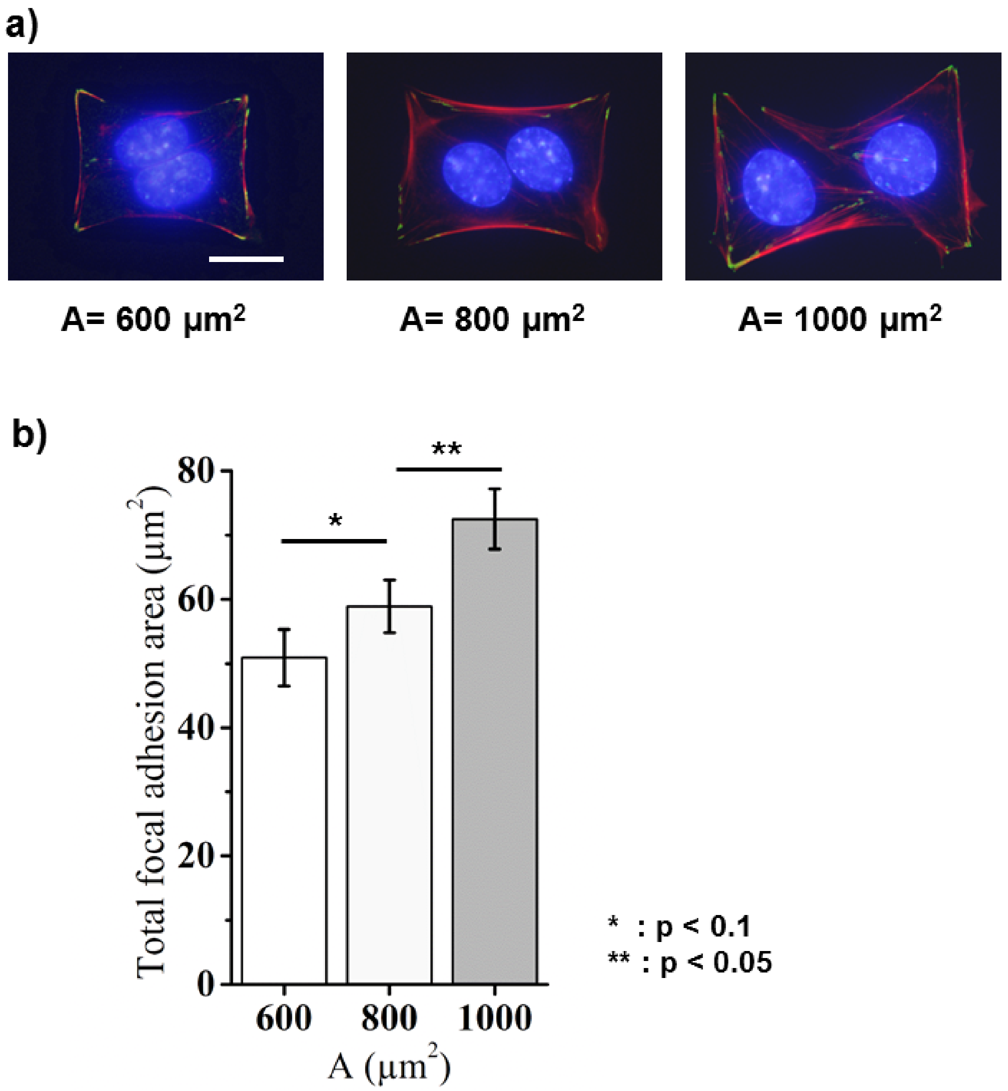

**Fig. 4.8.** Quantification of focal adhesion density. a) Immunofluorescence staining for phosphorylated paxillin (green), actin filaments (red) and cell nuclei (blue) in cell pairs seeded on A600 CL20, A800 CL20 and A100 CL20 patterns. Scale bar depicts 20 µm. (b) Measurement of total focal adhesion area in cell pairs seeded on A600 CL20 (n =53), A800 CL20 (n=65) and A100 CL20 (n =57) patterns. Error bars depict S.E. statistics.

### 4.3.4 Proposed mechanism governing cell pair rotations

Based on experimental results on cell-cell contact length and single cell area, as well as results reported in the literature, a force-mediated mechanism to explain the physical principles governing rotation of constrained cell pairs is proposed. Firstly, since the cell pairs are generally well spread with cell thickness negligible compared to the surface dimensions of the micropatterns, the cell pair is treated as a 2D object. From traction force microscopy results reported by other researchers, cell-ECM traction forces that are orientated perpendicularly to the cell-cell junction had been implicated in the rotation of cell pairs confined on micropatterns [131]. To balance the forces acting on each cell, forces exerted by the cell-cell contact must be equal to these ECM-traction forces. Cell-cell contact forces had been confirmed in a separate study to orientate perpendicularly to the cell-cell junction and more interestingly appeared to be concentrated at the edges of the cell-cell contact [171]. If cell-cell forces are indeed responsible for cell pair rotation and are concentrated at the contact edges, these forces could be coupled to the length of the cell-cell junction to form a rotational moment. An overall net rotational moment could be the origin of the driving force behind cell pair rotations on micropatterns and is the basis for the proposed mechanism. This would also explain how the contact length of the cell pair would be correlated to the rotation potential of cell pair.

To further develop the proposed mechanism, it is postulated that there exist intrinsic forces that oppose cell pair rotations and these rotations should be more completely described as a net effect between the driving forces for rotation and these resisting forces. Besides the contact length, cell area was also implicated in the determination of the potential for cell pair rotation. Based on the experimental results shown in this chapter, rotation potential of cell pairs appeared to be independent of cell area when the cells are small and only decreased significantly with area when the cells were well spread. To explain this experimental observations, one needs to explore how driving and resisting forces changes with an increase in cell area.

Focal adhesions may be a likely candidate for the origin of resisting forces that suppresses cell pair rotations. From the results shown in Fig.4.8, focal adhesion density appeared to increase with cell area at an increasing rate. This is consistent with published data from single cells seeded on square shaped patterns [52]. Besides focal adhesion density, another potential candidate that may contribute to resisting cell pair rotations is the stiffness of the cells. Cell stiffness had previously showed a positive correlation with cell spreading area [172] and had been reported to be an important determinant in the motility of cancer cells [173].. In bowtie patterns, an increase in cell area would be accompanied by an elongation of the cell as CL was kept constant. Since, cell elongation was also reported to be positively correlated to cell stiffness [174] the increase in cell stiffness with area is also likely to occur at an increasing rate. Taken together, it may be reasonable to expect the resisting force to increase with area at an increasing rate.

As cell area increases, a corresponding increase in cell-ECM traction forces and hence the cell-cell forces had been reported [175]. Driving forces for rotation was obtained from a net difference between rotational moments at the top and bottom of the cell-cell contact and would be positively correlated to the degree of fluctuations in cell-cell forces. These fluctuations originated from corresponding fluctuations in the cell-ECM traction forces which had been shown to increase when intracellular contractility was reduced [176]. In this way, increase in area would likely increase the driving force in general (through an increase in cell-cell forces) but at a decreasing rate (through a decrease in fluctuations in cell-cell forces).

If the driving and resisting forces do vary with area in the manner described above, the observed relationship between rotation potential and cell area could be explained. When the cell areas are small, an increase in cell area may cause a comparable increase in both driving and resisting forces of rotation. Hence, this increase in area would have a negligible effect on rotation potential. However, at large cell areas, the increase in resisting forces would be larger than that of the driving forces, causing a drop in rotation potential.

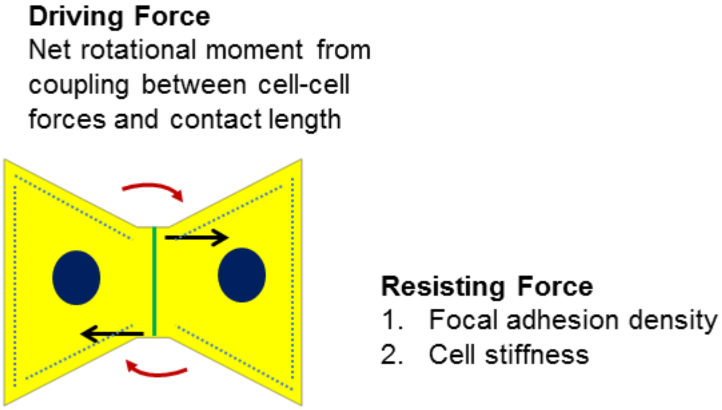

**Fig. 4.9.** Proposal of mechanism to explain the physical principles governing cell pair rotations on bow-tie patterns. Schematic diagram of proposed mechanism. Interplay between driving and resisting forces governs cell rotations. Nuclei are represented by dark blue ovals, cell-cell contacts by green lines, focal adhesions by light blue dots and cell body is shown in yellow. Black arrows depict net cell-cell forces and red arrows depict net rotational moment.

### 4.3.5 Effect of cell shape asymmetry

To validate the proposed mechanism, three further experiments were carried out. In the first of these experiments, redesigned patterns with shape asymmetries were designed. Besides the magnitude of the rotation speed, the direction of the rotation may also be affected by the micropattern that the cell pairs reside on. For clarity in description, asymmetry was described with reference to x- and y- axes where the origin was located at the center of the pattern (see Fig. 4.10.a.i). In bow-tie patterns that are symmetrical about both the x- and y- axes, there appeared to be no preference in the direction at which the cell pairs tend to rotate. For the different types of bow-tie patterns described so far, the frequencies of anti-clockwise rotations were measured. 52.9% (S.E.±5.5), 52.7% (S.E.±5.4), 50.1% (S.E.±6.5), 52.3% (S.E.±4.6) and 56.5% (S.E.±4.8) of the rotations were anti-clockwise for cell pairs on A600 CL20, A800 CL20, A800 CL30, A1000 CL20 and A1000 CL30 patterns respectively as shown in Fig.4.10.a.ii. These results were very close to the 50% anticlockwise rotation expected for randomly rotating cells.

To understand how micropattern shape would affect the direction of cell pair rotations, pattern shapes were redesigned. For the first redesigned pattern, instead of being bow-tie shaped, the bottom of a A1000 CL30 pattern was flatten to generate asymmetry about the x-axis (see Fig. 4.10.b.i). Also, instead of cell shape diverging away from the contact length (named 'diverging' patterns), similar patterns that allow the cell shape to converge from the contact length (named 'converging' patterns) were also designed (see Fig. 4.10.b.iii). These patterns were highly symmetrical about the y-axis when |θ| was small and were named 'symmetrical' patterns. To generate even more asymmetry in the cell shape, the right half of the pattern was rotated 180° in both of these designs to form patterns that are asymmetrical about both the x- and y- axes (see Fig. 4.10.b.ii and Fig. 4.10.b.iv) and named 'asymmetrical' patterns. In these patterns, the frequency of anti-clockwise rotations was measured. For symmetrical patterns, 56.7% (n = 59, S.E.±4.5) and 52.3% (n = 60, S.E.±5.4) of the rotations were observed to be anti-clockwise for diverging and converging patterns respectively (see Fig. 4.10.c). Again, these results were close to the 50% anticlockwise rotation expected for randomly rotating cells. For asymmetrical patterns, 32.0% (n = 70, S.E.±4.0) and 70.9% (n = 51, S.E.±5.3) of the rotations were observed to be anti-clockwise for diverging and converging patterns respectively (see Fig. 4.10.c). This result showed that asymmetrical diverging patterns preferentially rotate in a clockwise direction while asymmetrical converging patterns preferred to rotate in an anti-clockwise direction. Putting these results together, a bias in rotation direction appeared to emerge only in cell pairs where there was an asymmetry about the cell-cell contact.

The average rotation speed was also calculated for cell pairs on these redesigned patterns to examine the effect of pattern shape on rotation potential. Average rotation speed for clockwise and anticlockwise rotations for diverging cells pairs on symmetrical and asymmetrical patterns was compared separately (see Fig. 4.10.d). The results showed that asymmetry about the cell-cell contact did not result in any significant differences in the potential for cell pair to rotate in both clockwise and anticlockwise direction even though a rotational bias was observed. Similar observation was obtained for converging cell pairs. Taken together, these results showed that while the direction of cell pair rotations were highly sensitive to cell shape asymmetry, the rotation potential appeared to be more dependent on parameter such as single cell area and contact length, as least in the case of these A1000 CL30 patterns. However, cell pairs rotated in a persistent direction on asymmetrical redesigned patterns and were likely to experience higher overall rotational amplitudes than symmetrical redesigned patterns.

Looking closer at experiments involving these patterns, a pattern that is asymmetrical about the x-axis would be expected to give rise to a similar asymmetrical distribution of cell-ECM traction forces in the cell. If the cell-cell forces that balance this cell-ECM traction forces are indeed concentrated at the edges of the cell-cell junction, the cell-cell forces at the top and bottom edges of the junction would be different. To verify this proposition, calyculin A was used to initiate the rupture of the cell-cell contact between cell pairs on redesigned patterns. As reported by other groups, the stability of cell-cell junctions could be determined by the size of the junction and the tugging force acting on

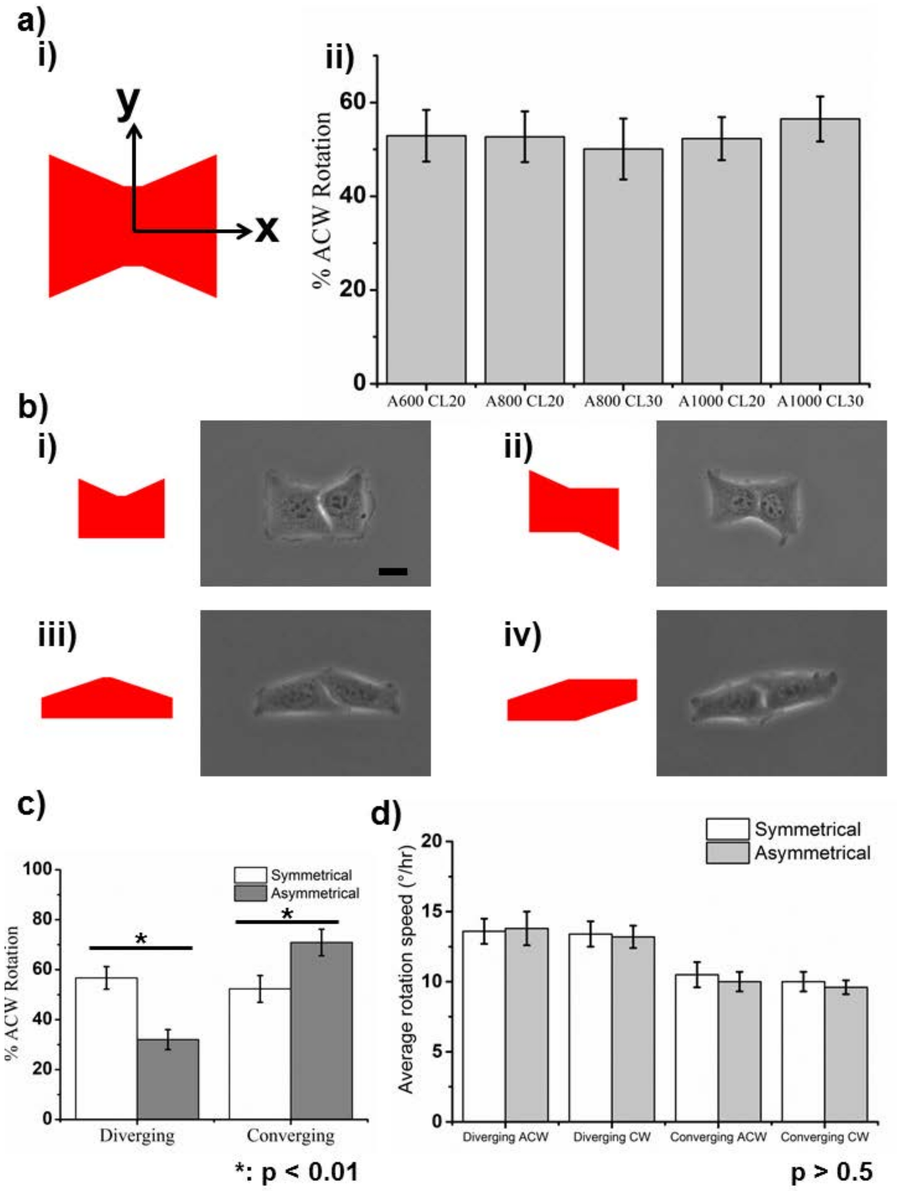

**Fig. 4.10.** Effect of shape asymmetry on the direction of cell pair rotation. a) (i) Bow-tie patterns are symmetrical about both x- and y-axis. (ii) Frequency of anti-clockwise rotations for cell pairs on bow-tie patterns. b) Cell pairs seeded on redesigned patterns that are asymmetrical about (i),(iii) x-axis only or (ii), (iv) both x- and y- axis. Schematics of (i), (ii) diverging and (iii), (iv) converging micropatterns used are shown on the left in red. c) Frequency of anti-clockwise rotations for cell pairs on redesigned patterns. Cells on asymmetrical diverging (n = 70) and converging (n = 51) patterns had a rotation bias compared to cells on symmetrical diverging (n = 59) and converging (n = 60) patterns d) Average rotation speed on redesigned patterns. Scale bar depicts 20 μm. Error bars depict S.E. statistics.

the junction [177]. Since the size of the junction was kept constant by the micropatterns, any changes in tugging force would play a critical role in determining the stability of the cell-cell junction. Calyculin A is an unspecific phosphatase inhibitor which is known to increase the overall cellular tension and hence the tugging force on the cell-cell junction [177]. An increase in tugging force would eventually lead to a rupture in the cell-cell junction. To maximize the asymmetry in cell-cell forces at top and bottom edges of the cell-cell junction, symmetrical redesigned patterns were used. 1nM calyculin A was added to cell pairs seeded on these patterns and time lapse images were taken at 5 minutes interval until the cell-cell junction was totally disrupted or when the cells totally round up due to an increase in cellular tension.

For diverging patterns, it was observed that if the cell-cell junction did rupture before the cell pair started to round up, the rupture tends to (9 out of 12 cases observed) occur at the bottom edge (see Fig. 4.11.a.). This result suggests that the cell-cell forces at the bottom edge could be larger than that at the top edge. Based on the proposed mechanism, this information could be used to predict the preferred rotation direction in asymmetrical redesigned patterns which was consistent with experimental observations (see Fig. 4.11.c.ii). A similar procedure for estimating the cell-cell forces at the top and bottom edges was carried out for converging patterns and again the preferred rotation direction in asymmetrical redesigned patterns could be predicted successfully (7 out of 11 cases) based on the proposed model (see Fig. 4.10.d.ii). Although the number of observed cases was severely limited by cell rounding with increased cell contractility, the results from these experiments on redesigned pattern indicated that the proposed mechanism is potentially valid.

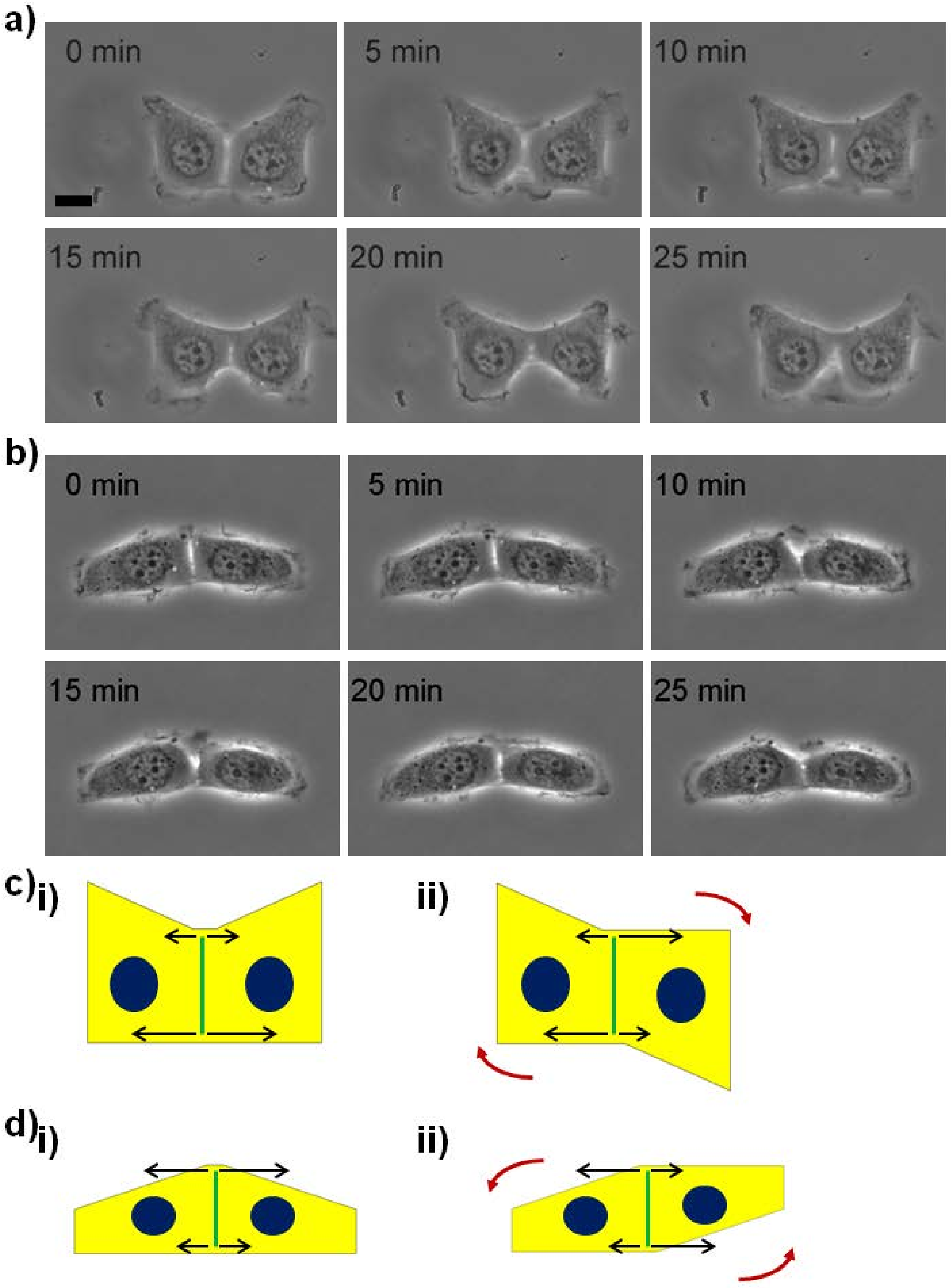

**Fig. 4.11.** Verification of cell-cell forces at contact edges using 1nM Calyculin A treatment of symmetrical redesigned patterns. Timelapse phase images of a) diverging patterns and b) converging patterns at 5 min intervals. Schematics of cell-cell forces and net rotational moment in c) diverging and d) converging (i) symmetrical and (ii) asymmetrical redesigned patterns. Nuclei are represented by dark blue ovals, cell-cell contacts by green lines, and cell body is shown in yellow. Black arrows depict net cell-cell forces and red arrows depict net rotational moment. Scale bar depicts 20 μm.

### 4.3.6 Effect of an ECM gap between the bow-tie regions

In the second of these validation experiments, an ECM gap was designed between the bow-tie regions. Cell-cell junctions had been reported in square-shaped cell pairs to spatially stabilize in regions that were devoid of ECM [131]. To verify this finding in bow-tie patterns, the plateau region was devoid of ECM and an ECM gap was created between bow-tie regions (see Fig. 4.2.a). Cell pairs were seeded on a variety of bowtie patterns with different distributions of ECM at the different pattern geometries used so far. Phase images of cell pairs seeded on these patterns confirmed that the presence of the ECM gap did not affect the shape and size of cell pairs residing on them (See. Fig. 4.12.a.). A distribution of θ was obtained for cell pairs on each of these patterns and the total frequency of θ in the $-10° < \theta < 10°$ region was calculated. This value gave the probability for a cell pair to be orientated in this low $|\theta|$ region and was taken to be inversely related to the spatial motility of the cell pair. Spatial motility of cell pairs was compared between patterns of the same geometry but with different ECM distributions (see Fig. 4.12.b). The results clearly indicated a significant increase in spatial motility for cell pairs residing on patterns without the ECM gap (except the A1000 CL20 set of patterns) consistent with reported results using square-shaped cell pairs. Interestingly, by comparing the p-values between patterns of different geometries, it was observed that the differences in cell pair motility were more significant if A was smaller or if CL was larger. As the presence of an ECM gap had been shown to affect cell-cell forces in square-shaped cell pairs, these results showed that the single cell area and the contact length of the cell pairs were important determinants in how much changes in cell-cell forces would affect the rotation dynamics of cell pairs.

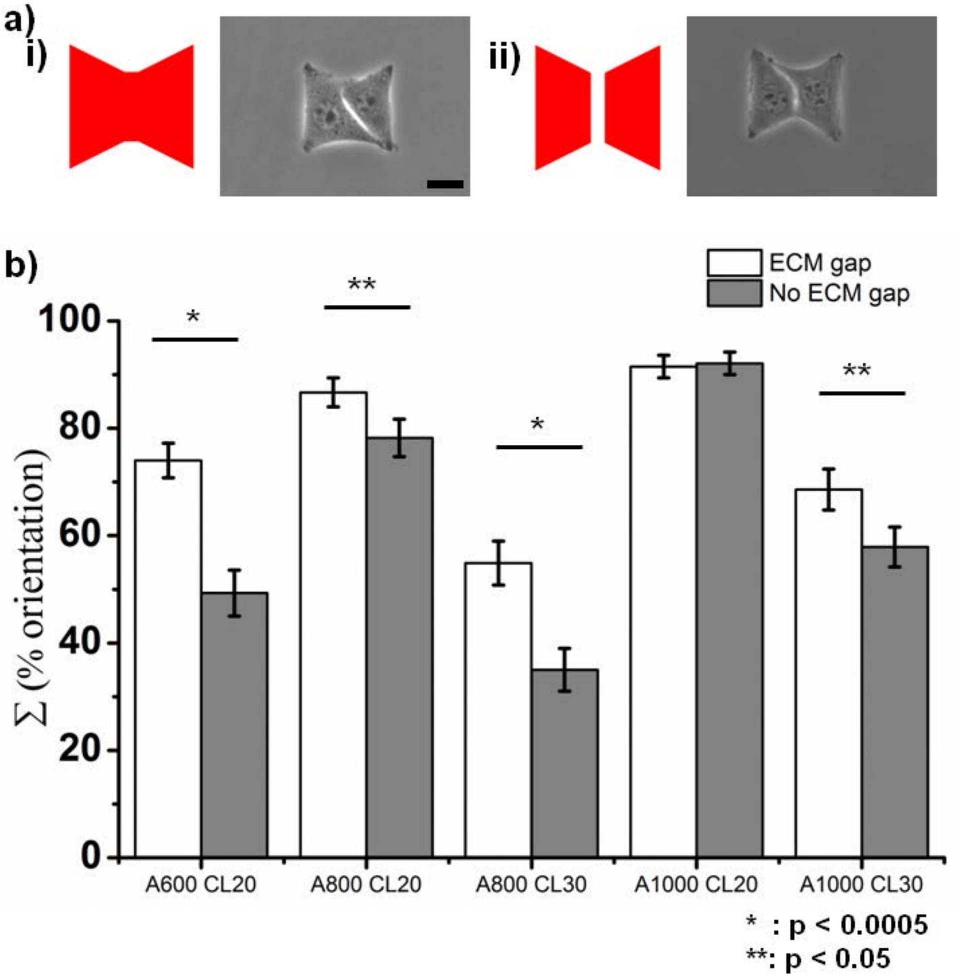

**Fig. 4.12.** Effect of an ECM gap on the spatial motility of cell pairs on bow-tie patterns. a) Phase images showing the shape and size of cell pairs on a A1000 CL30 pattern (i) without ECM gap and (ii) with ECM gap. Schematics of micropattern used shown on the left in red. b) Plot comparing the spatial motility of cell pairs on bow-tie patterns with or without ECM gap. Increase in spatial motility for cell pairs residing on patterns with ECM gap for A600 CL20 (n = 65), A800 CL20 (n = 65), A800 CL30 (n = 67) and A1000 CL30 (n = 59) patterns. No such increase in spatial motility observed for cell pairs on A1000 CL20 (n = 53) patterns with ECM gap. Scale bar depicts 20 µm. Error bars depict S.E. statistics.

### 4.3.7 Drug Treatment

In the last of these validation experiments, constrained cells pairs were exposed to actomyosin contractility inhibitors. Actomyosin contractility has been identified from earlier experiments to play a prominent role in the motility of constrained cell clusters [178], including the rotation of cell pairs in micropatterned substrates [131]. Here, inhibition of ROCK by Y27632 and myosin light chain kinase (MLCK) by ML7 was performed. Both ROCK and MLCK are active players in the Rho-ROCK pathway and the inhibition of these kinases would be useful to probe how these crucial components of actomyosin contractility could affect cell pair rotation dynamics. A low drug dose of 1-2 μM was used in these experiments. This is due to longer drug exposure time as cells on the bowtie patterns were exposed to the drugs throughout the whole imaging period of 6 hrs unlike similar studies where drug exposure time was relatively shorter.

First DMSO, which was used to dissolve these inhibitors, was verified to have no effect on cell pair rotations when the cells are treated at the concentrations used in actual experiments (results not shown). When a dose of 1 μM was used for Y27632 and ML7, the average rotation speed of cell pairs on A1000 CL20 patterns were found to be 10.9 °/hr (n = 58, S.E.±0.5), and 11.0 °/hr (n = 62, S.E.±0.5) respectively. When compared to untreated cell pairs with an average rotation speed of 10.9 °/hr (S.E.±0.3), the results showed no significant difference in rotation potential (see Fig. 4.13.a). When inhibitors of the same dose was used for cell pairs on A600 CL20 patterns, the average rotation speed of cell pairs was found to be 13.3 °/hr (n = 58, S.E.±0.7) for cell pairs under Y27632 treatment. These results were significantly lower than average rotation speed of untreated cell pairs at 15.9 °/hr (S.E.±1.2). On the other hand, treatment of cell pairs with ML7 gave an average rotation speed of 15.0 °/hr (n = 66, S.E.±0.9) which was comparable to that of untreated cell pairs (see Fig. 4.13.b.). When this experiment was again repeated on cell pairs residing on A1000 CL30 patterns, similar trend was observed. Average rotation speed of the cell pairs was found to be 13.8 °/hr (n = 51, S.E.±0.6) when treated with Y27632. This was significantly lower than average rotation speed of untreated cell pair at 16.4 °/hr (S.E.±1.2). Again, when treated with ML7, the average rotation speed of 15.2 °/hr (n = 62, S.E.±0.9) was not found to be significantly different (see Fig. 4.13.c).

Taken together, these experiments showed that parameters such as single cell area and contact length could affect how cell pairs respond to drug treatment at the same dose. Inhibition of ROCK by Y27632 treatment would lower actomyosin contractility and was found to reduce the average rotation speed of cell pairs. However, even though both ROCK and MLCK are thought to be important in the Rho-ROCK pathway, inhibition of MLCK activity did not seem to affect cell pair rotation speed. To further examine the effect of the inhibitors at a higher dose, cell pairs on A1000 CL20 patterns were treated with 2 µM ROCK and 2 µM ML7. This time, a significant decrease in average rotation speed was observed for Y27632 treated cell pairs with a rotation speed of 9.5 °/hr (n = 50, S.E.±0.4). Interestingly, as shown in Fig. 4.13.d, when cell pairs are treated with ML7 at this dosage, the average rotation speed increases to 12.7 °/hr (n = 50, S.E.±0.6). Taken together, these results confirmed that the effect of Y27632 treatment was amplified on cell pairs with smaller cell areas and longer contact lengths. Conversely, the effect of ML7 treatment did not appear to be affected by pattern geometries and a surprisingly increase in rotation potential was observed when cell pairs were treated with 2uM ML7.

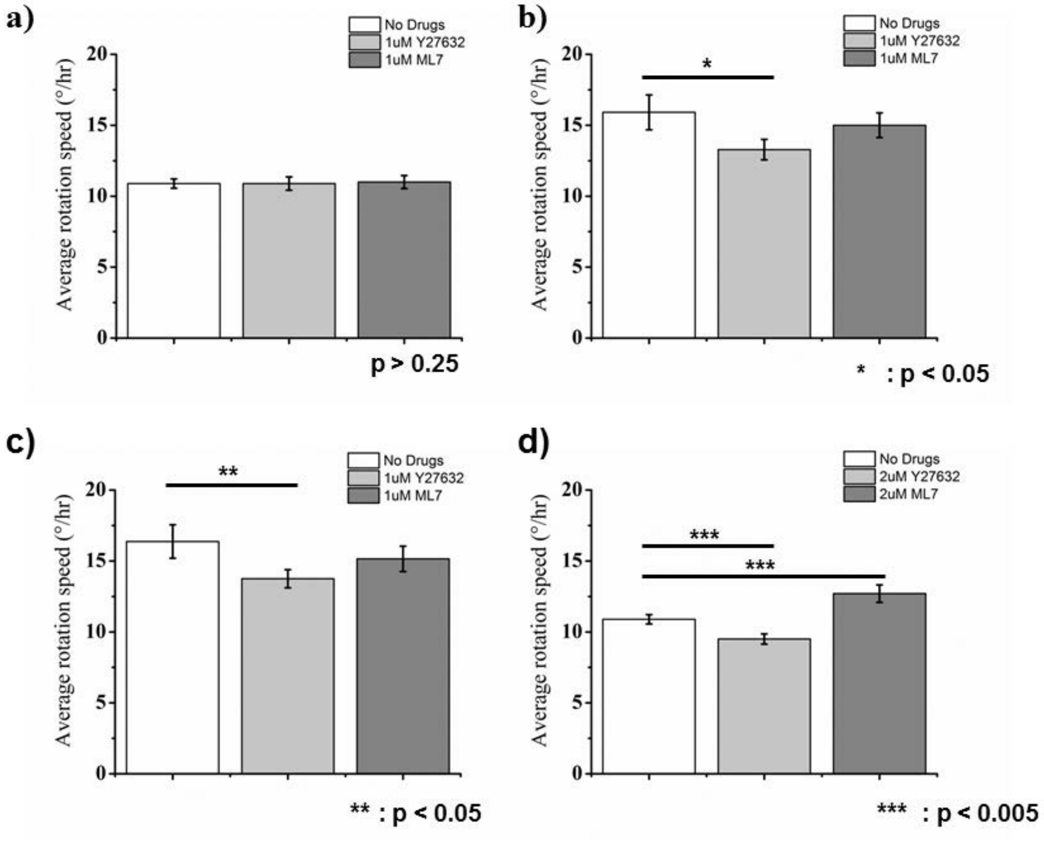

**Fig. 4.13.** Effect of Y27632 and ML7 treatment on the rotation potential of cell pair on different bow-tie patterns. Average rotation speed of cell pairs treated with 1μM Y27632 and 1μM ML7on a) A1000 CL20 patterns ($n_{Y27632} = 58$, $n_{ML7} = 62$), b) A600 CL20 patterns ($n_{Y27632} = 58$, $n_{ML7} = 66$) and c) A1000 CL30 patterns ($n_{Y27632} = 51$, $n_{ML7} = 62$). d) Average rotation speed of cell pairs treated with drugs at double dose on A1000 CL20 patterns ($n_{Y27632} = 50$, $n_{ML7} = 50$). Error bars depict S.E. statistics.

### 4.3.8 Effect amplification at small cell area or long cell-cell contact length

In experiments involving bowtie patterns with different distribution of ECM and when cell pairs were treated with Y27632, changes in rotation potential were amplified in patterns where cell area was small or where contact length was long. Treatment of cell pairs with ML7 yielded very different results where the effect of the drug treatment did not appear to vary with pattern geometries. These observed results were in agreement with the proposed mechanism where it is clear that changes in cell-cell forces could result in magnified rotational moment when coupled to a longer cell-cell junction. Hence, a larger change in driving forces for rotation would be expected for cell pairs of longer contact length when they experience similar changes in cell-cell forces. In both types of experiments, changes in cell-cell forces for cell pairs of different areas were kept constant by using a constant ECM gap or a similar dose of Y27632 drug. As smaller cells were under lower intracellular tension, they would possibly experience a proportionately larger change in cell-cell forces (and hence, driving forces for rotation) when exposed to a similar-sized ECM gap or drug dose. This would account for a more significant effect of an ECM gap or Y27632 treatment on the rotation potential of smaller cells.

Although both ML7 and Y27632 were known to reduce intracellular contractility, the different results found could be explained by their action at different sites in treated cells. Comparing the effects of Y27632 and ML7 reported in previous studies, it was noted that Y27632 disrupts stress fibers (and hence cell stiffness) and focal adhesion in the interior of the cell while ML7 had been reported to have a more pronounced effect at the periphery of the cell [179]. Since focal adhesions and stress fibers are mainly concentrated at the cell periphery [52], it was speculated that only ML7 treatment would cause a significant decrease in forces opposing cell pair rotations. Similar to changes in driving forces in different areas, these changes in resisting forces were likely to be proportionately larger at smaller areas when the same ML7 dose was used. Hence, even though cell pairs with smaller areas or longer contact length could amplify the effect of ML7 treatment on the driving forces for rotation, a similar change in resisting forces would result in no net effect of ML7 treatment on rotation potential. At 2μM dose, rotation potential surprisingly increases under ML7 treatment. This finding support the proposal that the overall rotation potential observed in experiments were determined by an interplay between driving forces and resisting forces. In this case, the results from

2μM ML7 treatment could be explained if there is a larger decrease in resisting forces compared to the drop in driving forces in the treated cells.

### 4.3.9 Towards a more complex cell system: motility of 3-cell clusters

The experiments so far had established a general framework to explain the physical mechanism governing the rotation of confined cell pairs. However, cells do not exist in doublets in the body tissues and cell rotations are a rare occurrence *in vivo*. To verify the principles governing cell motility in more complex cell systems, the motility of a 3-cell cluster was tracked on a circular micropattern with an area of 2800 μm$^2$. Based on the principles governing cell pair rotations, cell motility could be expected to be minimized when the cells are distributed in a perfectly symmetrical manner as shown in Fig. 4.14.a. In such a configuration, the average contact lengths were at a minimum. Also, the cells were all identical in shape and were distributed in such a way that forces between them would likely balance themselves. The area of the cells was also kept approximately equal such that there were no cells of very small areas with high motility. Such highly mobile cells could be expected to generate a force imbalance that might destabilize the cell cluster. A configuration index, α was used to numerically characterize the configuration of the cells with respect to one another. By the definition of α, cells arranged in this perfectly symmetrical configuration will give a value of $\alpha = 1$. 3-cell clusters ($n = 73$) imaged over a 6 hour period at 10 mins interval and the different configurations adopted by these cell clusters were characterized by their α values. This was shown as a plot of square root count against α in Fig. 4.14.b. The square root transformation in the plot provided a clearer picture of the distribution of the cell clusters with low α since most of the clusters adopt configurations at high α values. The results showed that cell clusters tend to adopt symmetrical configurations and hence, this configuration could be regarded as the most stable one, consistent with predictions using the principles from cell pair rotations. This suggested that these principles might extend beyond rotational motion in 2-cell systems to provide some insights into the general motility of cells in tissue systems.

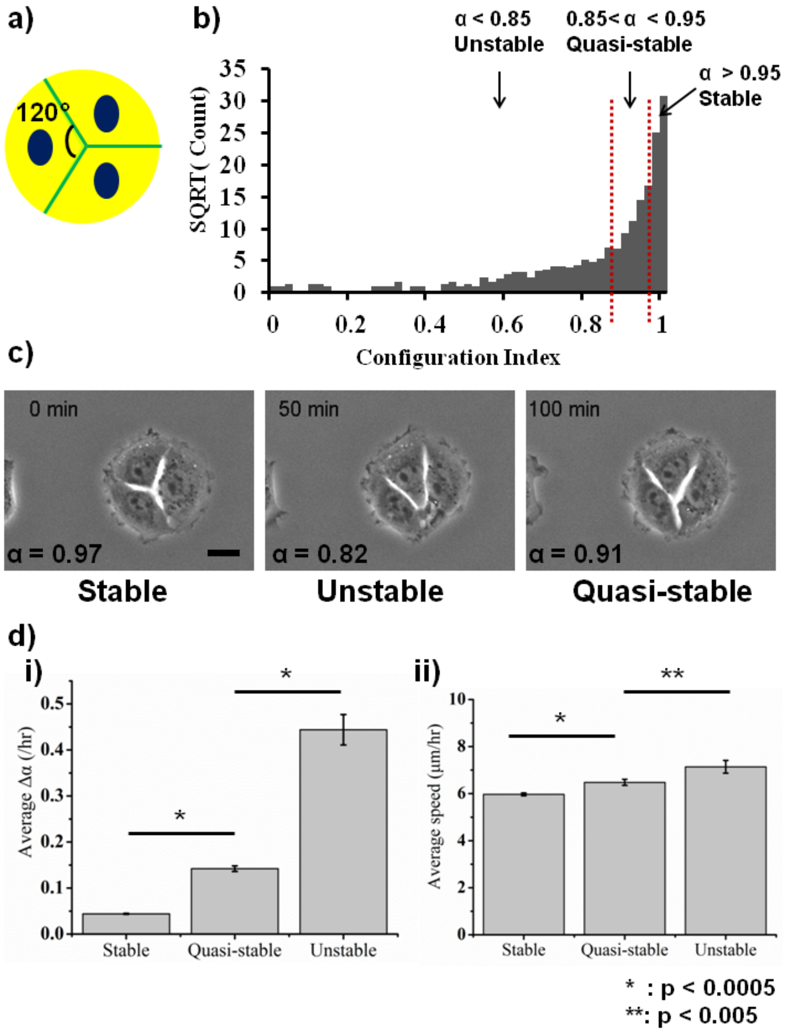

**Fig. 4.14.** Motility of 3-cell clusters on circular micropattern. a) Schematic of perfectly symmetrical distribution of cells. Nuclei are represented by dark blue ovals, cell-cell contacts by green lines, cell body is shown in yellow. b) Distribution of cell clusters (n =73) with various configuration index. Decay in square root count with α used to categorize cell clusters into groups. c) Time-lapse phase images of 3-cell clusters on micropatterns. Cell arrangement used to categorize cell clusters into groups. (d) Average (i) $\Delta\alpha$ and (ii) translational speed for cell clusters in each of the three groups. Scale bar depicts 20 μm. Error bar depict S.E. statistics.

Based on how the plot decays with α (see Fig. 4.14.b.) and how the cells were observed to be arranged under phase imaging (see Fig. 4.14.c), the cell clusters were broadly categorized into three groups. The stable group represented cell clusters with α in the region $\alpha > 0.95$ where the decay in the graph was very steep and the cells were arranged close to the symmetrical configuration seen in Fig. 3.14.a. In this group, each cell occupied a sector close to 120° in the circle. The quasi-stable group represented cell clusters with α in the region $0.85 > \alpha > 0.95$ where the decay in the graph was less steep and one of the cell tend to occupy a 180° sector leaving the other two cells to share the remaining sector in the circle. The unstable group represented cell clusters with α in the region $\alpha < 0.85$ where the decay in the graph was modest. In this group, one of the cells extended protrusions into the cell-cell junction of the other two cells, resulting in a clear change in neighbor relationship for these two cells. This is a classical cellular motion seen in cell intercalation which is one of the most important cell rearrangement processes *in vivo*. The motility of cell clusters in each of these three groups was further examined by calculating the average Δα and the average translational speed of the cell as shown in Fig. 4.14.d. Δα is defined as the change in the α value between two adjacent time points and translational speed was calculated by measuring the distance moved by the center of the nucleus of each cell over time. The results showed clear distinction in motility between the three groups where the stable group experience a low Δα and a low average speed of 0.04 /hr and 5.97 μm/hr respectively. The quasi-stable group represented a transitional configuration between the stable and unstable group with a moderate Δα of 0.16 /hr and a moderate speed of 6.55 μm/hr. The unstable group undergoes similar movement and rearrangement in cell position as cell intercalation that had been reported to be observed in physiological tissues. This movement and rearrangement once initiated was observed to be highly mobile with high Δα and high translational speed of 0.48 /hr and 7.08 μm/hr respectively. Cell clusters in this group was observed to either return back to a stable configuration via the quasi-stable group (see. Fig. 4.14.b.) or the intercalating cell could go all the way through the cell-cell junction of the other two cells (results not shown). Force imbalance had been reportedly used in computational models to recreate conditions for cell rearrangement but this result showed for the first time in experiments that this mechanical instability is sufficient to drive intercalating motion once it is initiated.

## 4.4 Conclusions

In this chapter, some physical principles governing cell motility of 2- and 3- cell systems had been elucidated and a force-mediated mechanism is proposed. For cell pairs confined in bow-tie shaped patterns, the coupling between cell-cell forces and the contact length could possibly generate a net rotational moment in the cell pair that could be the origin of the driving force behind cell pair rotations. The single cell area could also affect cell-cell forces in the cell pair via changes in cell contractility. More importantly, a change in focal adhesion density and cell stiffness with cell area could account for the resisting force against cell pair rotations. Cell shape symmetry was also an important factor which could determine the distribution of cell-ECM traction forces and consequently the distribution of cell-cell forces. Thus, cell shape could be a crucial determinant of the biased cell pair rotations. The presence or absence of an ECM gap and the response of cell pairs under drug treatment fits into this framework where interplay between driving and resisting forces determines the overall observed rotation potential.

To provide further insights into the general motility of cells in tissue systems, the applicability of these principles in a 3-cell system was investigated on circular patterns. The results showed that maximum stability of the 3-cell system was obtained when the cells were arranged in a symmetrical configuration. This result is consistent with the principles elucidated in cell pair systems where the average contact lengths of cells in such a symmetrical configuration were at a minimum. Also, the cells were all identical in shape and were distributed in such a way that forces between them would likely balance themselves. The area of the cells was also kept approximately equal such that there was no cells of very small areas with high motility. These results are summarized in Table 4.1.

**Table 4.1.** Summary of experimental observations in Chapter 4.

| Experimental parameter | Cell motility | Proposed mechanism |
|---|---|---|
| Cell-cell contact length | Increases with contact length | Coupled to cell-cell forces to generate rotational moment |
| Single cell area | Increases with area at large cell area | Involved in focal adhesion density and possibly cell stiffness which may be the origin of resisting forces against rotation |
| Shape asymmetry | No effect | Generate force imbalance resulting in rotational bias |
| ECM gap | Decrease amplified with small cell area and long contact lengths | Illustrates interplay between driving and resisting forces of rotation |
| Y27632 treatment | Decrease amplified with small cell area and long contact lengths | Illustrates interplay between driving and resisting forces of rotation |
| ML7 treatment | No effect at 1 µM dose,<br>Increases at 2 µM dose | Illustrates interplay between driving and resisting forces of rotation |
| 3-cell cluster | Minimized with symmetrical configurations | Consistent with proposed mechanism of 2-cell system |

# Chapter 5

# Actomyosin-mediated Contraction Dynamics in Cellular Rings

## 5.1 Introduction

In this chapter, the emphasis would be placed on epithelial void closure mediated by actomyosin contraction-based mechanism. Apart from its importance in the re-epithelialization of damaged epithelium, contractions mediated by force-generating actomyosin rings appears to be a universally observed behavior in dynamical systems of various cellular scales ranging from cleavage furrow constriction in cell division, single cell wound healing, extrusion of apoptotic cells to developmental processes such as dorsal closure in *Drosophila* morphogenesis. Due to the active role played by actomyosin ring contractions in so many different biological contexts, a good understanding of the contraction dynamics of actomyosin rings could be highly valuable.

In actomyosin contraction-based void closure, molecular mechanism governing its dynamics had been substantially studied. In a key experiment performed on Caco-2 cells about a decade ago using a variety of small GTPase inhibitors, a two stage process was used to described how small voids in epithelial sheets were closed by actomyosin contraction mechanisms [180]. An initial localized Rho-dependent assembly of actin and myosin II in a ring around the void was proposed to be followed by a MLCK-dependent contraction of the actomyosin ring. In order for the contractile ring to be formed, cells and their intracellular force-generating machineries must be joined in a continuous network at the cell edge lining the void region. To achieve this, both tight junctions [181] and E-cadherin mediated adherent junctions [182] have been implicated in the proper functioning of the actomyosin ring.

On the other hand, the physical rules dictating void closure by actomyosin-based contractions is poorly understood. Available literatures were focused on global void geometries and little work had been done to probe the effect of individual cell geometry. Even for studies done on global void geometry, the results obtained might be confounded by the rearrangement and proliferation of cells that were not directly involved in the formation of the actomyosin ring. For example, cells up to 10 cell rows back from the void could respond to the presence of a void in the cell layer. Rearrangement of cells had been observed in both epithelial sealing by cell crawling and actomyosin contraction where cells near the void region frequently exchanges position and neighbor relationships with one another [183]. Cell proliferation is also thought to be important for the prompt resealing of epithelial void especially if the void size is large. When a sizeable number of cells are removed from the epithelium by wounding, cells must be initiated to proliferate upon void formation in order to replenish the cell loss. Quantification of cell proliferation after a void was introduced in a confluent primary respiratory epithelial cell layer showed that a significant increase in proliferation was observed in cells located as far as 320 µm away from the void. This proliferation increase was only restricted to the immediate area around the void [184] which could indicate a direct link to void formation.

In this chapter, an *in vitro* experimental system to study the dynamics of actomyosin ring contractions was introduced. Cell adhesive micropatterns were arranged in a ring configuration allowing the formation of a cellular ring comprising a single row of cells. In this way, actomyosin ring contractions to close the void at the center of the cellular ring could be studied without conflicting signals from other components of the cell layer which are unrelated to forces generated by constituent cells. For example, signals from cell proliferation and cell rearrangement could be excluded in a single-row cellular ring. Using this novel *in vitro* experimental system, the influence of both the geometrical parameters of individual cells as well as cell arrangement in the ring (global void geometry) on the contraction dynamics of actomyosin rings was investigated.

## 5.2 Materials and Methods

### 5.2.1 Cell seeding on micropatterned substrates

Array patterning of a series of micropattern in ring configuration was achieved using the photolithographic method as described in Chapter 3. EpH4 cells were cultured and prepared as described in Chapter 3. 1.5 ml of cell suspension with a cell density of 150,000 cells/ml were added to patterned coverslips in a 35 mm petri dish and incubated in standard cell culture conditions for 40 min. Cell were seeded at an increased density and incubated for a longer time compared to that in Chapter 3 as the micropatterns are now patterned at a higher density on the coverslip when they are arranged in ring configuration. After the incubation time has elapsed, the excess cells were rinsed off using serum-free DMEM medium supplemented with only 1% (v/v) penicillin/streptomycin. A common problem encountered when using this experimental system was that void closure in the cellular ring occurred at hugely different time points on different patterns in the array. Void closure typically occurred after all the cell-cell junctions were formed between well-spread cells in the ring. However, the rate of spreading was observed to be vastly different for cells on different patterns in the array and even between different cells on the same pattern. With 4 to 6 cells in each pattern, it was reasonable to expect void closure to occur at very different time points. To initiate void closure on demand (ie when most of the cellular rings were formed and the coverslip was ready for imaging), Y27632 ROCK inhibitor was added at a low concentration of 100 nM. As reported in the literature, Y27632 treatment blocked the assembly of actomyosin rings and prevented void closure [180]. Conversely, the drug encouraged cell spreading as cell contractility was reduced. Cells on micropattern were allowed to spread in serum-free medium spiked with Y27632 inhibitor for 8 hrs. This ensured that the cells spread fully on the micropattern and formed cellular rings. After 8 hrs, the serum-free medium was rinsed twice with complete medium to ensure a complete wash out of the Y27632 inhibitor. For verification of void closure mechanisms using small molecule inhibitors, complete medium containing 10 µM of Y27632 or 25 µM NSC23766 were added instead.

### 5.2.2 Immunofluorescence staining

The actomyosin system was allowed to assemble by incubating the cellular rings in complete medium for 30 mins after Y27632 washout. After which, cellular rings were washed twice with PBS to remove any serum residues. The rings were then fixed using 4% paraformaldehyde (Sigma) for 5 mins. Following fixation, the cellular rings were rinsed twice with PBS and then permeabilized with 0.5% Triton-X (Sigma) for another 5 minutes. The permeabilized cellular rings were thoroughly rinsed three times with PBS and incubated in a blocking buffer containing 1% BSA (Sigma) for 30 mins. After blocking, the cellular rings were incubated for 45 mins in a humid chamber with a primary rabbit antibody for phosphorylated myosin light chain (Cell Signaling) diluted 1:200 in blocking buffer. The humid chamber was made using petri dishes and kimwipes soaked with DI water. After that, the primary antibody was thoroughly washed off before the rings were incubated for 45 mins with Alexa Fluor 488-tagged anti-rabbit polyclonal antibody (Abcam) diluted 1:1000 in PBS. The secondary antibody was thoroughly rinsed off before the cellular rings were incubated for 20 mins with Alexa Fluor 594-tagged phalloidin (Invitrogen) diluted 1:40 in blocking buffer. The coverslips were then deposited on glass slides using 30 µl mounting solution and dried overnight at room temperature.

### 5.2.3 Image Acquisition

Time-lapse imaging of live cells on micropatterns was taken over 12 hrs at 5 mins time intervals using the BioStation IM-Q system. This long imaging period was to ensure that sufficient time was given for the assembly of the actomyosin ring and also for some of the partially formed cellular ring to be completed. Images were taken under using the in-built cooled CCD camera at 10X magnification. Instead of automated acquisition as was done in chapter 3. Cellular rings containing the correct number of cells were selected for imaging manually. This was because the probability of obtaining 4-6 cells correctly in the rings was very much lower than the probability of having paired cells required in Chapter 3. Immunofluorescently stained cellular rings were imaged using the BioStation IM-Q system under both 465-495 nm (blue) and 540-580 nm (green) excitations using the in-built cooled CCD camera at 40 X magnification.

### 5.2.4 Measurement of contraction rate in cellular ring

From raw images obtained from the BioStation IM-Q, patterns that did not contain the correct number of cells were immediately discarded. For the remaining patterns, only the series of images showing void closure in a stable cellular ring was used in the analysis of the contraction rate of the actomyosin ring. A stable cellular ring must satisfy the following 2 criteria: (1) the center of the void region should not be visibly shifted and (2) there should be no change in cell number lining the void as it closes. The size of the void in each of these images was then measured using the ImageJ software. Image enhancement using in-built functions such as ‘Despeckle’ and ‘Find Edge’ were used to locate the edges of the void clearly. The polygon selection tool was used to surround the void as accurately as possible and the area of the selection was measured. This measurement was repeated 3 times and the average value gave the approximate area of the void in that particular image. The rate of actomyosin-mediated contractions associated with the cellular rings could then be calculated from the difference between the void areas of two images taken at successive time points. Contractions rates lower than 10 $\mu m^2$/min were considered stationary and discarded. At least 25 cellular rings were analyzed for each type of pattern in this manner and their associated contraction rates and void areas were plotted as data points shown in Fig. 5.3 - Fig. 5.7. The data points from all the cellular rings analyzed were collated together for each type of pattern to generate an overall picture of the relationship between contraction rates and void areas. Void areas at each time point were then expressed as a fraction of the initial void area before void closure. Data obtain was found to be fairly noisy and outliers were removed using the modified Thompson tau method [185] to smoothen the data.

## 5.3 Results and Discussion

### 5.3.1 Cellular ring from a single row of cells

Five trapezium shaped micropatterns arranged in a ring configuration created a pentagon-shaped region devoid of ECM at the center of the ring. This region resembled a void formed in an epithelial cell sheet and the *in vitro* behavior of cells lining this ECM-free region could be investigated conveniently. EpH4 cells seeded at high density on this ring of micropatterns formed a confluent pentagon-shaped monolayer with a cell-free region at the center as shown in Fig. 5.1.a. Not surprisingly, the inner edges of the cells lining this cell-free region were observed to form a smooth ring around the void which contracts rapidly and closes the void within 1 hour. Under phase contrast microscopy, this contracting ring formed by the cell edges appeared to be highly tense and lamellipodia activity were absent in the void. This observed behavior was highly reminiscent of how cells move to close openings in the epithelium via an actomyosin-mediated contraction mechanism, consistent with reports that claimed that this mechanism would be preferred to the lamellipodia-mediated migration mechanism for epithelial voids without an underlying ECM layer [41]. When cells were seeded on ring micropatterns at low density, it was observed that a single row of 5 cells arranged in a pentagon shaped ring could be formed. This single row cellular ring could close the void at the ring center in the same manner as confluent cell sheets (see Fig. 5.1.b.). Although epithelial void closure involving several rows of cells in the void vicinity was thought to be closer to the situation *in vivo* [182], examining actomyosin contractions in a single row of cells could potentially remove conflicting signals from cells shuffling towards and away from the void region.

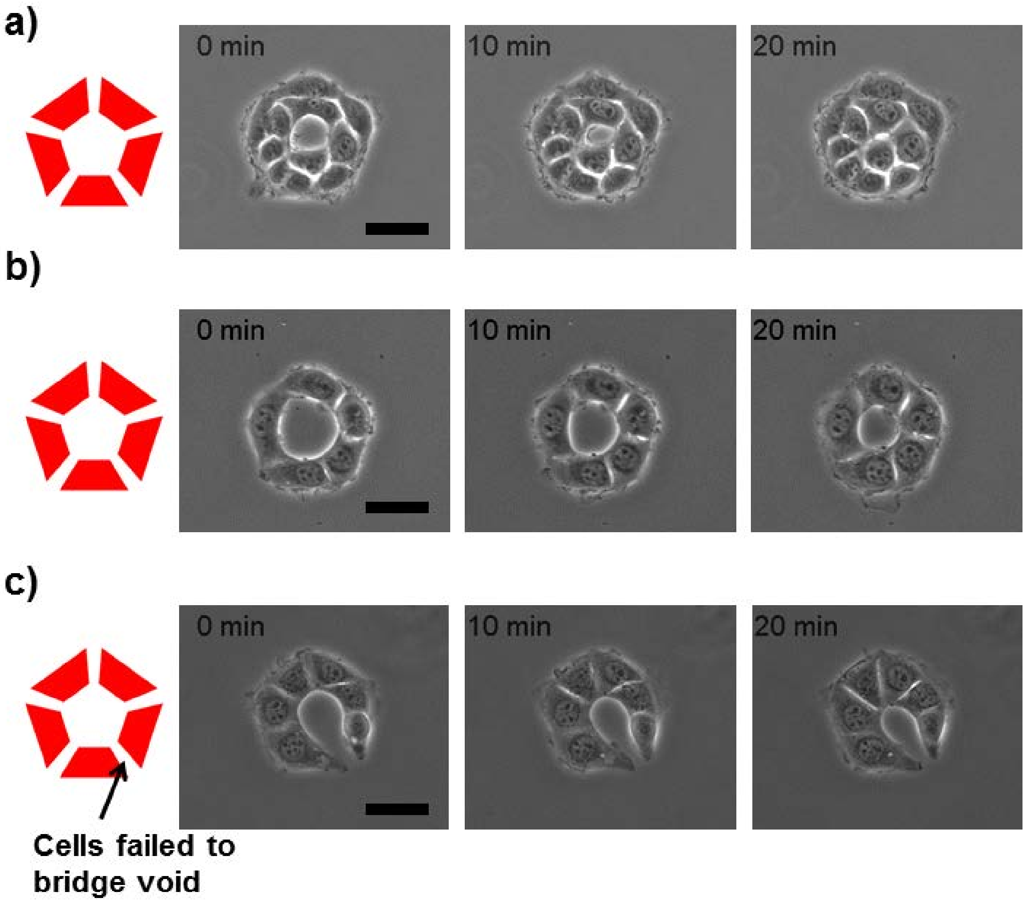

**Fig. 5.1.** Actomyosin-mediated contraction in different cellular configurations. a) Confluent monolayer with a cell-free region in the center. 0 min indicates the commencement of void closure. b) Single row cellular ring. c) Single row of cells in horseshoe-shaped configuration. Schematics of micropatterns used are shown on the left of phase images in red. Scale bars depict 50 µm.

Interestingly, it was also found that a row of cells arranged in a horseshoe-shape appeared to form a similar contractile ring at the inner edge of the ring as shown in Fig. 5.1.c. These horseshoe-shaped cellular clusters were formed when two adjacent cells did not bridge the gap between successive micropatterns in the ring. This result suggests that curvature could play an essential role in encouraging void closure in cell clusters and it is possible that the presence of a full ring of cells lining the void might not be a necessary condition.

Void closure in epithelial resealing is known to be driven by either cell crawling or actomyosin contraction mechanisms. Rac activation has been found to be vital for cell crawling [38] while the activation of the Rho-ROCK pathway is known to be a pre-requisite for actomyosin contraction [180]. To verify that void closure on these single row cellular rings were mediated by actomyosin contractility and not cell crawling, singe row cellular rings were treated with small molecule inhibitors Y27632 and NSC23766 for inhibition of ROCK and Rac1 respectively. An optimal drug dose of 10 µM and 25 µM was used for Y27632 and NSC23766 respectively in these experiments. At higher dosage, the cellular rings were observed to be highly unstable where cell-cell contacts tend to be easily disrupted during the course of the time-lapse imaging. Inhibition of ROCK by Y27632 treatment was found to prevent void closure over a long period of time (> 120 min), well over the typical time period (< 60 min) required for untreated rings to close (see. Fig 5.2.a.i). On the other hand, inhibition of Rac1 by NSC23766 continued to allow void closure in the cellular rings to proceed as shown in Fig, 5.2.a.ii. To further show that actin and myosin molecules were key players in this Rho-dependent closure of cellular rings, immunofluorescence experiments were performed as shown in Fig. 5.2.b. As the void size was found to be smaller than the ECM-free region at the center of the ring of patterns, this cellular ring was deduced to be fixed and stained while in the process of void closure. Actin filaments and phosphorylated myosin were found to be co-localized at the inner edge of the cellular ring as expected when void closure is driven by the actomyosin contraction mechanism. Taken together, these results supported the claim that void closures in these single row cellular rings were mediated by actomyosin contractility.

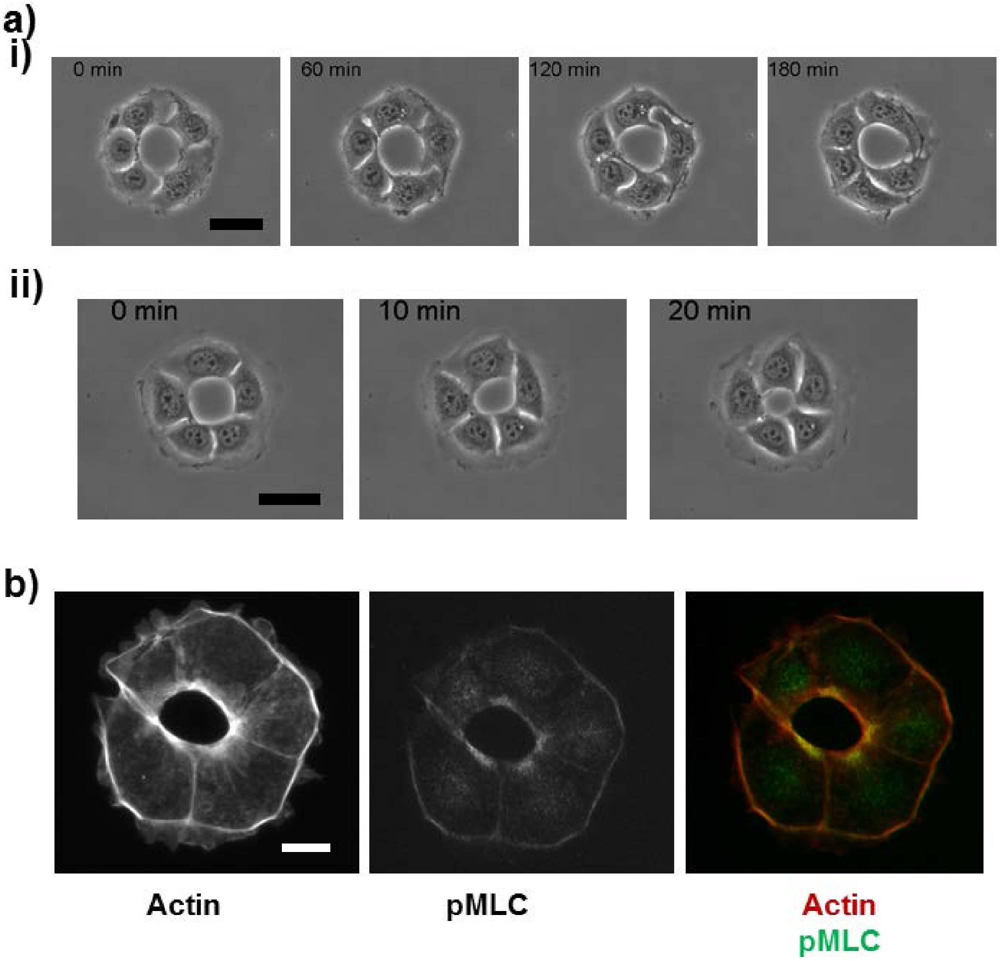

**Fig. 5.2.** Verification of void closure mechanism. a) Treatment of cellular ring with small molecule inhibitors. (i) Treatment with 10 µM Y27632. No void closure even after 120mins from establishment of a stable cellular ring. Cell migration after 180mins disrupts the cellular ring. (ii) Treatment with 25 µM NSC23766. Void closure continued to be observed within 60 min. b) Immunofluorescence staining for actin (red) and phosphorylated myosin light chain (green) on single row cellular ring. Black and white scale bars depict 50 µm.

Before performing quantitative experiments on single-row cellular rings, a general understanding of the contraction dynamics associate with these rings were first obtained.

Changes in the area of the cell-free region in the cellular rings (termed ‘void’ from now on) was first measured over time and at least two prominent behavior of these cellular rings was found to have significant effect on contraction dynamics. Firstly, an off-centering of void was sometimes observed in the cellular ring as shown in Fig. 5.3.a.i. This could be explained by heterogeneity in intracellular contractility of constituent cells in the cellular rings which could manifest as localized differences in the contraction rate. As cellular rings were made up of only a small number of cells, these localized differences were significant and different parts of the cellular ring might contract at different rates. Conversely, for void closure in confluent cell sheets where a large number of cells were involved, this effect did not appear to be observed. Cellular rings with an off-centered void would also be expected to have an uneven distribution of tension as some cells in the ring would be stretched to a larger degree compared to other cells. In the example in Fig. 5.3.a.i, cells making up the top of the cellular ring were clearly stretched more compared to cells at the bottom of the ring at the 25 min time point. A redistribution of tension in the ring would move the void back to the center of the ring again as shown at the 50 min time point. When the void was being repositioned, contraction dynamics were adversely affected. A plot of void area over time clearly showed that the void size remained constant from 35 min mark to the 50 min mark (see Fig. 5.3.a.ii). This time period coincides with the repositioning of the void. Before and after this repositioning, the cellular ring was observed to close the void normally. This result strongly suggested that repositioning of the void possibly due to a redistribution of stress in the cellular ring could have a strong influence on contraction dynamics. Hence, for quantitative studies, contraction rates in the cellular rings were only measured when the void position did not vary significantly.

The second behavior of cellular rings that could have significant impact on contraction dynamics was a change in the number of cells lining the void region. For void closure in confluent cell sheets, the number of cells lining the void tends to decrease as the void closes and this behavior is facilitated by the shuffling of cells towards and away from the void region [184]. In single row cellular rings, exclusion of cells from the immediate vicinity of the void could still occur as shown in Fig. 5.3.b.i. at the 250 min and 450 min time point. However, cell insertion were also frequently observed as shown at the 350 min and 550 min time points, especially in cellular rings with a few cells and large void sizes that would take a long time to close if it were to close at all. In the example given in Fig. 5.2.b, the cellular ring consisting of 6 cells and had a void size of 3500 $\mu m^2$ did not close even after 800 min. A plot of void area over time clearly showed a relaxation in the cellular ring whenever there were changes in the cell number lining the void region (see Fig. 5.3.b.ii). Again, this could possibly be due to the small number of cells lining the void where a change in the cell number could have significant effect. Hence, for quantitative studies, contraction rates were only measured when the number of cells lining the void remained constant. In this way, the influence of cell number on contraction dynamics associated with the cellular rings could also be probed systematically.

For a quantitative study of the actomyosin-mediated contraction dynamics associated with these cellular rings, an average contraction rate was calculated. Contraction rates at different stages of void closure (expressed as a fraction of initial void area) were also plotted for a visual representation of how contraction rate changes with void closure. For cellular rings associated with high contractility, the data points would populate higher easy identification of this trend (as shown in Fig. 5.4.a) and by no means represented the exact rates of changes in the graph. From the results obtained, contraction rates were

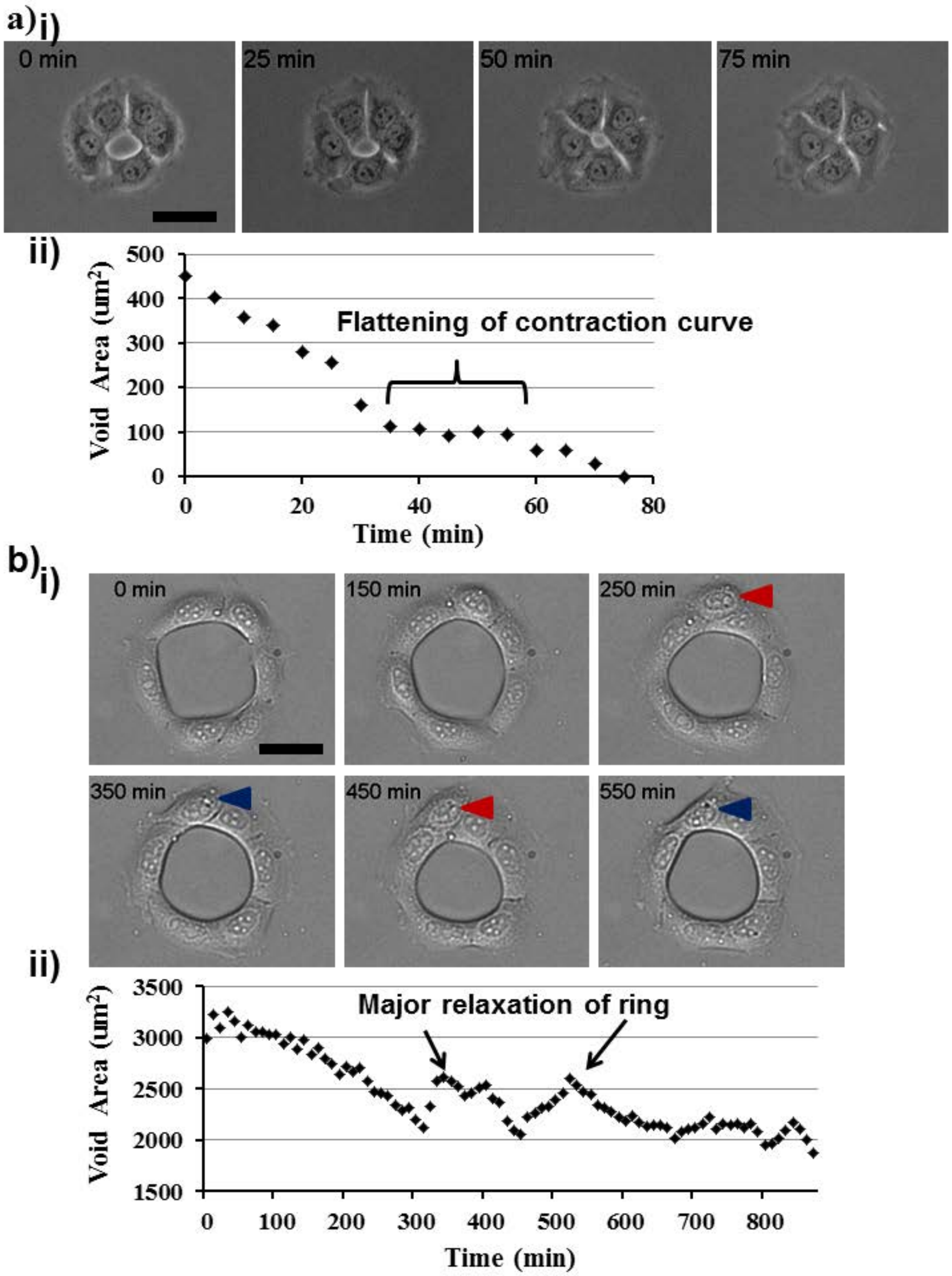

**Fig. 5.3.** Behavior of cellular ring affecting contraction dynamics. a) Effect of void repositioning on contraction dynamics. (i) Phase images of void repositioning. (ii) Plot of void area against time showing a flattening of the contraction curve as the void was repositioned. b) Effect of cell insertion and exclusion on contraction dynamics. (i) Phase images at time = 0 min and time = 150 min to time = 550 min where insertion (blue arrow) and exclusion (red arrow) was taking place. (ii) Plot of void area against time showing relaxation of cellular ring when number of cells lining the void changes. Scale bars depict 50 μm.

observed to decrease as the void was closed. The average cell sizes of constituent cells in the cellular rings were also found to increase in tandem with void closure. Taken together, a plot of contraction rates against average cell areas showed that the contraction rate was inversely correlated with average cell areas (see Fig. 5.4.b). This effect of cell area on contraction dynamics appeared to be observed uniquely in single row cellular ring. In confluent cell sheets with large number of cells lining the void region, changes in cell size as the void closes are likely to be small and may not have any significant effect on contraction dynamics.

To further probe the effect of cell area on contraction dynamics associated with cellular rings, the initial area of constituent cells in this ring could be varied conveniently by changing the size of the trapezium micropatterns (see Fig. 5.4.c). Void area could also be varied conveniently with small shifts in the angle between each trapezium micropattern. Square-shaped rings could be designed by using four micropatterns instead of five arranged at right angle to each other. These square-shaped rings were observed to be able to close the void in the center of the ring in a similar manner to their pentagon-shaped counterparts (see Fig. 5.4.d.i). As cells were randomly seeded on the micropatterns, the number of cells in the cellular ring could vary. With the seeding density used, these cellular rings were frequently observed to be made up of four or five cells. Cellular rings made up of only four cells were observed to close the void in the ring in a similar manner as 5-cell rings (see Fig. 5.4.d.ii). Hence, a systematic study of the effect of cell number on contraction dynamics was also possible. Different micropattern designs were named based on these four parameters. For example, [G1600 A1000 5-cell Pentagon] patterns represented micropatterns designed for 5-cell pentagon–shaped cellular rings of void area 1600 μm$^2$ with initial cell area of 1000 μm$^2$.

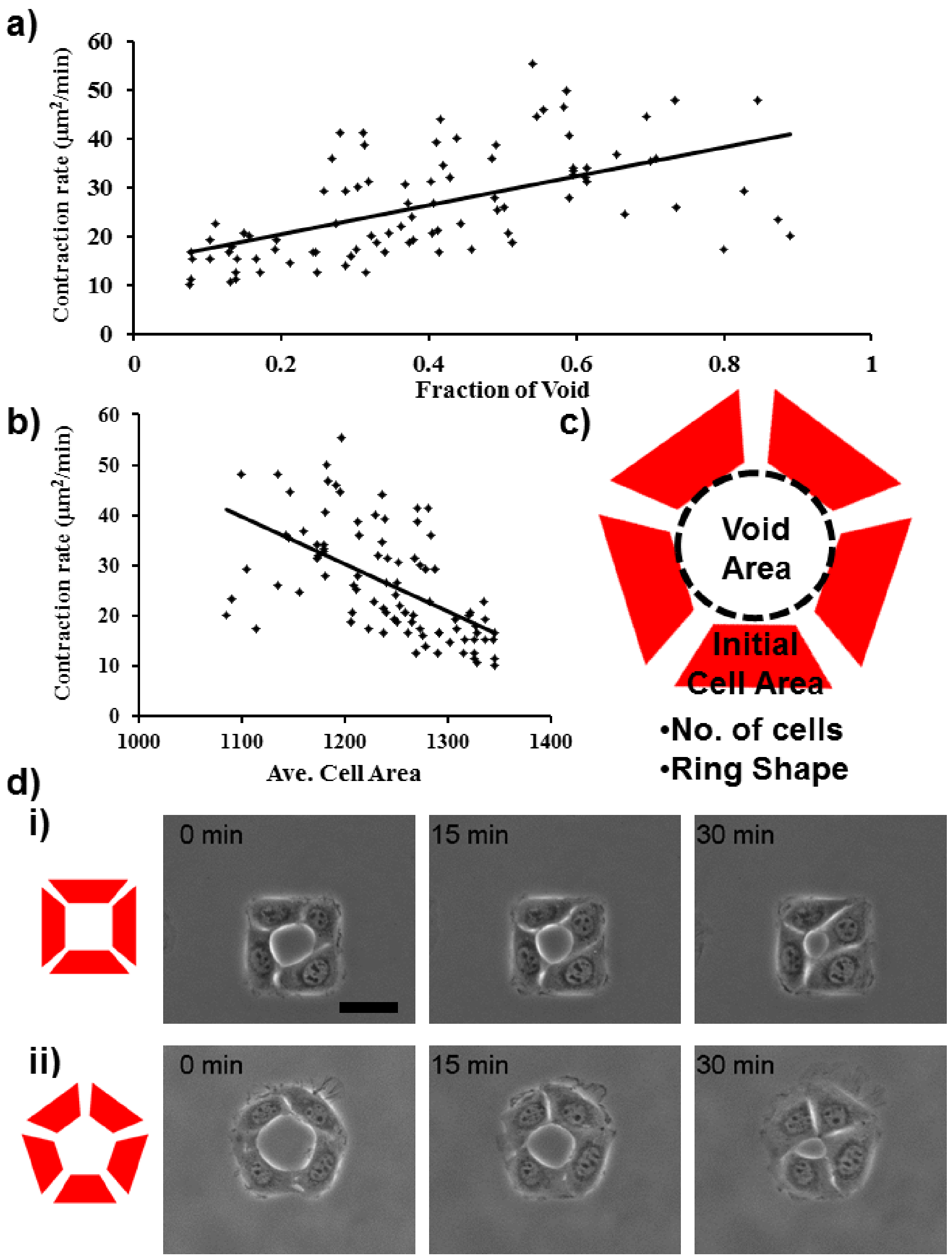

**Fig. 5.4.** Contraction dynamics associated with cellular rings a) Plot showing contraction rates with fractional area of initial void. Linear fit for visualization purposes only. b) Plot showing how contraction rates changes with average cell area of constituent cells in the cellular rings. c) Possible physical parameters affecting contraction dynamics in cellular rings that could be varied with micropatterning. d) Phase images showing (i) square-shaped cellular ring and (ii) pentagon-shaped cellular ring with 4 cells. Schematics of micropatterns used are shown on the left of phase images in red. Scale bar depicts 50 μm.

### 5.3.2 Effect of initial cell size and cell number on contraction dynamics

Void closure observed in single row cellular rings with a small number of cells lining the void region provide a unique opportunity to examine the effect of individual cells on global contraction dynamics associated with these cellular rings. Physical parameters such as the initial area of constituent cells in a cellular ring could be varied conveniently using micropatterning. A plot of contraction rates against average cell areas shown in Fig. 5.4.b had given a first indication that average cell area could significantly impact contraction dynamics associated with these cellular rings. To probe the effect of initial cell area instead, [G1600 5-cell Pentagon] cellular rings made up of cells with initial area of 800 µm$^2$ and 1000 µm$^2$ before void closure were created. Their contraction rates and average cell areas were measured (number of ring patterns analysed, $n_{A800} = 36$, $n_{A1000} = 28$) as the void was closed. An average value of the cell areas throughout the whole contraction process was calculated and this was used to represent the area regime where the contraction occurs. Cell areas generally varied within 200 µm$^2$ of this average value. As expected, contraction in A800 rings occurred at a lower area regime averaged at 976 µm$^2$ (S.E.±6) compared to that of A1000 rings at 1241 µm$^2$ (S.E.±7) as shown in Fig. 5.5.a. At the same time, contractility in the cellular rings characterized by average contraction rate were observed to be significantly lower in A800 rings at 22.0 µm$^2$/min (S.E.±0.7) as compared with A1000 rings at 26.4 µm$^2$/min (S.E.±1.2) as shown in Fig. 5.5.b. Furthermore, in a plot of contraction rate against void closure, the A1000 line characterizing changes in contraction rate with void closure clearly lie above the A800 line in Fig. 5.5.c. These results strongly suggested that general contraction rate in cellular ring increases with an increase in the initial area of constituent cells in the ring.

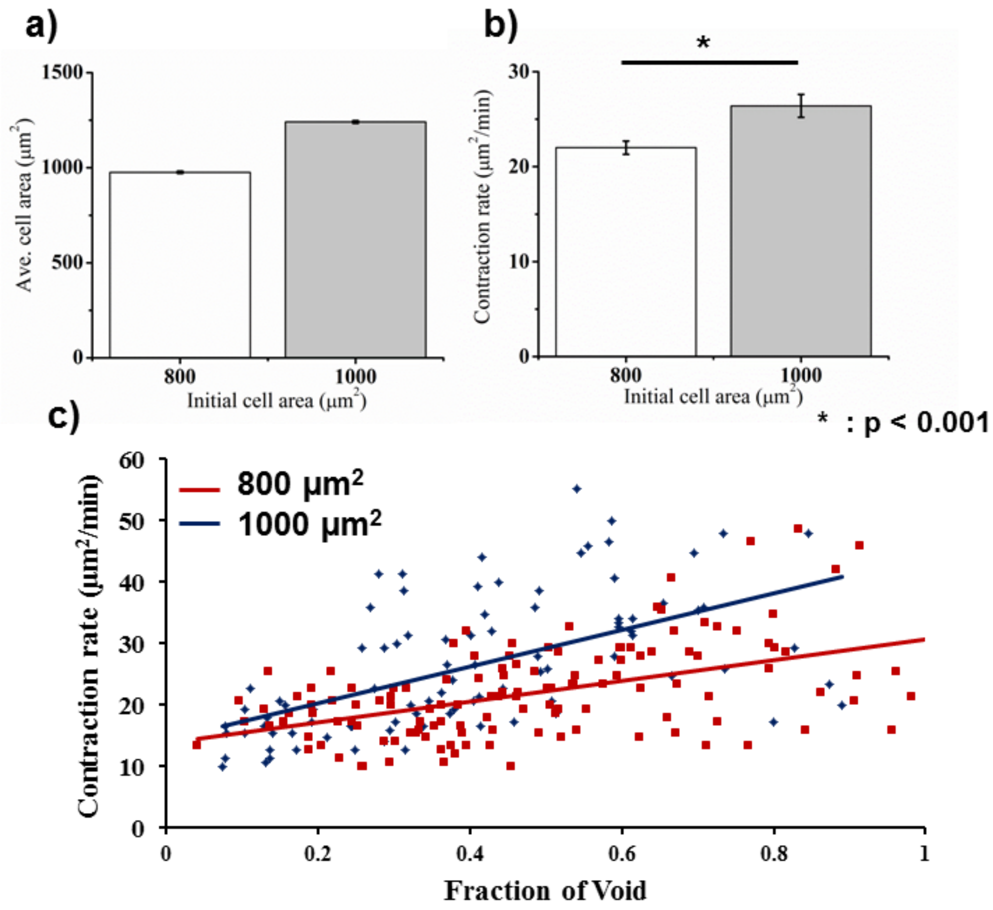

**Fig. 5.5.** Effect of initial cell area on contraction dynamics. a) Plot showing average cell area over the whole contraction process for different initial cell areas. b) Plot showing average contraction rates for different initial cell areas. c) Plot showing contraction rates with void closure. Data for rings with initial cell area of 800 $\mu m^2$ ($n_{A800} = 36$) depicted in red and area of 1000 $\mu m^2$ ($n_{A1000} = 28$) depicted in blue. Linear fit for visualization purposes only. Error bars depict S.E. statistics.

Taken together with results shown in Fig 5.4.b, changes in cell area was observed to have two opposing effect on contraction dynamics. An increasing average cell area could decrease contraction rate as the contraction proceeds but a large initial cell area encourages higher contraction rate in general. Contraction in these cellular rings could be driven by the assembly and contraction of actomyosin rings lining the void region. However, the identity of any resisting forces that may prevent void closure had not been well described. Intracellular contractility increased with cell size [172] and was similarly mediated by actomyosin tension. These intracellular forces were known to act towards the interior of the cell and could oppose further stretching of the cells with void closure. Cell stiffness was also positively correlated with cell size [173] which may make cellular rings increasingly more difficult to be stretched over the void region. These factors could act as a resisting force to actomyosin contraction and might account for the decreasing contraction rate observed when cell area increases with void closure. However, the degree at which each of these factors affect contraction dynamics may vary with the initial cell area. In fact, the results obtained suggested that these factors may affect contraction dynamics more significantly when initial cell areas are smaller. It had been previously reported that competition for G-actin could regulate the formation and development of various F-actin structures in fission yeast [186]. At small initial cell areas, levels of intracellular contractility and cell stiffness are low. As average cell area increases, these cellular properties could possibly increase with ease, mediated by an abundant pool of free actin, myosin and other required molecular resources. However, at large initial cell areas, most of these molecular resources were already involved the formation of stress fibers, cortical actin cables or cross-linked to these cytoskeletal networks and available free molecules may be scarce. Hence, it is conceivable that changes to intracellular contractility levels and cell stiffness may occurred at lower rates, leading to lower opposing forces to contraction and the higher contraction rates observed in general.

To investigate the effect of constituent cell number on contraction dynamics associated with the cellular rings, [G1600 A1000 5-cell Pentagon] patterns with five cells ($n_{5\text{-cell}} = 28$ and [G1600 A800 5-cell Pentagon] patterns with four cells ($n_{4\text{-cell}} = 32$) were investigated. This was because when four cells were seeded on patterns designed for five, the initial cell area would be larger than expected. In the cellular rings created, contraction in 4-cell rings occurred at an area regime averaged at 1236 $\mu m^2$ (S.E.±8) which is comparable to the regime of 5-cell rings at 1241 $\mu m^2$ (S.E.±7) as shown in Fig. 5.6.a. This result showed that contraction in both 4 and 5 cell rings occurred in the same area regime and the effect of initial cell area would not affect the general contraction rates in these rings. Interestingly, average contraction rate were observed to be significantly lower in 4-cell rings at 20.6 $\mu m^2$/min (S.E.±0.7) compared with 5-cell rings at 26.4 $\mu m^2$/min (S.E.±1.2) as shown in Fig. 5.6.b. At the same time, in a plot of contraction rate against void closure, the 5-cell ring line clearly lies above the 4-cell ring line in Fig. 5.6.c. These results strongly suggested that general contraction rate in cellular ring increases with the constituent number of cells in the ring. As the void in a 5-cell ring closes, changes in the area of constituent cells were distributed among a larger number of cells compared to 4-cell rings. In this way, 4-cell rings experienced a larger change in the average cell area compared to 5 cell rings for the same change in void area. For example, a 200 $\mu m^2$ decrease in void area would result in a 40 $\mu m^2$ increase in the average cell area of 5-cell rings but a 50 $\mu m^2$ change for 4-cell rings. As a larger increase in average cell area would result in a more significant drop in contraction rate, it was clear that contraction in 4-cell rings would occur at a lower rate in general.

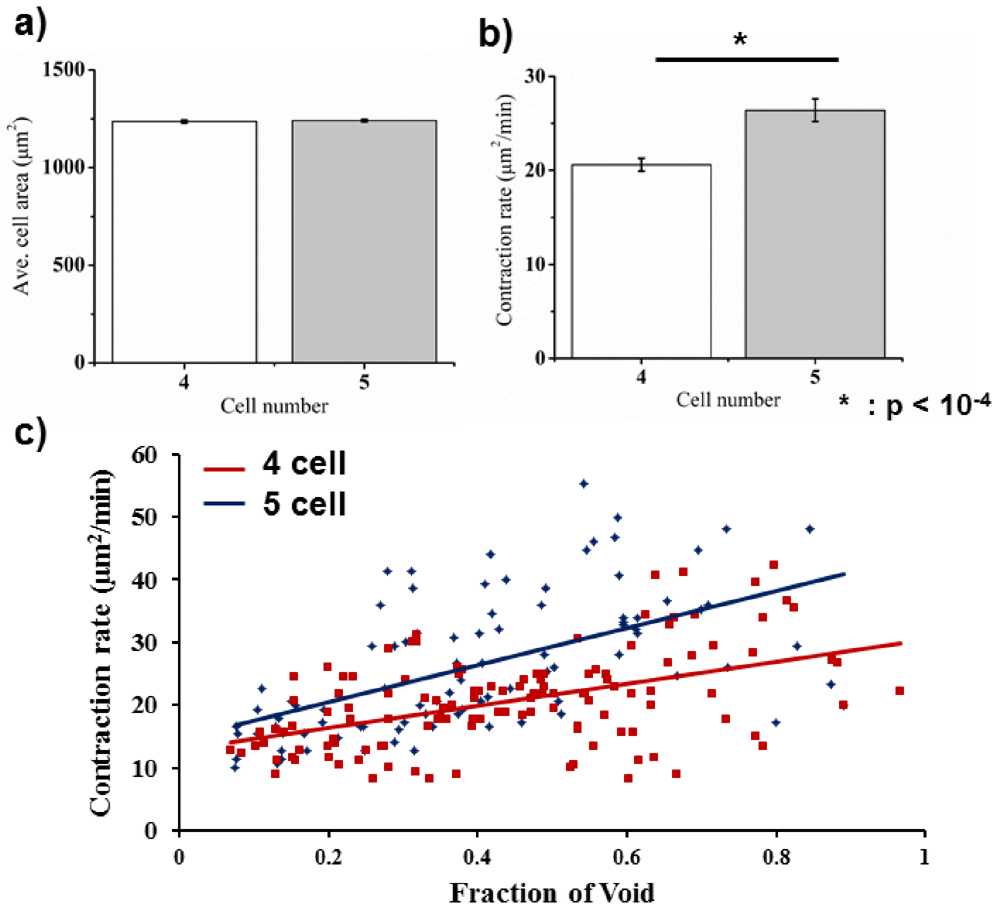

**Fig. 5.6.** Effect of constituent cell number on contraction dynamics. a) Plot showing average cell area over the whole contraction process for different cell numbers. b) Plot showing average contraction rates for different cell numbers. c) Graph showing contraction rates with void closure. Data for 4-cell ring ($n_{5\text{-cell}} = 32$) depicted in red and 5-cell ring ($n_{5\text{-cell}} = 28$) are depicted in blue. Linear fit for visualization purposes only. Error bars depict S.E. statistics.

### 5.3.3 Effect of global void geometry on contraction dynamics

Physical parameter of individual cells that made up cellular rings had been shown to exert a considerable influence on global contraction dynamics associated with these cellular rings. While global void geometry had already been investigated in several studies [41,187], these studies were conducted in confluent cell sheets with possible conflicting signals from cells located a few cellular rows away from the void region. Also, individual cell size and cell number were not kept constant which might influence the obtained results. Here, the influence of void size and shape on contraction dynamics was examined under highly controlled physical conditions. Contraction dynamics associated with [A1000 5-cell Pentagon] cellular rings with void area of 1000 µm$^2$ ($n_{G1000}$= 33), 1600 µm$^2$ ($n_{G1600}$= 28) and 2200 µm$^2$ ($n_{G2200}$= 26) respectively were compared in experiments. Contraction in G1000 rings occurred at an area regime averaged at 1192 µm$^2$ (S.E.±4) which is slightly lower than the regime of G1600 rings at 1241 µm$^2$ (S.E.±7). At the same time, the area regime where contraction occurred in G1600 rings was also slightly lower compared to the regime associated with G2200 rings at 1318 µm$^2$ (S.E.±7). These results were shown in Fig. 5.7.a. Average contraction rate were observed to be higher in G1600 rings at 26.4 µm$^2$/min (S.E.±1.2) compared with G1000 rings at 23.4 µm$^2$/min (S.E.±0.8) while similar contraction rate of 26.5 µm$^2$/min (S.E.±0.9) was found in G2200 rings (see Fig. 5.7.b.). Similar trends were also observed in a plot of contraction rate against void closure as shown in Fig. 5.7.c. Here, although there may be some difference in the initial cell area, it was considered small compared to that observed in Fig. 5.5 and its influence on contraction rate may be considered to be small compared to the observed differences in contraction rate. Hence, these results showed that a larger void area increases the average contraction rate only at low initial void areas.

A previous study claimed that the constriction rate of the single cell cortical contractile ring (which was similarly powered by actomyosin forces) during cytokinesis varied proportionately to initial cell size [188]. The authors proposed a model which described contractile rings as a collection of smaller contractile unit of fixed size and contractile potential. A larger ring would therefore contain more of these units, allowing a faster rate of contraction. The results obtained from the void size experiments suggested that this model could also be possibly applicable to actomyosin-mediated closure of epithelial voids. However, the results also showed that this dependency of contraction rate on void size was only restricted to low void sizes. Possibly, this could be due to limited availability of these contractile units due to the small number of cells in single row cellular rings.

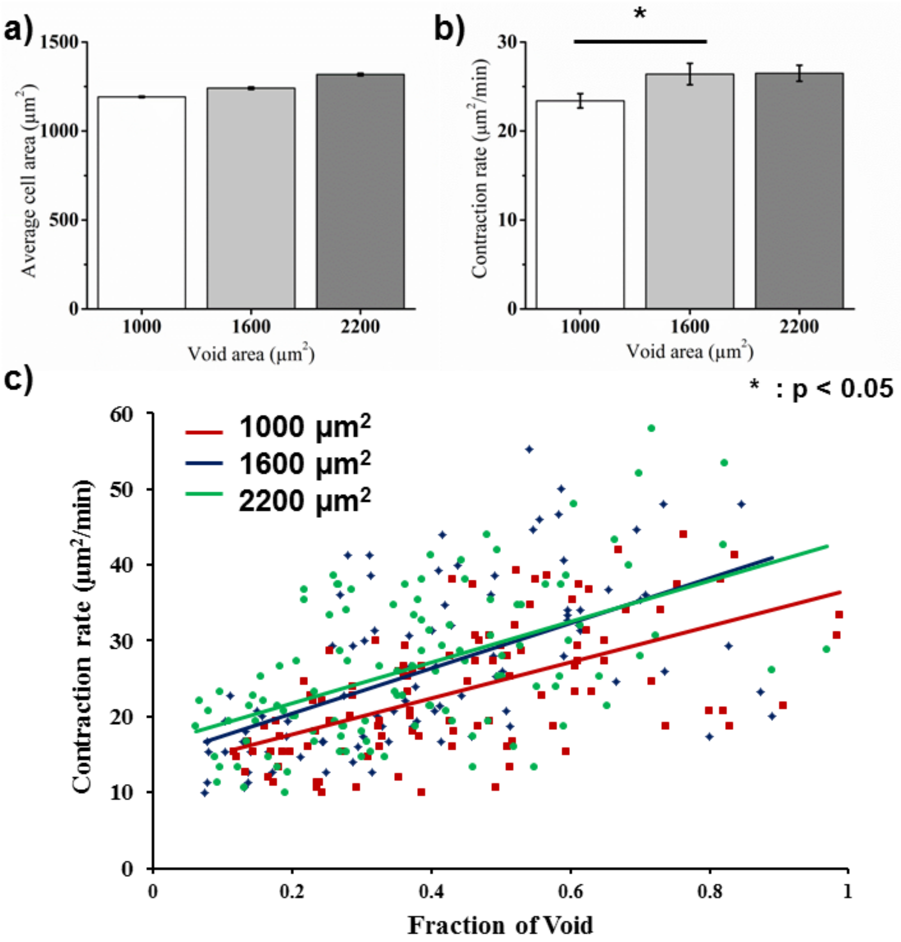

**Fig. 5.7.** Effect of void size on contraction dynamics. a) Plot showing average cell area over the whole contraction process for different void sizes. b) Plot showing average contraction rates for different void sizes. c) Plot showing contraction rates with void closure. Data for G1000 rings ($n_{G1000}$= 33) depicted in red, G1600 rings ($n_{G1600}$= 28) depicted in blue and G2200 rings ($n_{G2200}$= 26) depicted in green. Linear fit for visualization purposes only. Error bars depict S.E. statistics.

To investigate the effect of initial void shape on contraction dynamics, the contractility associated with [G1600 A800 5-cell Pentagon] cellular rings ($n_{pentagon}$ = 36) and [G1200 A800 4-cell Square] cellular rings ($n_{square}$ = 36) were characterized. Due to the arrangement of the micropatterns, square cellular rings were formed around square voids while pentagon cellular rings surrounded pentagon voids before void closure sets in. As the square rings were made up of only 4 micropatterns, geometry restrictions allowed a maximum initial cell area of 1200 μm$^2$ to be designed in these rings. Contraction in square rings occurred at an area regime averaged at 1097 μm$^2$ (S.E.±6) which was only slightly higher compared to the regime of pentagon rings at 976 μm$^2$ (S.E.±6) as shown in Fig. 5.8.a. An average contraction rate of 21.3 μm$^2$/min (S.E.±0.7) in square rings were observed to be comparable to pentagon rings at 22.0 μm$^2$/min (S.E.±0.7) (see Fig. 5.7.b.)

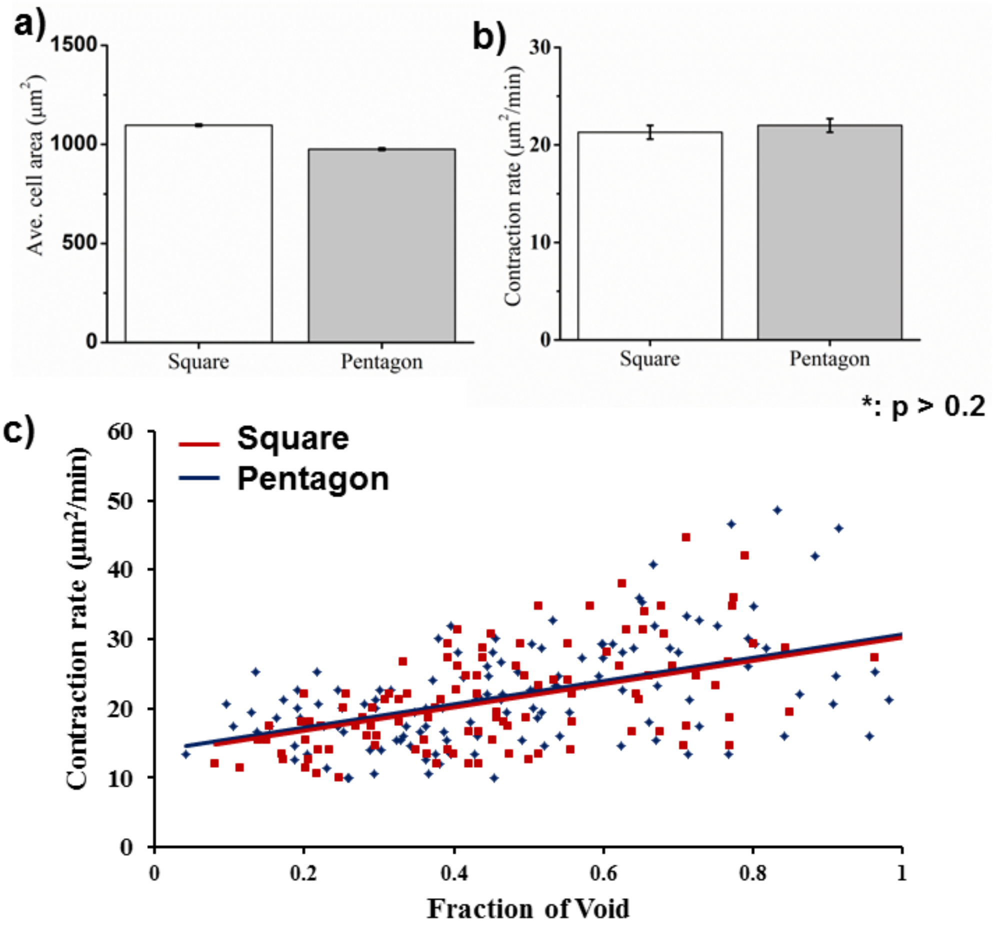

**Fig. 5.8.** Effect of initial void shape on contraction dynamics. Initial void shapes were dependent on cellular ring shapes. a) Plot showing average cell area over the whole contraction process for different ring shapes. b) Plot showing average contraction rates for different ring shapes. c) Plot showing contraction rates with void closure. Data for square rings ($n_{square}$ = 36) depicted in red and pentagon rings ($n_{pentagon}$ = 36) depicted in blue. Linear fit for visualization purposes only. Error bars depict S.E. statistics.

while similar trends were also observed in a plot of contraction rate against void closure as shown in Fig. 5.8.c. To understand these results, it should be noted that even though void closure in the square ring occurred at a slightly higher area regime which would lead to higher contraction rates, it also has a lower cell number and void area compared to pentagon rings. A simple comparison of results obtained earlier in the chapter would suggest that the combined effect of lower cell number and void area in lowering general contraction rates would dominate. Hence, when all other physical conditions are held constant, a void that has an initial square shape would close faster than a pentagon one.

To explain this finding, it was noted that cells lining a square void had highly concave curvatures at the corner of the void (90° corners) while cells lining a pentagon void (108° corners) had less concave curvatures. Previous studies have shown that cells with concave curvatures encourage void closure by purse string-mediated contraction as opposed to straight or convex cell edges [189]. Hence, a more effective actomyosin ring could possibly be assembled in cells with highly concave curvatures, raising the general contraction rates. An indication of this possibility was the observed preference of cells to populate the corner of square rings as shown in Fig. 5.4.d.i.

To further verify that ring contractions were more effective in cells with highly concave curvatures, void closure of a 6-cell ring with an elliptical void were tracked as shown in Fig. 5.9. Cells were initially seeded on micropatterns arranged in a 6-sided polygonal shape as shown in the bottom left corner of Fig 5.9. Here, cells were also observed to populate the corners of the polygon. The four cells with highly concave curvature lining the elliptical void were found at the top and bottom of the ellipse. The edges of the initial void were highlighted in black. At the 10 min and 15 min time points, observable void closure were only observed at the top and bottom of the elliptical cellular ring, similar to the location of the cells with highly concave curvatures. The two other cells in the center of the cellular ring remained relatively unchanged. At the 20 min mark, uneven localized contractions had transformed the elliptical void into a more circular shape and a repositioning of the void was observed at the 25 min mark. After which, the circular void closed symmetrically. Here, it had been shown that an uneven distribution of contractile forces at the inner edge of the cellular ring due to void shape could possibly act to balance itself out and is consistent with the rounding of unevenly shaped voids observed in confluent cell sheets in studies by other groups [187].

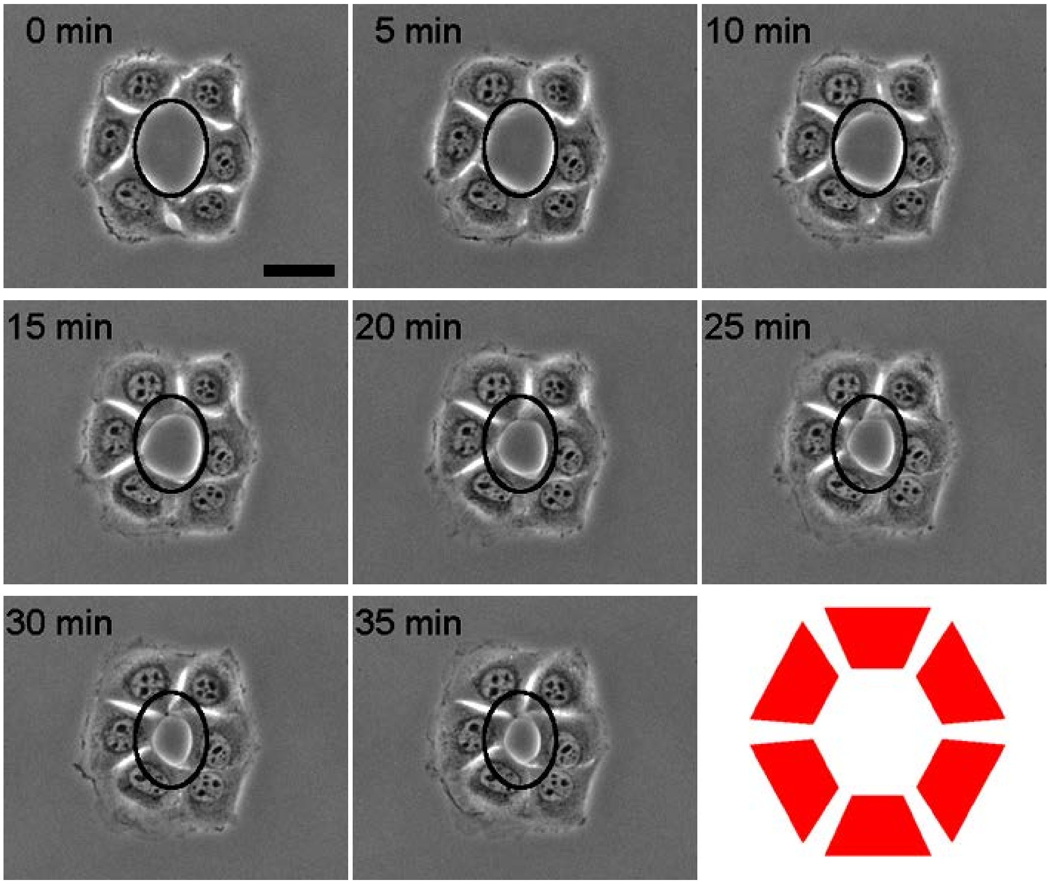

**Fig. 5.9.** Time-lapse phase images showing void closure in 6-cell elliptical ring. Edges of the initial void highlighted in black. Arrangement of micropatterns used shown in red at the bottom left corner. Scale bar depicts 50 μm.

## 5.4 Conclusions

In this chapter, an *in vitro* experimental system to study the dynamics of actomyosin ring contractions was introduced. Cell adhesive micropatterns were arranged in a ring configuration allowing the formation of a cellular ring comprising a single row of 4-6 cells. In this way, actomyosin-mediation contractions to close the void at the center of the cellular ring could be studied without conflicting signals from cell proliferation or cell rearrangement which are unrelated to forces generated by constituent cells. Using this novel *in vitro* experimental system, the influence of individual cell geometry/number as well as cell arrangement in the ring (global void geometry) on the contraction dynamics of actomyosin rings was investigated. Actomyosin mediated contraction of the cellular ring was found to increase with initial cell area and the number of cells forming the ring. Cell arrangement in the ring (global void geometry) was also found to significantly influence the contraction of the cellular ring. Contraction rates were found to be higher on rings with larger void region (only at small void sizes) and also in voids with highly concave curvatures (e.g. a square-shaped void compared to a pentagon shaped void). These results could be explained based on actomyosin-mediated contractility in the cells and the contractile ring and supported by results from previous studies. Although the physical rules uncovered in this chapter were simplistic and general, it showed that the single-row cellular rings could be an attractive *in vitro* experimental system to study the physical parameters governing void closures without conflicting signals from cell proliferation or cell rearrangement.

# Chapter 6

# Conclusions

## 6.1 Conclusions

In this thesis, clusters of micropatterns have been used successfully to demonstrate how the size, shape and arrangement of individual cells in close proximity would regulate cell rearrangement and epithelial void closure and are force-mediated. Some basic physical principles governing these multi-cellular dynamics had been revealed. The rotational dynamics of 2-cell systems on bow-tie patterns can be described by a force-mediated mechanism involving an interplay between driving forces of rotations and resisting forces against rotations. Basic physical parameters that affect actomyosin-mediated contraction in 4- to 6- cell cellular rings had also been established without conflicting signals from cell rearrangement and proliferation which are unrelated to forces generated by constituent cells. Although the size and shape of cells had been used routinely to study the behavior of single cells, these experiments are one of the first attempts to correlate global dynamics of cell clusters with the contributions from individual cells.

In the abovementioned studies, although experiments on micropattern clusters were successfully conducted, the process could be tedious and inefficient. A cell positioning platform that allowed single cells to be positioned on fibronectin micropatterns in a controlled manner was also developed. This platform made use of an array of sieve-like traps in a microfluidic channel to capture and position cells efficiently over adhesive proteins patterned on a coverslip. Fabrication of the microchannel could be achieved easily using soft-lithography from a silicon mold made from a straightforward one-step fabrication process. By using computational fluid dynamics to model fluid flow, cup-shaped and trident-shaped traps flanked by side pillars were designed to allow cells to be trapped either close together or far apart. This flexibility in trapping positions would enable the platform to be compatible with a wide variety of micropattern configurations.

When compared to random seeding, a 4-fold improvement in efficiency was achieved when the platform was used to position paired cells on bowtie patterns and a highly significant 40-fold improvement could be achieved for 6 cells arranged in a ring. The viability of these positioned cells was also found to be similar to randomly seeded cells. After cells were well adhered on the micropatterns, the microchannel could be removed, facilitating high resolution imaging and subsequent manipulation of positioned cells.

Rotation dynamics of a 2-cell system confined in bow-tie shaped micropatterns of different geometries was examined. From the experimental results, the single cell area and the cell-cell contact length had been shown to be important parameters that could influence the rotation potential of cell pairs. Cell shape asymmetry had also been implicated in affecting rotation direction and overall rotation bias. In experiments involving bowtie patterns with different distribution of ECM and when cell pairs were treated with Y27632, changes in rotation potential were amplified in patterns where cell area was small or where contact length was long. Treatment of cell pairs with ML7 yielded very different results where the effect of the drug treatment did not appear to vary with pattern geometries. These observations could be explained using a proposed mechanism where cell pair rotations could be regulated by an interplay between forces driving the rotation and resisting forces opposing it. Driving forces involve both cell-cell forces and the length of cell-cell contact which are thought to be coupled in a rotational moment while focal adhesion density and cell stiffness may account for the resisting forces. Principles governing cell pair rotations were also found to dictate cell rearrangements in 3-cell clusters seeded on large circular patterns.

Actomyosin-mediated contraction dynamics associated with cellular rings formed from a single row of 4-6 cells was examined. The results suggest that both the physical parameter of individual cells and cell arrangement in the ring (global void geometry) exert considerable influence on contraction dynamics associated with these cellular rings. Although *in vivo* void closure by actomyosin contraction typically involved a large number of cells, these singe row cellular rings could be attractive as *in vitro* models to isolate the contribution of cells lining the void. Confounding signals which are unrelated to forces generated by constituent cells such as the shuffling of cells towards and away from the void region was removed and the force-mediated mechanisms governing the behavior of cells lining the void could be examined in greater details.

In summary, designing micropatterns in a cluster can be useful to set up *in vitro* model systems to study the contribution of individual cell geometry, adhesion and arrangement to global behaviour of cell clusters in detail. The efficient use of these micropattern clusters in experiments could also be facilitated with a cell positioning platform which had been shown to efficiently position viable cells on the micropatterns. To demonstrate the utility of these micropattern clusters in biological studies, multi-cellular dynamics of 2-cell systems on bow-tie patterns, 3-cell systems on circular pattern and 4- to 6-cell systems on ring-shaped micropattern clusters had been investigated in this thesis.

## 6.2 Future work

This thesis has laid the groundwork for designing and using clusters of single cell micropattern for studying multi-cellular dynamics. The development of the cell positioning platform also holds much potential as a useful tool for engineering highly sophisticated cell clusters. Further work could be carried out based on the results discussed in this thesis and the directions for these possible researches are briefly described in this section.

In Chapter 3, seamless integration of cup-shaped and trident-shaped traps have been shown when trapping cells in a micropattern ring. This ease of integrating different trap types in the microfluidic channel could open up many exciting opportunities for creating highly complex cell clusters. For example, a myosin knock-down cell could be easily positioned in a ring configuration with 5 other wild type cells and this cell cluster could show very interesting contraction dynamics. The use of sieve like traps in the platform design also allows platform variants to be easily developed. For example, a pair of cells trapped using the trident shaped trap could be allowed to spread fully underneath the trap without removing the microchannel. The half-elliptical structure in the trident shaped traps could be extended to a full ellipse to act as an effective physical barrier to prevent cell-cell adhesion between the fully spread cells. Formation of cell-cell contact could only be initiated when the microchannel is removed. In this way, cellular events at the initial stages of cell-cell adhesion may be examined in a high throughput manner.

In Chapter 4, a mechanism outlining the governing principles for cell pair rotation has been described. As the work in this thesis was focused on examining physical parameters, more biologically involved investigations could be carried out in the future. For example, protein knock-down experiments could be carried out to identify the main cell-cell adhesion molecules that are responsible for the transmission of cell-cell forces. Innovative imaging methods could be employed to confirm that these molecules are indeed concentrated at the periphery of the cell-cell contact. Also, since the 3-cell system on circular pattern was able to recreate a simplified version of cell intercalation in a high throughput manner, it could be useful as a simple *in vitro* model for identifying active molecular players involved in this process.

In Chapter 5, physical parameters of individual cells and global void geometry had been shown to exert considerable influence on contraction dynamics associated with these cellular rings. A similar contraction observed in a row of cells arranged in a horseshoe-shape was only briefly mentioned in the chapter but this result could be further examined to unravel the origin of actomyosin-mediated contractions.

Besides multi-cellular dynamics, other biologically relevant studies could also be carried out using micropattern clusters. For example, positioning of organelles such as the nucleus or centrosomes in a cell had been shown to be dependent on the presence of neighboring cells in its vicinity [90,118]. Exactly how these neighboring cells orientate organelle positioning needs to be examined further. By controlling the exact position of cell neighbors with carefully designed micropattern clusters, an efficient experimental platform could be developed for this purpose. For example, the centrosomes tend to be positioned away from the cell-cell contact for a cell pair on a bow-tie pattern [90]. If a cell is sandwiched between two other cells, does the positioning of its centrosomes return to the cell centroid?

# Bibliography

1. Butcher DT, Alliston T, Weaver VM. (2009). A tense situation: forcing tumour progression. *Nat. Rev. Cancer*. **9**(2), 108-122.
2. Vogel V, Sheetz M. (2006). Local force and geometry sensing regulate cell functions. *Molecular Cell Biology*. **7**, 265-275.
3. Huh D, Matthews BD, Mammoto A, Montaya-Zavala M, Hsin HY, Ingber DE. (2010). Reconstituting organ-level lung functions on a chip. *Science*. **328**, 1662-1668.
4. Wolff J. (1892). Das Gesetz der Transformation der Knochen. August Hirschwald, Berlin.
5. Song JW, Gu W, Futai N, Warner KA, Nor JE, Takayama S. (2005). Computer-Controlled Microcirculatory Support System for Endothelial Cell Culture and Shearing. *Anal. Chem.* **77**, 3993-3999.
6. Wechezak AR, Viggers RF, Sauvage LR. (1985). Fibronectin and F-actin redistribution in cultured endothelial cells exposed to shear stress. *Lab Invest.* **53**(6), 639-647.
7. Akimoto S, Mitsumata M, Sasaguri T, Yoshida Y. (2000). Laminar shear stress inhibits vascular endothelial cell proliferation by inducing cyclin-dependent kinase inhibitor p21(Sdi1/Cip1/Waf1). *Circ Res*. **86**, 185-190.
8. Dimmeler S, Haendeler J, Rippmann V, NehlsM, Zeiher AM. (1996). Shear stress inhibits apoptosis of human endothelial cells. *FEBS Lett.* **399**, 71-74.
9. Garcia-Cardeña G, Comander J, Anderson KR, Blackman BR, Gimbrone MA, Jr. (2001). Biomechanical activation of vascular endothelium as a determinant of its functional phenotype. *Proc. Natl. Acad. Sci. USA.* **98**, 4478-4485.

10. Wang JHC, Thampatty BP. (2008). Mechanobiology of adult and stem cells. *International Review of Cell and Molecular Biology*. **271**, 301-346.
11. Thamilselvan V, Patel A, van der Voort van Zyp J, Basson MD. (2004). Colon cancer cell adhesion in response to Src kinase activation and actin-cytoskeleton by non-laminar shear stress. *J. Cell. Biochem.* **92**(2), 361-371.
12. Hsu H-J, Lee C-F, Locke A, Vanderzyl SQ, Kaunas R. (2010). Stretch-Induced Stress Fiber Remodeling and the Activations of JNK and ERK Depend on Mechanical Strain Rate, but Not FAK. *PLoS One* **5**, e12470.
13. Lee AA, Delhaas T, McCulloch AD, Villarreal FJ. (1999). Differential Responses of Adult Cardiac Fibroblasts to in vitro Biaxial Strain Patterns. *J. Mol. Cell. Cardiol.* **31**,1833-1843.
14. Svennersten K, Berggren M, Richter-Dahlfors A, Jager EWH. (2011). Mechanical stimulation of epithelial cells using polypyrrole microactuators. *Lab Chip*. **11**, 3287-3293.
15. Ventre M, Causa F, Netti PA. (2012). Determinants of cell-material crosstalk at the interface: towards engineering cell instructive materials. *J. R. Soc. Interface.* **9**, 2017-2032.
16. Wang HB, Dembo M, Wang YL. (2000). Substrate flexibility regulates growth and apoptosis of normal but not transformed cells. *Am. J. Physiol. Cell Physiol*. **279**, C1345-C1350
17. Pelham RJ, Jr., Wang Y. (1997). Cell locomotion and focal adhesions are regulated by substrate flexibility. *Proc. Natl. Acad. Sci. USA*. **94**(25), 13661-13665.
18. Lo CM, Wang HB, Dembo M, Wang YL. (2000). Cell movement is guided by the rigidity of the substrate. *Biophys J.* **79**(1), 144-152.

19. Engler AJ, Sen S, Sweeney HL, Discher DE. (2006). Matrix elasticity directs stem cell lineage specification. *Cell*. **126**(4), 677-689.

20. Turner AM, Dowel N, Turner SW, Kam L, Isaacson M, Turner JN, Craighead HG, Shain W. (2000). Attachment of astroglial cells to microfabricated pillar arrays of different geometries. *J. Biomed. Mater. Res.* **51**(3), 430-441.

21. Lamers E, van Horssen R, te Riet J, van Delft FC, Luttge R, Walboomers XF, Jansen JA. (2010). The influence of nanoscale topographical cues on initial osteoblasts morphology and migration. *Eur. Cell. Mater*. **20**, 329-343.

22. Loesberg WA, te Riet J, van Delft FC, Schon P, Figdor CG, Speller S, van Loon JJ, Walboomers XF, Jansen JA. (2007). The threshold at which substrate nanogroove dimensions may influence fibroblast alignment and adhesion. *Biomaterials*. **27**, 3944-3951.

23. Clark P, Connolly P, Curtis AS, Dow JA, Wilkinson CD. (1990). Topographical control of cell behavior: II. Multiple grooved substrata. *Development*. **108**(4), 635-644.

24. Tan J, Saltzman WM. (2002). Topographical control of human neutrophil motility on micropatterned materials with various surface chemistry. *Biomaterials*. **23**, 3215-3225.

25. Yim EK, Reano RM, Pang SW, Yee AF, Chen CS, Leong KW. (2005). Nanopattern-induced changes in morphology and motility of smooth muscle cells. *Biomaterials*. **26**, 5405-5413.

26. Ghibaudo M, Trichet L, Le Digabel J, Richert A, Hersen P, Ladoux B. (2009). Substrate topography induces a crossover from 2D to 3D behavior in fibroblast migration. *Biophys J*. **97**(1), 357-368.

27. Seo CH, Furukawa K, Suzuki Y, Kasagi N, Ichiki T, Ushida T. (2011). A topographically optimized substrate with well-ordered lattice micropatterns for

enhancing the osteogenic differentiation of murine mesenchymal stem cells. *Macromol. Biosci.* **11**(7), 938-945.

28. Dalby MJ, Gadegarrd N, Tare R, Andar A, Riehle MO, Herzyk P, Wilkinson CD, Oreffo RO. (2007). The control of human mesenchymal cell differentiation using nanoscale symmetry and disorder. *Nat. Mater.* **6**, 997-1003.
29. Yim EK, Pang SW, Leong KW. (2007). Synthetic nanostructures inducing differentiation of human mesenchymal stem cells into neuronal lineage. *Exp. Cell Res.* **313**(9), 1820-1829.
30. Christopherson GT, Song H, Mao HQ. (2009). The influence of fiber diameter of electrospun substrates on neural stem cell differentiation and proliferation. *Biomaterials*. **30**(4), 556-564.
31. Gilbert SF. (2013). *Developmental Biology*. Sinauer Associates, Inc. Sunderland, USA
32. Thompson DW. (1915). *On Growth and Form*. Cambridge University Press. New York.
33. Trinkaus JP. (1969). *Cells into Organs. The Forces That Shape the Embryo*. Prentice-Hall. Englewood Cliffs, N.J.
34. Tabata T, Takei Y. (2004). Morphogens, their identification and regulation. *Development*. **131**(4), 703-712.
35. Hannezo E, Prost J, Joanny J-F. (2014). Theory of epithelial sheet morphology in three dimensions. *Proc. Natl. Acad. Sci. USA.* **111**(1), 27-32.
36. Rooji J. (2014). Cadherin adhesion controlled by cortical actin dynamics. *Nat. Cell Biol.* **16**(6), 508-510.
37. Vasiliev JM, Gelfand IM, Domnina LV, Rappoport RI. (1969). Wound healing processes in cell cultures. *Exp. Cell Res.* **54**(1), 83-93.

38. Fenteany G, Janmey PA, Stossel TP. (2000). Signaling pathways and cell mechanics involved in wound closure by epithelial cell sheets. *Curr. Biol.* **10**(14), 831-838.

39. Bement WM, Forscher P, Mooseker MS. (1993). A novel cytoskeletal structure involved in purse string wound closure and cell polarity maintenance. *J. Cell Biol.* **121**(3), 565-578.

40. Brock J, Midwinter K, Lewis J, Martin P. (1996). Healing of incisional wounds in the embryonic chick wing bud: characterization of the actin purse-string and demonstration of a requirement for Rho activation. *J. Cell Biol.* **135**(4), 1097-1107.

41. Grasso S, Hernández JA, Chifflet S. (2007). Roles of wound geometry, wound size, and extracellular matrix in the healing response of bovine corneal endothelial cells in culture. *Am J Physiol Cell Physiol.* **293**(4), 1327-1337.

42. Gray DS, Liu WF, Shen CJ, Bhadriraju K, Nelson CM, Chen CS. (2008). Engineering amount of cell-cell contact demonstrates biphasic proliferative regulation through RhoA and the actin cytoskeleton. *Exp. Cell Res.* **314**(15), 2846-2854.

43. Ingber DE, Folkman J. (1989). Mechanochemical switching between growth and differentiation during fibroblast growth factor-stimulated angiogenesis in vitro: role of extracellular matrix. *J. Cell Biol.* **109**(1), 317-330.

44. Singhvi R, Kumar A, Lopez GP, Stephanopoulos GN, Wang DI, Whitesides GM, Ingber DE. (1994). Engineering cell shape and function. *Science.* **264**, 696-698.

45. Folch A, Toner M. (2000). Microengineering of cellular interactions. *Annu. Rev. Biomed. Eng.* **2**, 227-256.

46. Falconnet D, Csucs G, Grandin HM, Textor M. (2006). Surface engineering approaches to micropattern surfaces for cell-based assays. *Biomaterials* **27**, 3044-3063.

47. Nakanishi J, Takarada T, Yamaguchi K, Maeda M. (2008). Recent Advances in Cell Micropatterning Techniques for Bioanalytical and Biomedical Sciences. *Anal. Sci* **24**(1), 67-72.

48. Nelson CM, Raghavan S, Tan JL, Chen CS. (2002). Degradation of Micropatterned Surfaces by Cell-Dependent and -Independent Processes. *Langmuir* **19**(5), 1493–1499.

49. Fink J, Théry M, Azioune A, Dupont R, Chatelain F, Bornens M, Piel M. (2006). Comparative study and improvement of current cell micro-patterning techniques. *Lab chip* **7**, 672–680.

50. Charest JL, Jennings JM, King WP, Kowalczyk AP, Garcı´a AJ. (2009). Cadherin-Mediated Cell–Cell Contact Regulates Keratinocyte Differentiation. *Journal of Investigative Dermatology* **129**, 564–572.

51. Gallant ND, Michael KE, Garcı´a AJ. (2005). Cell Adhesion Strengthening: Contributions of Adhesive Area, Integrin Binding, and Focal Adhesion Assembly. *Molecular Biology of the Cell.* **16**: 4329–4340.

52. Chen CS, Alonso JL, Ostuni E, Whitesides GM, Ingber DE. (2003). Cell shape provides global control of focal adhesion assembly. *Biochemical and Biophysical Research Communications.* **307**, 355–361.

53. Brock A, Chang E, Ho C-C, LeDuc P, Jiang X, Whitesides GM, Ingber DE. (2003). Geometric Determinants of Directional Cell Motility Revealed Using Microcontact Printing. *Langmuir.* **19**,1611-1617.

54. Jiang X, Bruzewicz DA, Wong AP, Piel M, Whitesides G.M. (2005). Directing cell migration with asymmetric micropatterns. *Proc. Natl. Acad. Sci. USA* **102**(4), 975-978.

55. Dike LE, Chen CS, Mrksich M, Tien J, Whitesides GM, Ingber DE. (1999). Geometric control of switching between growth, apoptosis, and differentiation during angiogenesis using micropatterned substrates. *In Vitro CeIl. Dev. Biol.-Anima1*. **35**: 441-448.

56. James CD, Davis RC, Kam L, Craighead HG, Issacson M, Turner JN, Shain W. (1998). Patterned Protein Layers on Solid Substrates by Thin Stamp Microcontact Printing. *Langmuir*. **14**(4), 741-744.

57. Tang X, Ali MY, Saif MT. (2012). A Novel Technique for Micro-patterning Proteins and Cells on Polyacrylamide Gels. *Soft Matter*. **8**(27), 7197-7206.

58. Nelson CM, Liu WF, Chen CS. (2007). Manipulation of Cell–Cell Adhesion Using Bowtie-Shaped Microwells. *Methods in Molecular Biology* **370**, 1-10.

59. Tan CP, Seo BR, Brooks DJ, Chandler EM, Craighead HG, Fischbach C. (2009). Parylene peel-off arrays to probe the role of cell-cell interactions in tumour angiogenesis. *Integr. Biol.* **1**, 587-594.

60. Folch A, Jo B-H, Hurtado O, Beebe DJ, Toner M. (2000). Microfabricated elastomeric stencils for micropatterning cell cultures. *J. Biomed. Mater. Res.* **52**(2), 346-353.

61. Jinno S, Moeller HC, Chen CL, Rajalingam B, Chung BG, Dokmeci MR, Khademhosseini A. (2008). Microfabricated multilayer parylene-C stencils for the generation of patterned dynamic co-cultures. *J. Biomed. Mater. Res. A.* **86**(1), 278-288.

62. Michel R, Lussi JW, Csucs G, Reviakine I, Danuser G, Ketterer B, Hubbell JA, Textor M, Spencer ND. (2002). Selective Molecular Assembly Patterning: A

New Approach to Micro- and Nanochemical Patterning of Surfaces for Biological Applications. *Langmuir*. **18**(8), 3281-3287.

63. Azioune A, Storch M, Bornens M, Théry M, Piel M. (2009). Simple and rapid process for single cell micro-patterning. *Lab Chip* **9**, 1640–1642.
64. Nakanishi J, Kikuchi Y, Takarada T, Nakayama H, Yamaguchi K, Maeda M. (2006). Spatiotemporal control of cell adhesion on a self-assembled monolayer having a photocleavable protecting group. *Analytica Chimica Acta*. **578**, 100–104.
65. Yang Z, Frey W, Oliver T, Chilkoti A. (2000). Light-Activated Affinity Micropatterning of Proteins on Self-Assembled Monolayers on Gold. *Langmuir*. **16**, 1751-1758.
66. Douvas AM, Petrou PS, Kakabakos SE, Misiakos PA, Sarantopoulou ZK, Cefalas AC. (2005). 157-nm Laser ablation of polymeric layers for fabrication of biomolecule microarray. *Anal. Bioanal. Chem.* **381**, 1027-1032.
67. Okano K, Matsui A, Maezawa Y, Hee P-Y, Matsubara M, Yamamoto H, Hosokawa Y, Tsubokawa H, Li Y-K, Kao F-J, Masuhara H. (2013). *In situ* laser micropatterning of proteins for dynamically arranging living cells. *Lab Chip* **13**, 4078-4086.
68. Yu F, Li P, Shen H, Mathur S, Lehr C-M, Bakowsky U, Mucklich F. (2005). Laser interference lithography as a new and efficient technique for micropatterning of biopolymer surface. *Biomaterials* **26**, 2307-2312.
69. Heinz WF, Hoh M, Hoh JH. (2011). Laser inactivation protein patterning of cell culture microenvironments. *Lab Chip* **11**, 3336-3346.
70. Tourovskaia A, Barber T, Wickes BT, Hirdes D, Grin B, Castner DG, Healy KE, Folch A. (2003). Micropatterns of Chemisorbed Cell Adhesion-Repellent Films Using Oxygen Plasma Etching and Elastomeric Masks. *Langmuir*. **19**, 4754-4764.

71. Junkin M, Wong PK. (2011). Probing cell migration in confined environments by plasma lithography. *Biomaterials.* **32**, 1848-1855.

72. Rhee SW, Taylor AM, Tu CH, Cribbs DH, Cotman CW, Jeon NL. (2005). Patterned cell culture inside microfluidic devices. *Lab Chip* **5**, 102-107.

73. Deguchi S, Nagasawa Y, Saito AC, Matsui TS, Yokoyama S, Sato M. (2014). Development of motorized plasma lithography for cell patterning. *Biotechnol. Lett.* **36**(3), 507-513.

74. Tien J, Nelson CM, Chen CS. (2002). Fabrication of aligned microstructures with a single elastomeric stamp. *Proc. Natl. Acad. Sci. USA* **99**(4), 1758-1762.

75. Chiu DT, Jeon NL, Huang S, Kane RS, Wargo CJ, Choi IS, Ingber DE, Whitesides GM. (2000). Patterned deposition of cells and proteins onto surfaces by using three-dimensional microfluidic systems. *Proc. Natl. Acad. Sci. USA* **97**(6), 2408-2413.

76. Gropeanu M, Bhagawati M, Gropeanu RA, Rodriguez Muniz GM, Sundaram S, Piehler J, del Campo A. (2013). A versatile toolbox for multiplexed protein micropatterning by laser lithography. *Small.* **9**(6), 838-845.

77. Yousaf MN, Houseman BT, Mrksich M. (2001). Using electroactive substrates to pattern the attachment of two different cell populations. *Proc. Natl. Acad. Sci. USA* **98**(11), 5992-5996.

78. Jiang X, Ferrigno R, Mrksich M, Whitesides GM. (2003). Electrochemical desorption of self-assembled monolayers noninvasively releases patterned cells from geometrical confinements. *J. Am. Chem. Soc.* **125**(9), 2366-2367.

79. Yamato M., Kwon O.H., Hirose M., Kikuchi A., Okano T. (2001). Novel patterned cell coculture utilizing thermally responsive grafted polymer surfaces. *J. Biomed. Mater. Res.* **55**(1), 137-140.

80. Vignaud T, Galland R, Tseng Q, Blanchoin L, Colombelli J, Théry M. (2012). Reprogramming cell shape with laser nano-patterning. *J. Cell Sci*. **129**, 2134-2140.

81. Chen CS, Mrksich M, Huang S, Whitesides GM, Ingber DE. (1997). Geometric Control of Cell Life and Death. *Science*. **276**, 1425-1428.

82. Gallant ND, Capadona JR, Frazier AB, Collard DM, Garciá AJ. (2002). Micropatterned Surfaces to Engineer Focal Adhesions for Analysis of Cell Adhesion Strengthening. *Langmuir*. **18**, 5579-5584.

83. James J, Goluch ED, Hu H, Liu C, Mrksich M. (2008). Subcellular Curvature at the Perimeter of Micropatterned Cells Influences Lamellipodial Distribution and Cell Polarity. *Cell Motility and the Cytoskeleton.* **65**, 841-852.

84. Parker KK, Brock AL, Brangwynne C, Mannix RJ, Wang N, Ostuni E, Geisse NA, Adams JC, Whitesides GM, Ingber DE. (2002). Directional control of lamellipodia extension by constraining cell shape and orienting cell tractional forces. *FASEB J.* **16**, 1195-1204.

85. Huda S, Soh S, Pilans D, Byrska-Bishop M, Kim J, Wilk G, Borisy GG, Kandere-Grzybowska K, Grzybowki BA. (2012). Microtubule guidance tested through controlled cell geometry. *J. Cell Sci.* **125**(23), 5790-5799.

86. Théry M, Pépin A, Dressaire E, Chen Y, Bornens M. (2006). Cell Distribution of Stress Fibers in Response to the Geometry of the Adhesive Environment. *Cell Motility and the Cytoskeleton.* **63**, 341-355.

87. Théry M, Racine V, Piel M, Pépin A, Dimitrov A, Chen Y, Sibarita J-B, Bornens M. (2006). Anisotropy of cell adhesive microenvironment governs cell internal organization and orientation of polarity. *Proc. Natl. Acad. Sci. USA* **103**(52), 19771-19776.

88. Théry M, Racine V, Pépin A, Piel M, Chen Y, Sibarita J-B, Bornens M. (2005). The extracellular matrix guides the orientation of the cell division axis. *Nat. Cell Biol.* **7**(10), 947-953.

89. Théry M, Jiménez-Dalmaroni A, Racine V, Bornens M, Jülicher F. (2007). Experimental and theoretical study of mitotic spindle orientation. *Nature.* **447**, 493-497.

90. Desai RA, Gao L, Raghavan S, Liu WF, Chen CS. (2008). Cell polarity triggered by cell-cell adhesion via E-cadherin. *J. Cell Sci.* **122**(7), 905-911.

91. Lambert M, Thoumine O, Brevier J, Choquet D, Riveline D, Mège R-M. (2007). Nucleation and growth of cadherin adhesions. *Expt. Cell. Res.* **313**, 4025-4040.

92. Borghi N, Lowndes M, Maruthamuthu V, Gardel ML, Nelson WJ. (2010). Regulation of cell motile behavior by crosstalk between cadherin- and integrin-mediated adhesions. *Proc. Natl. Acad. Sci. USA* **107**(30), 13324-13329.

93. Huang S, Chen CS, Ingber DE. (1998). Control of Cyclin D1, p27$^{\mathrm{Kip1}}$, and Cell Cycle Progression in Human Capillary Endothelial Cells by Cell Shape and Cytoskeletal Tension. *Mol. Biol. Cell.* **9**, 3179-3193.

94. Pirone DM, Liu WF, Ruiz SA, Gao L, Raghavan S, Lemmon CA, Romer LH, Chen CS. (2006). An inhibitory role for FAK in regulating proliferation: a link between limited adhesion and RhoA-ROCK signaling. *J. Cell Biol.* **174**(2), 277-288.

95. Nelson CM, Chen CS. (2002). Cell-cell signaling by direct contact increases proliferation via a PI3K-dependent signal. *FEBS Letters.* **514**, 238-242.

96. Nelson CM, Chen CS. (2003). VE-cadherin simultaneously stimulates and inhibits cell proliferation by altering cytoskeletal structure and tension. *J. Cell Sci.* **116**(17) 3571-3581.

97. Liu WF, Nelson CM, Pirone DM, Chen CS. (2006). E-cadherin engagement stimulates proliferation via Rac1. *J. Cell Biol.* **173**(3), 431-441.

98. Thakar RG, Cheng Q, Patel S, Chu J, Nasir M, Liepmann D, Komvopoulos K, Li S. (2009). Cell-Shape Regulation of Smooth Muscle Cell Proliferation. *Biophys. J.* **96**, 3423-3432.

99. McBeath R, Pirone DM, Nelson CM, Bhadriraju K, Chen CS. (2004). Cell Shape, Cytoskeletal Tension, and RhoA Regulate Stem Cell Lineage Commitment. *Developmental Cell* **6**, 483–495.

100. Connelly JT, Gautrot JE, Trappmann B, Tan DW, Donati G, Huck WT, Watt FM. (2010). Actin and serum response factor transduce physical cues from the microenvironment to regulate epidermal stem cell fate decisions. *Nat. Cell Biol.* **12**(7), 711-718.

101. Gao L, McBeath R, Chen CS. (2010). Stem Cell Shape Regulate a Chondrogenic Versus Myogenic Fate Through Rac1 and N-Cadherin. *Stem Cells.* **28**(3), 564-572.

102. Peng R, Yao X, Ding J. (2011). Effect of cell anisotropy on differentiation of stem cells on micropatterned surfaces through the controlled single cell adhesion. *Biomaterials.* **32**, 8048-8057.

103. Kilian KA, Bugarija B, Lahn BT, Mrksich M. (2010). Geometric cues for directing the differentiation of mesenchymal stem cells. *Proc. Natl. Acad. Sci. USA* **107**, 4872-4877.

104. Tay CY, Pal M, Yu H, Leong WS, Tan NS, Ng KW, Venkatraman S, Boey F, Leong DT, Tan LP. (2011). Bio-inspired Micropatterned Platform to Steer Stem Cell Differentiation. *Small* **7**, 4872-4877.

105. Kandere-Grzybowska K, Soh S, Mahmud G, Komarova Y, Pilans D, Grzybowski BA. (2010). Short-term molecular polarization of cells on symmetric and asymmetric micropatterns. *Soft Matter*. **6**, 3257-3268.

106. Kumar G, Ho C-C, Co CC. (2007). Guiding Cell Migration Using One-Way Micropattern Arrays. *Adv. Mater.* **19**, 1084-1090.

107. Kumar G, Co CC, Ho C-C. (2011). Steering Cell Migration Using Microarray Amplification of Natural Directional Persistence. *Langmuir*. **27**, 3803-3807.

108. Kushiro K, Chang S, Asthagiri AR. (2010). Reprogramming Directional Cell Motility by Tuning Micropattern Features and Cellular Signals. *Adv. Mater.* **22**, 4516-4519.

109. Mahmud G, Campbell CJ, Bishop KJ, Komarova YA, Chaga O, Soh S, Huda S, Kandere-Grzybowska K, Grzybowski BA. (2009). Directing cell motions on micropatterned ratchets. *Nat. Phys.* **5**, 606-612.

110. Song HK, Toste B, Ahmann K, Hoffman-Kim D, Palmore GT. (2006). Micropatterns of positive guidance cues anchored to polypyrrole doped with polyglutamic acid: A new platform for characterizing neurite extension in complex environments. *Biomaterials.* **27**, 473-484.

111. Féréol S, Fodil R, Barnat M, Georget V, Milbreta U, Nothias F. (2011). Micropatterned ECM Substrates Reveal Complementary Contribution of Low and High Affinity Ligands to Neurite Outgrowth. *Cytoskeleton.* **68**, 373-388.

112. Jang MJ, Namgung S, Hong S, Nam Y. (2010). Directional neurite growth using carbon nanotubes patterned substrates as a biomimetic cue. *Nanotechnology*. **21**(23), 235102.

113. Roth S, Bisbal M, Brocard J, Bugnicourt G, Saoudi Y, Andrieux A, Gory-Fauré S, Villard C. (2012). How Morphological Constraints Affect Axonal Polarity in Mouse Neurons. *PLoS One.* **7**(3), e33623.

114. Nelson CM, Jean RP, Tan JL, Liu WF, Sniadecki NJ, Spector AA, Chen CS. (2005). Emergent patterns of growth controlled by multicellular form and mechanics. *Proc. Natl. Acad. Sci. USA* **102**(33), 11594-11599.

115. Ruiz SA, Chen CS. (2008). Emergence of Patterned Stem Cell Differentiation Within Multicellular Structures. *Stem Cells.* **26**(11), 2921-2927.

116. Gomez EW, Chen QK, Gjorevski N, Nelson CM. (2010). Tissue geometry patterns epithelial-mesenchymal transition via intercellular mechanostransduction. *J. Cell. Biochem.* **110**(1), 44-51.

117. Kumar G, Chen B, Co CC, Ho C-C. (2011). Differential migration and proliferation of geometrical ensemble of cell clusters. *Expt. Cell Res.* **317**, 1340-1352.

118. Dupin I, Camand E, Etienne-Manneville S. (2009). Classical cadherins control nucleus and centrosomes position and cell polarity. *J. Cell Biol.* **185**(5), 779-786.

119. Vedula SR, Leong MC, Lai TL, Hersen P, Kabla AJ, Lim CT, Ladoux B. (2012). Emerging modes of collective cell migration induced by geometrical constraints. *Proc. Natl. Acad. Sci. USA* **109**(32), 12974-12979.

120. Vedula SR, Hirata H, Nai MH, Brugués A, Toyama Y, Trepat X, Lim CT, Ladoux B. (2014). Epithelial bridges maintain tissue integrity during collective cell migration. *Nat. Mater.* **13**, 87-96.

121. Desai RA, Gopal SB, Chen S, Chen CS. (2013). Contact inhibition of locomotion probabilities drive solitary versus collective cell migration. *J. R. Soc. Interface.* **10**, 20130717.

122. Doxzen K, Vedula SR, Leong MC, Hirata H, Gov NS, Kabla AJ, Ladoux B, Lim CT. (2013). Guidance of collective cell migration by substrate geometry. *Integr. Biol.* **5**, 1026-1035.

123. Wan LQ, Ronaldson K, Park M, Taylor G, Zhang Y, Gimble JM, Vunjak-Novakovic G. (2011). Micropatterned mammalian cells exhibit phenotype-specific left-right symmetry. *Proc. Natl. Acad. Sci. USA* **108**(30), 12295-12300.

124. Zhang D, Kilian KA. (2013). The effect of mesenchymal stem cell shape on the maintenance of multipotency. *Biomaterials.* **34**, 3962-3969.

125. Lam H, Patel S, Wong J, Chu J, Li A, Li S. (2008). Localized decrease of β-catenin contributes to the differentiation of human embryonic stem cells. *Biochemical and Biophysical Research Communications.* **372**, 601-606.

126. Peerani R, Rao BM, Bauwens C, Yin T, Wood GA, Nagy A, Kumacheva E, Zandstra PW. (2007). Niche-mediated control of human embryonic stem cell self-renewal and differentiation. *EMBO Journal.* **26**, 4744-4755.

127. Bauwens CL, Peerani R, Niebruegge S, Woodhouse KA, Kumacheva E, Husain M, Zandstra PW. (2008). Control of Human Embryonic Stem Cell Colony and Aggregate Size Heterogenity Influences Differentiation Trajectories. *Stem Cells.* **26**, 2300-2310.

128. Molnar P, Wang W, Natarajan A, Rumsey JW, Hickman JJ. (2007). Photolithographic Patterning of C2C12 Myotubes using Vitronectin as Growth Substrate in Serum-Free Medium. *Biotechnol. Prog.* **23**(1), 265-268.

129. Li B, Lin M, Tang Y, Wang B, Wang JH. (2008). A novel functional assessment of the differentiation of micropatterned muscle cells. *J. Biomech.* **41**(16), 3349-3353.

130. Bajaj P, Reddy B, Jr., Millet L, Wei C, Zorlutuna P, Bao G, Bashir R. (2011). Patterning the differentiation of C2C12 skeletal myoblasts. *Integr. Biol.* **3**, 897-909.

131. Tseng Q, Duchemin-Pelletier E, Deshiere A, Balland M, Guillou H, Filhol O, Théry M. (2012). Spatial organization of extracellular matrix regulates cell-cell junction positioning. *Proc. Natl. Acad. Sci. USA* **109**(5), 1506-1511.

132. Anis YH, Holl MR, Meldrum DR. (2010). Automated selection and placement of single cells. *IEEE Transactions on Automation Science and Engineering,* **7**, 598-606

133. Lu Z, Moraes C, Ye G, Simmons CA, Sun Y. (2010). Single cell deposition and patterning with a robotic system. *PLoS ONE*, **5,** e0013542

134. Rettig JR, Folch A. (2005). Large-scale single-cell trapping and imaging using microwell arrays. *Anal. Chem.* **77**(17), 5628-5634.

135. Tang J, Peng R, Ding J. (2010). The regulation of stem cell differentiation by cell-cell contact on micropatterned material surfaces. *Biomaterials.* **31**(9), 2470-2476.

136. Doh J, Kim M, Krummel MF. (2010). Cell-laden microwells for the study of multi-cellularity in lymphocyte fate decisions. *Biomaterials.* **31**(12), 3422-3428.

137. Voldman J, Gray ML, Toner M, Schmidt MA. (2002). A microfabricated dynamic array cytometer. *Anal. Chem.* **74**(16), 3984-3990.

138. Thomas RS, Morgan H, Green NG. (2009). Negative DEP traps for single cell immobilization. *Lab Chip* **9**(11), 1534-1540.

139. Chiou PY, Ohta AT, Wu MC. (2005). Massively parallel manipulation of single cells and microparticles using optical images. *Nature* **436**(7049), 370-372.

140. Gray DS, Tan JL, Voldman J, Chen CS. (2004). Dielectrophoretic registration of living cells to a microelectrode array. *Biosens Bioelectron.* **19**(12), 1765-1774.

141. Di Carlo D, Aghdam N, Lee LP. (2006). Single-cell enzyme concentrations, kinetics, and inhibition analysis using high-density hydrodynamic cell isolation arrays. *Anal. Chem.* **78**(14), 4925-4930.

142. Skelley AM, Kirak O, Suh H, Jaenisch R, Voldman J. (2009). Microfluidic control of cell pairing and fusion. *Nat. Methods.* **6**(2), 147-152.

143. Lee PJ, Hung PJ, Shaw R, Jan L, Lee LP. (2005). Microfluidic application-specific integrated device for monitoring direct cell-cell communication via gap junctions between individual cell pairs. *Appl. Phys. Lett.* **86**, 223902-223904.

144. Frimat JP, Becker M, Chiang YY, Marggraf U, Janasek D, Hengstler JG, Franzke J, West J. (2009). A microfludic array with cellular valving for single cell co-culture. *Lab Chip* **9**(11), 1534-1540.

145. Mittal N, Rosenthal A, Voldman J. (2007). nDEP microwells for single-cell patterning in physiological media. *Lab Chip* **7**(9), 1146-1153.

146. Reyes DR, Hong JS, Elliot JT, Gaitan M. (2011). Hybrid cell adhesive material for instant dielectrophoretic cell trapping and long-term cell function assessment. *Langmuir*. **27**(16), 10027-10034.

147. Yan C, Sun J, Ding J. (2011). Critical areas of cell adhesion on micropatterned surfaces. *Biomaterials.* **32**(16), 3931-3938.

148. Lai SL, Johnson D, Westerman R. (2006). Aspect ratio dependent etching lag reduction in deep silicon etch processes. *J. Vac. Sci. Technol. A.* **24**(4), 1283-1288.

149. Lee SW, Lee SS. (2008). Shrinkage ratio of PDMS and its alignment method for the wafer level process. *Microsyst. Technol.* **14**(2), 205-208.

150. Regehr KJ, Domenech M, Koepsel JT, Carver KC, Ellison-Zelski SJ, Murphy WL, Schuler LA, Alarid ET, Beebe DJ. (2009). Biological implications of polydimethylsiloxane-baased microfluidic cell culture. *Lab Chip* **9**(15), 2132-2139.

151. Miki Y, Ono K, Hata S, Suzuki T, Kumamoto H, Sasano H. (2012). The advantages of co-culture over mono cell-culture in simulating in vivo environment. *J. Steroid Biochem. Mol. Biol.* **131**(3-5), 68-75.

152. Kaji H, Camci-Unal G, Langer R, Khademhosseini A. (2012). Engineering systems for the generation of patterned co-cultures for controlling cell-cell interactions. *Biochim. Biophys. Acta.* **1810**(3), 239-250. Hong S, Pan Q, Lee LP.

153. Single-cell level co-culture platform for intercellular communication. *Intergr. Biol.* ***4*(**4), 374-380.

154. Felton EJ, Copeland CR, Chen CS, Reich DH. (2012). Heterotypic cell pair co-culturing on patterned microarrays. *Lab Chip* **12**(17), 3117-3126.

155. Huang S, Brangwynne CP, Parker KK, Ingber DE. (2005). Symmetry-breaking in mammalian cell cohort migration during tissue pattern formation: role of random-walk persistence. *Cell Motil. Cytoskeleton.* **61**(4), 201-213.

156. Wang H, Lacoche S, Huang L, Xue B, Muthuswamy SK. (2013). Rotational motion during three-dimensional morphogenesis of mammary epithelial acini relates to laminin matrix assembly. *Proc. Natl. Acad. Sci. USA* **110**(1), 163-168.

157. Marmaras A, Berge U, Ferrari A, Kurtcuoglu V, Poulikakos D. Kroschewski R. (2010). A Mathematical Method for the 3D Analysis of Rotating Deformable Systems Applied on Lumen-Forming MDCK Cell Aggregates. *Cytoskeleton.* **67**(4), 224-240.

158. Tanner K, Mori H, Mroue R, Bruni-Cardoso A, Bissel MJ. (2012). Coherent angular motion in the establishment of multicellular architecture of glandular tissues. *Proc. Natl. Acad. Sci. USA* **109**(6), 1973-1978.

159. Haigo SL, Bilder D. (2011). Global tissue revolutions in a morphogenetic movement controlling elongation. *Science* **331**, 1071-1074.

160. Yang N, Inaki M, Cliffe A, Rørth P. (2012). Microtubules and Lis-1/NudE/Dynein regulate invasive cell-on-cell migration in Drosophila. *PLoS One.* **7**(7), e40632.

161. Escudero LM, Dischoff M, Freeman M. (2007). Myosin II regulates complex cellular arrangement and epithelial architecture in Drosophila. *Dev. Cell.* **13**(5), 717-729.

162. Wilson PA, Oster G, Keller R. (1989). Cell rearrangement and segmentation in *Xenopus*: direct observation of cultured explants. *Development.* **105**, 155-166.

163. Samakovlis C, Hacohen N, Manning G, Sutherland DC, Guillemin K, Krasnow MA. (1996). Development of the Drosophila tracheal system occurs by a series of morphologically distinct but genetically coupled branching events. *Development.* **122**, 1395-1407.

164. Affolter M, Bellusci S, Itoh N, Shilo B, Thiery JP, Werb Z. (2003). Tube or Not Tube: Remodeling epithelial tissues by branching morphogenesis. *Dev. Cell.* **4**, 11-18.

165. Lecuit T, Lenne PF. (2007). Cell surface mechanics and the control of cell shape, tissue patterns and morphogenesis. *Nat. Rev. Mol. Cell Biol.* **8**(8), 633-644.

166. Kino-oka M, Agatahama Y, Hata N, Taya M. (2004). Evaluation of growth potential of human epithelial cells by motion analysis of pairwise rotation under glucose-limited condition. *Biochemical Engineering Journal.* **19**, 109-117.

167. Wakatsuki T, Wysolmerski RB, Elson EL. (2003). Mechanics of cell spreading: role of myosin II. *J. Cell Sci.* **116**, 1617-1625.

168. Carpenter AE, Jones TR, Lamprecht MR, Clarke C, Kang IH, Friman O, Guertin DA, Chang JH, Lindquist RA, Moffat J, Golland P, Sabatini DM. (2006).

CellProfiler: image analysis software for identifying and quantifying cell phenotypes. *Genome Biol.* **7**(10), R100

169. Weliky M, Oster G. (1990). The mechanical basis of cell rearrangement. *Development.* **109**, 373-386.

170. Chiou KK, Hufnagel L, Shraiman BI. (2012). Mechanical stress inference for two dimensional cell arrays. *PLoS Comput. Biol.* **8**(5), e1002512.

171. Maruthamuthu V, Sabass B, Schwarz US, Gardel ML. (2011). Cell-ECM traction force modulates endogenous tension at cell-cell contacts. *Proc. Natl. Acad. Sci. USA* **108**(12), 4708-4713.

172. Roca-Cusachs P, Alcaraz J, Sunyer R, Samitier J, Farré R, Navajas D. (2008). Micropatterning of single endothelial cell shape reveals a tight coupling between nuclear volume in G1 and proliferation. *Biophys. J.* **94**(12), 4984-4995.

173. Swaminathan V, Mythreye K, O'Brien ET, Berchuck A, Blobe GC, Superfine R. (2011). Mechanical stiffness grades metastatic potential in patient tumor cells and in cancer cell lines. *Cancer Res.* **71**(15), 5075-5080.

174. Ujihara Y, Nakamura M, Wada SA. (2011). Mechanical Cell Model and Its Application to Cellular Biomechanics. In Fazel R (Ed.) *Biomedical Engineering - From Theory to Applications*, ISBN: 978-953-307-637-9, InTech, DOI: 10.5772/19570.

175. Rape AD, Guo WH, Wang YL. (2011). The regulation of traction force in relation to cell shape and focal adhesions. *Biomaterials.* **32**(8), 2043-2051.

176. Plotnikov SV, Pasapera AM, Sabass B, Waterman CM. (2012). Force fluctuations within focal adhesions mediate ECM-rigidity sensing to guide directed cell migration. *Cell* **151**(7), 1513-1527.

177. Liu Z, Tan JL, Cohen DM, Yang MT, Sniadecki NJ, Ruiz SA, Nelson CM, Chen CS. (2010). Mechanical tugging force regulates the size of cell-cell junctions. *Proc. Natl. Acad. Sci. USA* **107**(22), 9944-9949.

178. Rauzi M, Verant P. Lecuit T, Lenne PF. (2008). Nature and anisotropy of cortial forces orienting Drosophila tissue morphogenesis. *Nat. Cell Biol.* **10**(12), 1401-1410.

179. Katoh K, Kano Y, Amano M, Kaibuchi K, Fujiwara K. (2001). Stress fiber organization regulated by MLCK and Rho-kinase in cultured human fibroblasts. *Am J Physiol Cell Physiol.* **280**(6), 1669-1679.

180. Russo JM, Florian P, Shen L, Graham WV, Tretiakova MS, Gitter AH, Mrsny RJ, Turner JR. (2005). Distinct temporal-spatial roles for rho kinase and myosin light chain kinase in epithelial purse-string wound closure. *Gastroenterology.* **128**(4), 987-1001.

181. Tamada M, Perez TD, Nelson WJ, Sheetz MP. (2007). Two distinct modes of myosin assembly and dynamics during epithelial wound closure. *J. Cell Biol.* **176**(1), 27-33.

182. Danjo Y, Gipson IK. (1998). Actin ‘purse string’ filaments are anchored by E-cadherin-mediated adherens junctions at the leading edge of the epithelial wound, providing coordinated cell movement. *J. Cell Sci.* **111**(pt 22), 3323-3332.

183. Jacinto A, Martinez-Arias A, Martin P. (2001). Mechaisms of epithelial fusion and repair. *Nat. Cell Biol.* **3**(5), E117-123.

184. Zahm JM, Kaplan H, Herard AL, Doriot F, Pierrot D, Somelette P, Puchelle E. (1997). Cell migration and proliferation during the in vitro wound repair of the respiratory epithelium. *Cell Motil. Cytoskeleton.* **37**(1), 33-43.

185. Thompson WR. (1935). On the criteria for the rejection of observations and the distribution of the ratio of the deviations to sample standard deviations. *Annals of Mathematical Statistics*. **6**, 214-219.

186. Burke TA, Christensen JR, Barone E, Suarez C, Sirotkin V, Kovar DR. (2014). Homeostatic actin cytoskeleton networks are regulated by assembly factor competition for monomers. *Curr. Biol.* **24**, 1-7.

187. Baur PS Jr, Parks DH, Hudson JD. (1984). Epithelial mediated wound contraction in experiment wounds – the purse string effect. *J. Trauma.* **24**(8), 713-720.

188. Carvalho A, Desai A, Oegema K. (2009). Structural memory in the contractile ring makes the duration of cytokinesis independent of cell size. *Cell.* **137**, 926-937.

189. Klarlund JK. (2012). Dual modes of motility at the leading edge of migrating epithelial cell sheets. *Proc. Natl. Acad. Sci. USA* **109**(39), 15799-15804.